MEASUREMENT AND ANALYSIS OF MAGNETOCARDIOGRAMS FOR SHIELDED AND UNSHIELDED SETUPS

By

PRAGYNA PARIMITA SWAIN

Enrolment No.: PHYS 02 2015 04 021

Indira Gandhi Centre for Atomic Research, Kalpakkam

A thesis submitted to the

Board of Studies in Physical Sciences

In partial fulfillment of requirements

for the Degree of

DOCTOR OF PHILOSOPHY

of

HOMI BHABHA NATIONAL INSTITUTE

February, 2021

Homi Bhabha National Institute[1]

Recommendations of the Viva Voce Committee

As members of the Viva Voce Committee, we certify that we have read the dissertation prepared by **Ms Pragyna Parimita Swain** entitled **"Measurement and analysis of magnetocardiograms for shielded and unshielded setups"** and recommend that it may be accepted as fulfilling the thesis requirement for the award of Degree of Doctor of Philosophy.

Chairman– **Dr. B P C Rao**	BPCRao
Guide / Convener – **Dr. Awadhesh Mani**	Awadhesh Mani
Examiner - **Dr. K Sethupathi**	By VC For Rao
Member 1- **Dr. S. V. M. Satyanarayana**	
Member 2- **Dr. Sharat Chandra**	
Member 3- **Dr. V Jayaraman**	V. Jayaraman 04.
The Technical Adviser- **Dr. K Gireesan**	Gireesan. K

Final approval and acceptance of this thesis is contingent upon the candidate's submission of the final copies of the thesis to HBNI.

I/We hereby certify that I/we have read this thesis prepared under my/our direction and recommend that it may be accepted as fulfilling the thesis requirement.

Date: 13/07/2021

Place: Kalpakkam

Awadhesh Mani

Dr Awadhesh Mani
(Guide)

STATEMENT BY AUTHOR

This dissertation has been submitted in partial fulfilment of requirements for an advanced degree at Homi Bhabha National Institute (HBNI) and is deposited in the Library to be made available to borrowers under rules of the HBNI.

Brief quotations from this dissertation are allowable without special permission, provided that accurate acknowledgement of source is made. Requests for permission for extended quotation from or reproduction of this manuscript in whole or in part may be granted by the Competent Authority of HBNI when in his or her judgment the proposed use of the material is in the interests of scholarship. In all other instances, however, permission must be obtained from the author.

Pragyna Parimita Swain

Pragyna Parimita Swain

DECLARATION

I, hereby declare that the investigation presented in the thesis has been carried out by me. The work is original and has not been submitted earlier as a whole or in part for a degree / diploma at this or any other Institution / University.

Pragyna Parimita Swain

Pragyna Parimita Swain

List of Publications arising from the thesis

Journal

1. "A feasibility study to measure magnetocardiography (MCG) in unshielded environment using First Order Gradiometer", **Pragyna Parimita Swain**, S Sengottuvel, Rajesh Patel, Awadhesh Mani and K Gireesan, *Biomedical Signal Processing and Control*, **2020**, *55*, 101664 1-9.

2. "Solving inverse problem in magnetocardiography by pattern search method", **Pragyna Parimita Swain**, S Sengottuvel, Rajesh Patel, Awadhesh Mani, Raja J Selvaraj and Santhosh Satheesh, *IETE Journal of Research,* DOI: 10.1080/03772063.2021.1946436.

3. "Magnetocardiographic source localization for shielded and unshielded set-ups", **Pragyna Parimita Swain**, S Sengottuvel, Rajesh Patel, Awadhesh Mani and Raja J Selvaraj, *Computer Methods in Biomechanics and Biomedical Engineering: Imaging and Visualization* (Under Review).

Conferences

1. "Measurement of Magnetocardiogram in unshielded environment", **Pragyna Parimita Swain**, S Sengottuvel, Rajesh Patel, Awadhesh Mani and K Gireesan, *National Superconductivity and Cryogenics Conference (NSCS-26)*, VECC, Calcutta, India, (Feb 22-24) 2017.

2. "Analysis of the P wave measured during posterior MCG", **Pragyna Parimita Swain**, S Sengottuvel, Rajesh Patel, Awadhesh Mani and K Gireesan, *Research Scholars Meet on*

Materials Science and Engineering of Nuclear Materials (RSM-MSENM), HBNI. IGCAR. Kalpakkam. India. (May 7-9) 2018.

3. "Comparison on magnetic source depth localization in magnetometer and gradiometer", **Pragyna Parimita Swain**, S Sengottuvel, Rajesh Patel, Awadhesh Mani and K Gireesan, *National Superconductivity and Cryogenics Conference (NSCS-27)*, IIT Bombay. Mumbai. India. (Jan 16-18) 2019.

4. "Understanding atrial electrophysiology using posterior magnetocardiography", **Pragyna Parimita Swain**, S Sengottuvel, Rajesh Patel, Awadhesh Mani and K Gireesan, *National Symposium on Instrumentation (NSI-42)*, (Through Virtual Mode). India. (Dec 28-29) 2020.

Pragyna Parimita Swain

Pragyna Parimita Swain

Dedicated to …

My Beloved Family

ACKNOWLEDGEMENTS

It would not have been possible without the support and encouragement of many people who contributed and extended their valuable co-operation in the completion of the research work. It is pleasure to convey my gratitude to them all in my humble acknowledgement.

First of all, I would like to express my sincere gratitude to my supervisor Dr. Awadhesh Mani, Head, Low Temperature Studies Section, Materials Science Group, Indira Gandhi Centre for Atomic Research (IGCAR) for his continuous support, inspiring guidance, valuable advice and encouragement throughout the work. He has always been a source of motivation for me in difficult times during the research work. I am grateful to him for all his care, help and patience.

I express my heartfelt gratitude to my Technology Advisor (TA) Dr. K Gireesan for all his guidance, help and valuable suggestions. His constructive comments and moral support during all aspects of this work have provided a good basis for the present thesis. My sincere thanks goes to my doctoral committee members Dr. B. P. C. Rao, Dr. S. V. M. Satyanarayana, Dr. V. Jayaraman, Dr. Sharat Chandra, and Dr. Siva Kumar (former member) for their encouragement, valuable comments and insightful suggestions during the course of the thesis work. I am grateful to Dr. R. Rajaraman, Dean Academic, Physical Sciences and Dr. N. V. Chandra Shekar (former Dean) for their constant help and support. I express my sincere gratitude to Mr. R. Baskaran, Head, SQUIDs and Applications Section for his valuable suggestions and assistance during the work. Dr. Shaju K Albert, Director, Materials Science Group (MSG) and Dr. G. Amarendra, former Director of MSG are thanked for their inspiration and encouragement. I thank Dr. A. K. Bhaduri, Director, IGCAR for permitting me to pursue research in this reputed centre.

I feel extremely fortunate to have Mr. S. Sengottuvel and Mr. Rajesh Patel as my colleagues at IGCAR, whose kind co-operation, friendly company, suggestions and invaluable help during my research period has provided an amicable environment to learn and grow. I thank my fellow colleagues Mr. Fayaz Khan and Mr. Kesavaraja for their help, useful technical discussions and moral support. Dr. R. Nagendran is thanked for his technical help and support.

I owe special thanks to our collaborators Dr. Raja J Selvaraj, Dr. Santhosh Satheesh from Department of Cardiology, JIPMER, Puducherry for providing subjects for carrying out the research as well as various technical discussions. My sincere gratitude goes to Mr. M. P. Janawadkar, former Director, MSG and Dr. T. S. Radhakrishnan, formerly Head, MSG for their valuable advice in my work, suggestions and unconditional support in many ways.

My heartfelt thanks goes to my dear friends Surojit, Geeti, Ijee, Shubhra, Bijay, Akshaya, Alok, Binaya, Dillip, Gopi, Bala, Dhilipan, Rasitha, Jakatha and all Enclavians for their warm friendship.

I owe a lot to my parents Narendra Kumar Swain and Sabita Swain, who have been so caring and supportive at every stage of my personal and academic life. I express my loving thanks to my younger brother Mani Prasad Swain and younger sister Rasmita Swain for their affection. I am forever grateful to my grandparents Bandhu Swain and Kanchan Swain whose foresight and values paved the way for a privileged education.

Above all, I praise almighty God, for whatever I have got in my life and for being with me all the time.

Pragyna Parimita Swain

TABLE OF CONTENTS

LIST OF FIGURES

LIST OF TABLES

Chapter 6

SUMMARY AND FUTURE WORK

6.1 Summary

The thesis presents the results pertaining to MCG measurements carried out in both shielded and unshielded setups for both healthy subjects and a few subjects with cardiac disorders. Some of the salient results presented in the thesis are listed below:

- The use of Magnetic field map (MFM) to provide a visualization of the underlying cardiac activity at any instant of time has been illustrated with several examples. The investigations carried out during this work reaffirm the utility of MFM in depicting the spatial distribution of cardiac magnetic field in order to allow development of suitable criteria to easily recognize possible deviations from the appearance of the normal MFM and to associate these deviations with specific cardiac disorders. Results obtained during the course of this work provide the necessary confidence to propose the use of MFM as a standard tool for an easy and quick diagnosis of cardiac dysfunctions using MCG.

- MFM patterns characteristic of two different cardiac disorders namely, coronary artery disease (CAD) and right bundle branch block (RBBB), were investigated in detail to identify certain quantitative MFM parameters such as maximum current angle that could be used for the diagnosis and assessment of such disorders. Possible interpretation of the values of these parameters has been evolved, which is consistent with the underlying pathophysiology in each case.

- Posterior MCG was measured and analyzed to investigate propagation of the activation front from right atrium to left atrium towards the end of the P wave. Posterior MCG is paramount not only for some atrial signals, but also to get important diagnostic information about posterior myocardial infarction (MI). It may be noted that there are difficulties in visualizing the posterior myocardium using the standard 12-lead ECG. Even when the standard 12 lead ECG is augmented by additional posterior leads V7, V8 and V9, there are issues related to ECG signal strength on the posterior thoracic surface, often necessitating the use of moderately invasive esophageal ECG lead. In this context, non-invasive posterior MCG measurement appears to have considerable potential in contributing to better understanding of some atrial signals, and possible investigation of posterior myocardial infarction.

- A wide spectrum of issues and pre-requisites for establishing an unshielded MCG setup have been addressed. These include, among others,

  i. Identifying a suitable magnetically quiet site by conducting a site-survey of ambient magnetic noise at the site;

  ii. Evaluation of spectral density of noise of the SQUID sensor as a function of frequency at the unshielded site to assess the feasibility of making MCG measurements at the unshielded site;

  iii. Use of single lead ECG to derive R-peak time instants for epoching and averaging of measured MCG data at the unshielded site;

  iv. Compensation for the fall in SNR in MCG data measured at the unshielded site by signal denoising scheme based on EEMD;

v. Comparative assessment of the measured MCG signals outside and inside the Magnetically Shielded Room.

- A feasibility test to record MCG with minimal signal loss at a totally unshielded site employing First Order Gradiometers (FOG) has been carried out. MCG signals were successfully extracted from the measured raw data by using a combination of signal averaging (to suppress uncorrelated noise) and EEMD (to further enhance the SNR). It was shown that the quality of MFM constructed and the values of quantitative parameters extracted from the MFM were comparable to the corresponding results obtained from measurements carried out inside the Magnetically Shielded Room. This gives the necessary confidence for proposing to establish a low-cost unshielded MCG system in a clinical setting.

- A local optimization algorithm known as Nelder-Mead simplex method was utilized for estimating the position of the cardiac source responsible for producing the measured magnetic field distribution by using the initial estimates of the source parameters derived from the pseudo-current density (PCD) map to ensure computational efficiency, and a quicker source localization.

- A detailed validation procedure was devised and executed to evaluate the source localization accuracy in estimating cardiac sources using both computer simulated, data-sets generated by calculating the magnetic field produced by a current dipole admixed with controlled amount of noise as well as experimentally measured data-sets generated by measuring the magnetic field produced by a small multi-turn test coil placed at known position with respect to the sensor array. Use of noise admixed data-sets with different values of SNR enabled the source localization accuracy to be assessed under realistic experimental conditions.

- Localization of the cardiac sources was carried out from MCG data measured on healthy subjects, as well as subjects with cardiac disorders such as coronary artery disease (CAD) and right bundle branch block (RBBB), and the source positions inferred at different instants of time along the cardiac cycle were found to be in general agreement with the underlying cardiac electrophysiology in each case. The results obtained demonstrate the potential of the MCG technique in development of suitable criteria for diagnosis of cardiac disorders based on MFM parameters such as maximum current angle, and source parameters such as position and orientation.

6.2 Future scope

- In the present thesis work, the cardiac source has been modeled as a single equivalent current dipole (ECD) at each instant of time, which limited the source localization technique to analyze MCG data-sets which generate nearly dipolar MFM in practice. As a future work, it may be interesting to extend the work to more complex source models such as those involving multiple point dipoles, higher order multipoles, or dipoles distributed over a region of space, which may be more suitable for describing subjects with certain types of cardiac disorders resulting in non-dipolar MFM patterns (for example, subjects with fragmented QRS, WPW syndrome, atrial flutter etc).

- The present study models the thorax as a horizontally layered conductor, for which the contribution of volume currents to the measured external magnetic field vanishes. However, towards minimizing the possible source localization error, it may be interesting to consider a more realistic volume conductor model in future by explicitly taking into account the detailed geometry and electrical conductivity profiles of the intervening tissues and structures surrounding the heart.

- As part of possible future work, it may be interesting to project the source parameters found using the present technique of source localization onto CT/MRI images for the purpose of better visualization of the sources in a clinical setting. This requires co-registration of the different coordinate systems used for MCG and CT/MRI, perhaps by having a set of three current carrying reference coils fixed onto the subject which are imaged independently using both MCG as well as CT/MRI systems so that actual position coordinates of the three reference coils are known in both the coordinate systems. It is then possible to find the transformation matrix which transforms the position coordinates of the reference coils from the MCG coordinate system to CT/MRI coordinate system. Once the transformation matrix is known, coordinates of the sources identified by the MCG technique can be transformed to CT/MRI coordinate system, and imported into the CT/MRI image for display and visualization. This is expected to enhance the clinical diagnostic value of the source localization process.

- Though trigger locked averaging is a commonly used method for improving the SNR of the measured MCG signal (especially, when it is recorded at an unshielded site), application of such trigger locked averaging is known to affect and even eliminate the beat-to-beat specific variations, making the technique sort of unsuitable for studying the beat-to-beat dynamics of the cardiac time series. As part of future work, it may be interesting to explore other novel advanced hardware and software-based signal denoising approaches, which could be implemented for improving the SNR of the MCG data, while preserving the beat-to-beat variation in cardiac waveform.

- In future, there may be a possibility to explore the use of a combination of First Order Gradiometers (FOG) and Second Order Gradiometers (SOG) for recording unshielded MCG signals from deeper sources with an acceptable SNR (and minimum signal loss). If

successful, it may be possible to deploy such systems for demonstration of measurement and localization of cardiac sources from deeper sites which may also be relevant in several situations, including fetal heart assessments.

- The feasibility and potential value of the application of advanced artificial intelligence (AI) methods such as deep-learning convolutional neural network (CNN) etc to the magnetocardiogram can be studied. These AI methods developed with the use of large number of digital MCGs linked to rich clinical datasets might be able to perform accurate and quick human-like interpretation of MCGs. Uses may include detecting heart disease, treating stokes faster etc.

ABSTRACT

Magnetocardiography (MCG) is the technique to measure spatial distribution of cardiac magnetic fields originating from the electrophysiological activity of the heart, and is expected to effectively complement the routinely used electrocardiography (ECG) by providing additional independent information for the assessment of cardiac health and possible disorders. Measurement of both electric and magnetic field distributions produced by an electrophysiological source of interest is essential for a comprehensive understanding of the source characteristics just as the specification of both divergence and curl of a bounded vector field (such as the source current density) is required for reconstructing the vector field. In spite of the distinctive information provided by MCG which is independent of the information provided by ECG, application of MCG as a routine technique for the assessment of cardiac health is presently not very popular in clinical environments owing to the relatively high capital cost, use of cryogenic sensor technology and inherent non-portability of the MCG system. In addition, as opposed to the well-established standardized measurement and interpretation protocols available for ECG, standardized measurement protocols and visualization tools to quickly and directly interpret the MCG signals are not currently available. The present thesis takes cognizance of these limitations of the MCG technique, and strives to address some of them.

The thesis highlights the use of traditional technique based on Magnetic field map (MFM) and proposes its use as a standard tool for the visualization of the measured MCG data at any instant of time. Based on a detailed analysis of the measured MCG data by constructing MFM for several normal healthy subjects as well as a few subjects with known cardiac disorders, the work demonstrates the usefulness of quantitative parameters derived from the MFM in recognizing disorders such as coronary artery disease (CAD) and right bundle branch block (RBBB).

As a notable contribution, the present thesis describes a feasibility study to demonstrate the measurement of MCG at a completely unshielded site with an acceptable Signal-to-Noise Ratio (SNR) using a software-based signal denoising technique. The work addressed various issues such as site-survey of magnetic noise to select a relatively magnetically quiet site, assessment of SQUID-noise spectra measured at the unshielded site, development of procedures based on signal averaging and EEMD for noise suppression, and finally, the successful demonstration of extraction of MCG signals having acceptable SNR from the data recorded at the unshielded site. The study features the use of First Order Gradiometers (FOG) to record MCG at the unshielded site, and emphasizes the capability of such systems to record signals from deeper sources when compared to other systems based on Second Order Gradiometers (SOG).

Another major contribution relates to the localization of cardiac sources responsible for the measured magnetic field distribution by assuming simple source models. Taking the initial values of source parameters derived from the MFM and Pseudo-Current Density (PCD) maps to start the iterative optimization of source parameters, it has been shown that the optimization algorithm designed to minimize a suitably chosen cost function converges quickly to the final optimal solution. After extensive validation on simulated data-sets, the proposed algorithm has been used to evaluate the source parameters at various instants of time along the cardiac cycle for healthy subjects as well as for subjects with different cardiac disorders, and the source parameters were found to be in general agreement with the underlying electrophysiology in each case. The thesis highlights the possible potential of both the MFM parameters and source parameters evaluated from the MCG data for a quick recognition of specific cardiac disorders based on observed deviations of these parameters from the normal range of values.

Chapter 1

INTRODUCTION TO MAGNETOCARDIOGRAPHY

1.1 Electrophysiology of the heart

Heart is an organ which acts as a mechanical pump to send deoxygenated blood received from different parts of the body to the lungs for reoxygenation, and send oxygenated blood to different parts of the body [1]. Rhythmic contraction and relaxation associated with the mechanical action of the heart is initiated and streamlined by a sequence of electrical activations taking place inside the heart. The heart muscles include a group of specialized pace-making cells which are responsible for its electrical activity. These electrical signals originate from the gradients of ionic concentrations existing across the cell membrane of the cardiomyocyte owing to changes in selective permeability of the cell membrane to certain types of ions [2]. A change in the membrane permeability of Na^+ ions alter the originally negative resting membrane potential (about -90 mV) of the inner side of the cell membrane relative to the outer side of the cell membrane to a positive value (about +20 mV) during the depolarization phase leading to the development of an action potential. The movement of positively charged ions to the inner side of the cardiomyocyte is termed as the depolarization phase of the cardiomyocyte and the subsequent restoration of the electrical potential to the original resting value is termed as the repolarization phase. The characteristics of these action potentials in terms of strength and duration differ across the groups of cells located inside the heart [3], which constitute the conduction pathway of the heart, or in other words, the heart's electrical circuit. Sino-atrial node (located in the right atrium), atrio-ventricular node (located between the atrium and ventricles), bundle of His (located at the

upper part of the interventricular septum), the right and the left branches of the His bundle, Purkinje fibers (ramifications of the bundle branches) and the ventricular myocardium together constitute the conduction pathway (see figure 1.1a) [4]. The successive depolarization of cardiomyocytes over the localized regions of the conduction pathway could be visualized as a depolarization wave front representing the movement of electrical activation (see arrows in figure

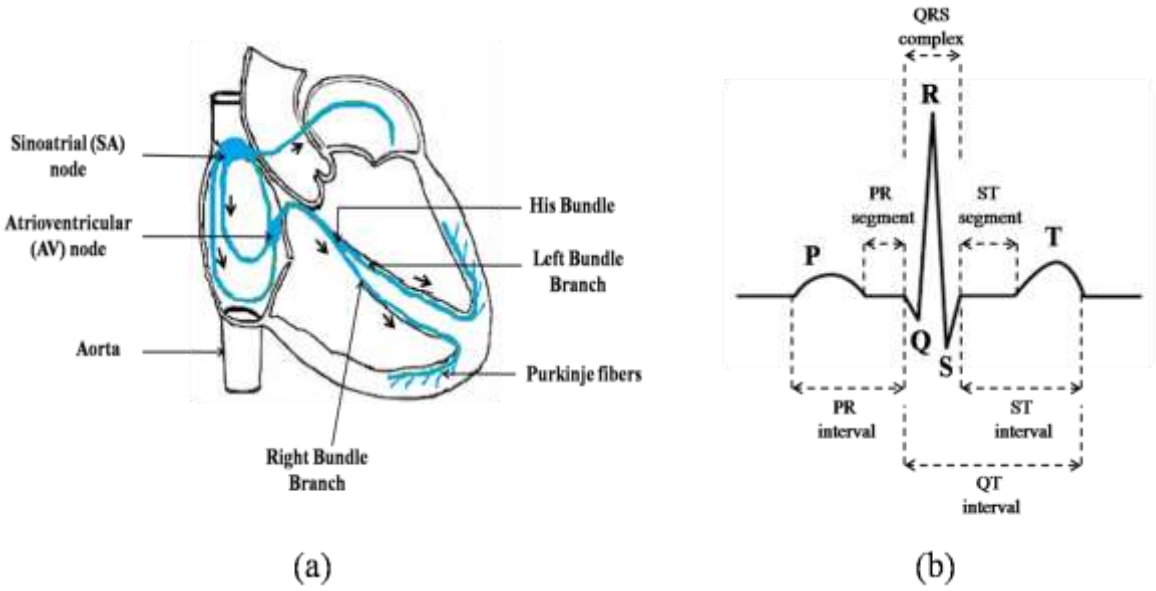

Figure 1.1 (a) Pathway for the cardiac conduction system (b) Pattern of a normal cardiac cycle. The electrical impulse originates at the sinoatrial (SA) node and then propagates along the atrioventricular (AV) node, His bundle, left and right bundle branches and Purkinje fibers causing the cardiac myocytes to depolarize. The depolarization of atria and ventricles manifest as the P wave and QRS complex in the cardiac cycle respectively. The subsequent repolarization of ventricular myocytes is observed as the T peak in the cardiac cycle. Various cardiac intervals and segments carrying clinical significances are indicated in panel (b).

1.1a) at a given instant of time in the cardiac cycle. This flow of current creates potential differences between different points on the body surface, which may be recorded as voltage signals using electrodes kept over standard positions on the thorax, and this recording is known as Electrocardiogram, or the ECG [5], which has become very popular among clinicians for the evaluation of cardiac activity. The electrical signal originates from the sinoatrial (SA) node, and propagates through the atrial myocardium to initiate a mechanical contraction of the upper chambers of the heart. This part of the activity is responsible for the appearance of the P wave in

ECG (see figure 1.1b) [6]. When the electrical activation reaches the AV node, there is a delay in further propagation, allowing time for both the ventricles to get filled with blood from the respective atria; this part of the activity is responsible for the appearance of isoelectric baseline segment of the PR interval in ECG. The signal then propagates to the Bundle of His and divides into two pathways to activate the left and right bundle branches on both the sides of the interventricular septum. Subsequently, the activation spreads across the Purkinje fibers and depolarizes the whole ventricular myocardium, resulting in mechanical contraction of both the ventricles. This is manifested as the QRS segment of the cardiac cycle in ECG. The last event of the cardiac cycle is the subsequent repolarization of the ventricles; this part of the activity manifests as the T wave in ECG, representing the phase during which the ventricles relax. The speed of this electrical conduction dictates the heart rate, which is typically in the range of 60-100 beats per minute for a normal resting individual.

Various intervals and segments in the ECG corresponding to different phases of activation front as it propagates across the cardiac conduction system are of considerable clinical importance in order to assess the underlying cardiac electrophysiology and thus provide a direct measure of the heart's functionality. For a normal heart, the PR interval ranges between 0.12 s to 0.20 s [7]. The duration between the start of QRS complex to the end of the T wave is known as the QT interval and it normally ranges between 0.34 s to 0.45 s. The duration of QRS ranges between 0.80-0.120 s. The line joining the end of QRS segment to the start of T wave is known as the ST segment which typically has a duration ranging between 0.12-0.2 s.

Magnetocardiography (MCG) is a technique to measure the magnetic fields associated with this electrical activity of the heart with signal features similar to those observed in a typical ECG [8]. However, MCG signals are extremely weak with the maximum amplitude representing the R wave peak being just about 50 pT, which is a million times weaker than the

earth's magnetic field. Owing to this, the MCG signals can be measured only by using highly sensitive magnetic field sensors like Superconducting Quantum Interference Devices (SQUID) operating inside a magnetically shielded room (MSR) capable of attenuating external electromagnetic noise. The first MCG was recorded by Baule and McFee in the year 1963 using two large coils with about two million turns wound over a ferrite core placed over the chest, connected in opposition to cancel the ambient noise [9]. The real breakthrough in MCG, however, came only after the advent of SQUIDs with unparalleled sensitivity, which allowed measurements to be performed with clinically acceptable Signal-to-Noise ratio (SNR) [10]. Currently, MCG is being used in several laboratories and hospital set-ups across the world, both for investigating the functioning of normal human heart and for clinical assessment of possible abnormalities [11-13].

1.2 Advantages of MCG

Though the morphological features of MCG such as P wave, QRS complex, T wave are similar to those found in an ECG, the two techniques complement each other in measuring two different physical quantities, (i.e. voltage in case of ECG and magnetic field in case of MCG). Indeed, combining the diagnostic information provided by both ECG and MCG has been shown to be extremely useful in obtaining a comprehensive picture of cardiac electrophysiology, and in evolving an effective management plan in case of possible abnormalities. Some of the major advantages offered by the MCG technique, which are more relevant from a clinical perspective, are listed below.

(a) MCG is sensitive to the currents tangential to the chest surface (producing a component of magnetic field normal to the chest, which can be measured by an external SQUID sensor), whereas ECG is sensitive to both radial and tangential flow of current [14]. However, in a majority of abnormalities representing altered cardiac activations, the

current flow is known to be tangential rather than radial, facilitating a better detection of cardiac dysfunctions in MCG since any radial sources capable of influencing the ECG features are virtually "silent" in MCG. This fact is also responsible for the improved sensitivity and specificity of MCG compared to other techniques such as ECG or the body surface potential mapping technique [15-17]. Cardiac pathophysiologies in which MCG has been shown to be beneficial include:

- Assessment of ischemic heart disease to detect injury currents
- Risk stratification for coronary artery disease

(b) MCG is known to be more sensitive to the primary currents associated with the actual electrophysiology of the heart, unlike ECG which is sensitive to secondary extracellular (volume) currents in cardiac tissues in a horizontally layered conductor model representing the human chest [18]. The sensitivity of MCG to primary currents (rather than the secondary volume currents) facilitates localization of cardiac sources closer to the actual region of interest. A few clinical applications exploiting this advantage of MCG include [19-21]:

- Non-invasive localization of cardiac arrhythmias such as ventricular tachycardia, premature ectopic beats, supraventricular arrhythmias etc.
- Localization of accessory pathways or pre-excitation sites in Wolf-Parkinson-White (WPW) syndrome

(c) MCG is less affected by the conductivity profile of the intervening tissues than ECG. ECG is highly influenced by the insulating effects of the bones, blood and other body

tissues surrounding the heart [22]. This aspect facilitates the following applications in clinical cardiology [23-29]:

- Surface recording of His bundle signals and late potentials
- Pre- and post-surgical mapping of cardiac sources for possible catheter interventions
- Measurement of cardiac signals on the posterior surface, where ECG is known to be not much sensitive due to the electrical resistivity of the lungs filled with air.
- Non-invasive cardiac assessments for fetal wellbeing, detection of congenital heart diseases and fetal arrhythmia. Fetal ECG signals are likely to get distorted by the electrically insulating layers (including *vernix caseosa* on the fetal skin) surrounding the uterus, especially, during the last trimester of pregnancy

Some of the other advantages of MCG include the following [24]:

- Since MCG is a non-contact technique, it may be useful for subjects with severe burn related injuries on the chest surface. Further, MCG requires less time for subject preparation unlike ECG, making it suitable for mass screening.
- MCG measurement does not require any reference electrode (unlike ECG which measures potential at the electrode relative to a reference zero). This may enable true measurement of ST segment changes in subjects with ischemic heart disease.
- MCG enables visualization of cardiac currents with the help of pseudo-current density maps generated by taking the planar gradient of the spatial distribution of cardiac magnetic field; such maps cannot be constructed using the ECG data.

1.3 Sensors used for MCG measurements

A variety of sensors with sensitivity ranging between few femto-Tesla to few pico-Tesla have been tested for their ability to measure cardiac magnetic fields [30-34]. A brief description of some of these sensors which have enabled identification of cardiac features in a typical MCG signal measured using them is given below:

(a) Induction coil magnetometer

The induction coil magnetometer or the search coil magnetometer works on the principle of Faraday's law of induction and measures the voltage induced in a coil by temporal variation in magnetic field. Integrator circuits are used to integrate the induced voltage in order to generate an output which is proportional to the instantaneous value of magnetic field. These devices are inexpensive, portable and work at room temperature. However, the sensitivity of these devices is rather low (~100 pT) [30] even when coils with a very large number of turns are used together with compensating coils to offset the parasitic signal induced by ubiquitous magnetic noise. The sensitivity attained is, however, inadequate to reveal all the features in a typical cardiac cycle.

(b) Fluxgate magnetometer

A fluxgate magnetometer typically consists of two coils of wire wrapped around a small ferromagnetic core having a very high magnetic permeability. An alternating electric current is passed through one of the coils (also known as the drive coil), which saturates the core alternately in both positive and negative directions. This changing magnetic field induces a voltage across the second coil (also known as sensing coil). In the absence of any externally applied magnetic field, voltage induced in the sensing coil is at the drive frequency. However, in the presence of a magnetic field (signal of interest), the core gets saturated more quickly along the direction of that field and less quickly in the opposite direction. Hence, the voltage induced in the sensing coil has

a component at twice the drive frequency (second harmonic). This second harmonic signal is detected and fed back to operate the flux gate as a null detector in order to increase linearity and enhance dynamic range; feedback signal is proportional to the magnetic field required to be sensed. The sensitivity of fluxgate magnetometer is typically ~10 pT, which is adequate to capture only prominent cardiac peaks such as the R peak of a cardiac cycle [31].

(c) Magnetoresistive sensor

Magnetoresistive (MR) sensors work by detecting the change in resistance caused by an applied magnetic field. They range from Anisotropic Magnetoresistance Sensors (AMR), Giant Magnetoresistance Sensors (GMR) and Tunnel Magnetoresistance Sensors (TMR). Typically, these sensors are based on ferromagnetic thin films separated by either metallic or insulating layers, and depending on their design, their sensitivity may range from ~100 pT to ~10 pT [32]. Since these sensors work at room temperature, it is feasible to reduce the stand-off distance between the source and sensor by bringing them closer to the subject compared to what is possible while using a cryogenic sensor such as SQUID. However, further improvements in sensitivity are required for use of such sensors for multichannel biomagnetic applications.

(d) SQUID sensor

SQUID or Superconducting Quantum Interference Device is a sensor capable of detecting an extremely small change in magnetic flux. The noise floor of this sensor is as low as 3 fT in commercially available instruments [33]. The device consists of a superconducting loop intersected by one or two Josephson junctions and requires cooling with liquid Helium (or liquid Nitrogen for devices based on high temperature superconductors) for its operation. SQUID sensors are most commonly used to measure the MCG signals since their sensitivity is sufficiently high to enable one to record all the features of the cardiac signal. Using SQUID

sensors, it is achievable to design and fabricate multichannel MCG systems, and hence, SQUID sensors have emerged as preferred sensors for these applications, despite the requirement of cryogenic operating temperatures.

(e) Optically Pumped Magnetometer

Use of an Optically Pumped Magnetometer (OPM) is a relatively new modality in measuring MCG signals. These magnetometers possess sensitivity ranging from about 100 fT to 1 pT depending on the details of design. These sensors are operated at room temperature, which is a major advantage of using such sensors. The vapour of an alkali metal such as Na, K, Rb, Cs etc. is utilized as the working substance for the OPM, and shift in atomic energy levels of the working substance in the presence of an external magnetic field is the basis of detection [34]. Further improvements are, however, required before it is possible to build multichannel MCG systems based on optically pumped magnetometers.

1.4 Noise affecting MCG

The sensor used in a typical MCG measurement is basically a transducer that produces an output voltage signal proportional to the magnetic field to be sensed. Since the magnetic fields measured in typical MCG measurements are very weak, associated voltage signals are also very low in amplitude, making it essential to consider in detail other sources of noise present at the sensor output. The most common types of noise encountered during a typical MCG measurement are discussed below.

(a) Thermal noise

Thermal noise or the Johnson-Nyquist noise is associated with the random thermal motion of the charge carriers such as electrons inside a conductor. This noise is independent of the applied

voltage and is unavoidable when the operating temperature is above absolute zero (0 K). The power spectral density of this noise is almost equal at all frequencies, and hence it is considered to be nearly white. Various electronic devices used in a typical MCG set-up could be a source of this noise and can affect the Signal-to-Noise ratio (SNR) of the measured MCG.

(b) Shot noise

This noise results from the discrete nature of charge carriers (electrons or holes). Unlike thermal noise, this noise is independent of temperature and depends only on the amount of current flowing inside a conductor. Use of various electronic circuits for measurement and control as part of a typical MCG set-up may potentially generate shot noise.

(c) 1/f noise

1/f noise is a low frequency noise for which the noise power varies inversely with frequency. It has been attributed to existence of electron traps with a range of activation energies, although there are several other mechanisms that could possibly explain the origin of 1/f noise. 1/f noise dominates at very low frequencies since the noise power associated with this source decreases as frequency increases. This noise arises mostly due to the use of sensors as well as various electronic devices as part of the overall measurement system.

(d) Ambient magnetic noise

This noise includes the magnetic field generated by the earth itself or due to the fluctuations in the intensity of the earth's field. The magnetic field of the earth has a static DC component of ~ 25-65 μT, depending on location, and slow temporal variations with an amplitude of several nT Activities such as movement of metallic or magnetic objects, vehicles etc. in the neighborhood

could also lead to fluctuations in the ambient magnetic field as well as spatial gradients in this field at the measurement site.

(e) Power line noise

The noise associated with the mains power line frequency (50 Hz or 60 Hz) and its harmonics are a major source of noise in MCG measurements especially in urban areas due to the presence of other electrical heavy duty equipments in the vicinity. Power line noise could get coupled to the sensor and electronic measuring circuits by either inductive coupling or capacitive coupling.

(f) Cryostat noise

A cryogenic sensor such as SQUID has to be cooled to its operating temperature by immersing the sensor in liquid helium or liquid nitrogen. Any movement or vibration of the cryostat, oscillation of liquid He or liquid N_2 surface (due to boil off etc.) could potentially add noise across the copper wires carrying signals from the sensors inside the cryostat to the preamplifiers located outside the cryostat. In addition, radiation baffles and other thermal shielding mechanical structures forming part of construction of the cryostat insert or the cryostat also add to the overall noise of the system. The cryostat noise may also include the noise associated with vibrations of wires or other structures at relatively low frequencies.

(g) Subject noise

This source of noise includes the biological artifacts arising due to the subject's breathing, movement of muscles with respect to the sensor array and the influence of activated biological sources other than the one under investigation.

The overwhelming ambient noise present at the measurement site creates a lot of difficulties in recording bio-magnetic signals unless the noise in the frequency bandwidth (0-1 kHz) of interest

is suppressed to a sufficiently low level. The conventional way of suppressing these parasitic sources of ambient noise is by using some form of shielding such as that provided by a magnetically shielded room (MSR) [9]. MSR serves to attenuate external ambient magnetic noise to a sufficiently low level and thereby enables the SQUID sensors to be used at their highest intrinsic sensitivity instead of being limited in attainable sensitivity by the ambient magnetic noise. The shielding of a MSR could be achieved by several means such as using high permeability materials (e.g. mu-metal) to provide low frequency magnetic shielding by providing a path of low magnetic reluctance for magnetic flux lines through such ferromagnetic shielding materials and by using materials with high electrical conductivity (e.g. aluminum) to provide high frequency shielding by inducing opposing eddy currents in the shielding materials; several thick layers of mu-metal and aluminum are used to realize sufficiently high shielding factors at frequencies of interest. Even superconducting materials could be used inside the cryostat to provide additional shielding around sensor location [35]. Some additional shielding against specific external magnetic noise sources in the vicinity could also be achieved by active compensation method, where any magnetic field fluctuations at a site are detected by a fast magnetic field sensor such as flux gate and are compensated in real time by an equal and opposite magnetic field generated by passing a suitable current through a large Helmholtz coil using a suitable feedback system [35]. A combined system consisting of shielded rooms with walls made up of several layers of mu-metal and aluminum together with such large active compensation coil systems is often used to achieve superior shielding performance in practice.

1.5 Major challenges faced by MCG

MCG has been established as a proven technique for the diagnosis and assessment of cardiac dysfunctions in several cases where the conventional techniques failed to give unambiguous conclusions. Further, MCG has been employed to obtain unique diagnostic information in a

completely non-invasive manner and help the clinician in arriving at clinically relevant decisions. However, the MCG technique is still not available for routine use in hospitals worldwide. Some of the major challenges faced by MCG technique for its adoption in hospital settings for regular clinical use are listed below.

- As opposed to the ubiquitous ECG, which is well established in a clinical setting, MCG is relatively new (although the technique is known to the medical fraternity) and a unified standard with respect to measurement locations and visualization tools to interpret the measured cardiac magnetic fields is still not available. This is due to differing designs of MCG set-ups presently being operated worldwide (with some set-ups using only a small number of channels in a moderately shielded room to keep the overall system cost lower while other set-ups using a very large number of channels in an excellent shielded room to obtain a comprehensive characterization of spatial distribution of cardiac magnetic field).

- The cost of a magnetically shielded room is a major component of the investment required to establish a MCG system in a laboratory or hospital setting. Indeed, the conventional way of measuring MCG inside a MSR leads to an increased cost of the MCG set up in addition to its overall complexity. Towards making a low cost and portable MCG set up, it is desirable to carry out the MCG measurements either inside a partially shielded enclosure (with minimal shielding) or at a completely unshielded site, thereby dispensing with the need for an expensive and bulky Magnetically Shielded Room.

- The cardiac signal is nonlinear and non-stationary in nature [36]. Hence, traditional signal denoising algorithms based on Fourier Transform are not very effective in denoising the measured MCG signal. Further, unlike ECG, MCG signals are tiny in magnitude and are more likely to get affected by various noise sources. Hence, more sophisticated denoising

techniques have to be implemented in practice to eliminate the noise (especially in unshielded or poorly shielded MCG set-ups) and unravel all the diagnostic features from a measured MCG data set.

It may be noted that, though currently it is desirable to explore the possibility of operating an unshielded MCG system in order to popularize the use of MCG technique widely by significantly lowering the installation cost, measurements inside a well shielded MSR under ideal conditions will remain the gold standard for basic research as well as for all types of experimental clinical studies.

1.6 Scope of the work

The present thesis takes into account the challenges (such as those outlined in section 1.5) faced by present day MCG and attempts to address some of them. The scope of work may be summarized as follows:

- Evaluating the use of some visualization tools which could be used as a standard practice in interpreting the measured cardiac magnetic fields
- Establishment of a MCG set-up operating in an unshielded environment
- Exploring the use of improved denoising techniques to improve the Signal-to-Noise ratio of MCG signals measured in an unshielded environment
- Localization of the site of activation of the cardiac signal for both normal subjects and subjects with cardiac dysfunctions

1.7 Organization of the thesis

The thesis comprises of six chapters which are outlined as follows.

In **Chapter 1,** the technique of magnetocardiography (MCG) is introduced. The similarity and differences between MCG and the conventionally used ECG are discussed. The major benefits of measuring MCG in clinical set-ups that are well demonstrated by various research groups have been presented. A variety of magnetic field sensors which have been used to measure MCG signal are described along with a comparison of their relative advantages and disadvantages. Various types of noise that are commonly encountered during a typical MCG measurement are also described. The chapter also deals with the status of MCG in the current context and discusses major factors that hinder the routine use of MCG for cardiac assessments in hospitals. The objective of the present thesis to make the MCG technique more widely accessible by lowering the overall cost of the MCG set-up while enabling the measurement of realistic signals in as accurate and reliable way as possible is clearly brought out.

Chapter 2 describes the various modules of the Supeconducting Quantum Interference Device (SQUID) based MCG system used in this work at IGCAR, Kalpakkam. The constituent sub-systems of the MCG set up are described along with other details related to construction of a magnetically shielded room (MSR), liquid helium cryostat, operating principle of SQUID sensors, and calibration of SQUID sensors etc. The chapter also presents a brief discussion on the procedure used for recording the MCG signal on human subjects and the ways of interpreting the measured cardiac signals for clinical diagnosis are summarized.

Chapter 3 deals with providing an easy and standardized procedure for the interpretation of magnetocardiograms. The chapter emphasizes the utilization of Magnetic field map (MFM), derived from the measured spatial distribution of cardiac magnetic fields over the thorax as a readily visualizable investigation tool. The importance of parameters derived from the MFM at specific time instants of the cardiac cycle to reliably classify cardiac anomalies has been examined, especially for patients with coronary artery disease (CAD) and right bundle branch

block (RBBB). Further, use of MFM to understand the spatial distribution of cardiac magnetic fields on the posterior surface of the thorax for healthy subjects is also studied.

Chapter 4 is devoted to the establishment of MCG set-up operating in an unshielded environment. The chapter lists the issues and pre-requisites starting from selecting a suitable site by carrying out a site survey of ambient magnetic noise in order to identify a site with sufficiently low magnetic noise to the measurement and analysis of MCG signals recorded in a totally unshielded manner at this site. The importance of software-based noise cancellation technique to improve the Signal-to-Noise ratio of the MCG signal measured in an unshielded environment is also emphasized. The signals measured in open unshielded environment and those measured inside the MSR are compared and quantified with a typical example of the MCG measured from a subject with a known cardiac dysfunction.

Chapter 5 is devoted to the estimation of cardiac source from the measured magnetic field distribution over the thoracic surface by solving the inverse problem. The chapter discusses the utilization of a local optimization method called Nelder-Mead method for this purpose with special emphasis on choosing the initial guess point by analyzing the spatial gradient of magnetic field values across the measurement plane in order to reduce the computational burden. Validation of the proposed idea in two different simulation scenarios, one using computer-simulated data, and another using experimental data measured using the MCG set-up with a small current carrying multi-turn copper coil acting as a source of magnetic field, has been demonstrated. The performance of the source localization algorithm at differing Signal-to-Noise ratio (SNR) conditions for the simulated signal is quantitatively analyzed. The outcome of the source localization method at various instants of the cardiac cycle for healthy subjects as well as for a few subjects with cardiac anomalies is presented by analyzing experimental MCG data-sets measured both inside the MSR and at the unshielded site.

Chapter 6 summarizes the major findings of the present thesis work in addition to outlining the scope and directions for probable future work.

References

1. Heart-healthy living. National Heart, Lung and Blood Institute. https://www.nhlbi.nih.gov/health-topics/heart-healthy-living. Accessed Oct.30, 2020.

2. What is cardiovascular disease? American Heart Association. https://www.heart.org/en/health-topics/consumer-health care/what-is-cardiovascular-disease. Accessed Oct.30, 2020.

3. E Riggin. Allscripts EPSi. Mayo Clinic. Oct.24, 2020.

4. C Parasakthi, R Patel, S Sengottuvel, N Mariyappa, K Gireesan, M Janawadkar and T Radhakrishnan. Establishment of 37 channel SQUID system for magnetocardiography. *AIP Conf Proc*. **1447** (2012) 871-872.

5. Mayoclinic.org/diseases-conditions/heart-disease/symptoms-causes/syc-20353118.

6. Symptoms, diagnosis and monitoring of arrhythmia. American heart association. https://www.heart.org/en/health-topics/arrhythmia/symptoms-diagnosis-monitoring-of-arrhythmia. Accessed Oct.30, 2020.

7. Congental heart defects. National Heart, Lung and Blood Institute. https://www.nhlbi.nih.gov/health-topics/heart-healthy-living. Accessed Oct.30, 2020.

8. Y Nakaya, H Mori. Magnetocardiography. *Clin Phys Physiol Meas.* **13** (1992) 191-229.

9. R Fagaly. Superconducting quantum interference device instruments and applications. *Rev Sci Instrum*. **77** (2006) 101101 1-45.

10. J Clarke and A Braginski, The SQUID handbook, vol I, WILEY-VCH, 2004, ISBN 9783527603640.

11. K Ogata, A Kandori, T Miyashita, K Tsukuda, S Nakatani, W Shimizu, H Kanzaki, K Miyatake, S Yamada, S Watanabe and I Yamaguchi. Noninvasive visualization of three-dimensional atrial electrical excitation using anterior and posterior magnetocardiogram. *Comput Cardiol.* **32** (2005) 527-530.

12. H Lim, H Kwon, N Chung, Y Ko, J Kim, I Kim, Y Park. Usefulness of magnetocardiogram to detect unstable angina pectoris and non ST-elevation myocardial infarction. *Am J Cardiol.* **103** (2009) 448-454.

13. Z Jun-Jie, J Shi-Qin, W Wei-Yuan, Z Chen, W Yan-Hua, L Ming and Q Wei-Wei. Cardiac electrical activity imaging of patients with CRBBB or CLBBB in magnetocardiography. *Chin Phys B.* **23** (2014) 048702 1-6.

14. J Malmivou and R Plonsey. Bioelectromagnetism. Oxford University press, New York, 1995.

15. S Watanabe and S Yamada. Magnetocardiography in early detection of electromagnetic abnormality in ischemic heart disease. *J Arrhythmia*. **24** (2008) 4-17.

16. R Agarwal, A Saini, T Alyousef and C Umscheid. Magnetocardiography for the diagnosis of coronary artery disease: a systematic review and meta-analysis. *Ann Noninvasive Electrocardiol.* **17** (2012) 291-8.

17. J Park, P Hill, N Chung, P Hugenholtz and F Jung. Magnetocardiography predicts coronary artery disease in patients with acute chest pain. *Ann Noninvasive Electrocardiol.* **10** (2005) 312-323.

18. V Pizella, S Penna, C Gratta and G Romani. SQUID systems for bio magnetic imaging. *Supercond Sci Tech.* **14** (2001) R 79–R 114.

19. I Tavarozzi, S Comani, C Gratta, S Luzio, G Romani, D Brisinda, S Gallina, M Zimarino, R Fenici and R Caterina. Magnetocardiography: Current status and perspectives-Part II: Clinical applications. *Ital Heart J.* **3** (2002) 151-165.

20. S Achenbach, W Moshage and K Bachmann. Magnetocardiography: Clinical investigations with a bio magnetic multichannel system. *Physiol Meas.***14** (1993) 61-68.

21. S Aita, K Ogata, K Yoshida, T Inaba, H Kosuge, T Machino, Y Tsumagiri, A Hattori, Y Ito, Y Komatsu, K Sekihara, H Horigome, K Aonuma, A Nogami, A Kandori and M Ieda. Noninvasive mapping of premature ventricular contractions by merging

magnetocardiography and computed tomography. *JACC Clin Electrophysiol.* **10** (2019) 1144-1157.

22. G Stroink, B Hailer and P Van Leeuwen. “Cardiomagnetism” in: Magnetism in Medicine edited by W Andra, H Nowak. Weinheim: *WILEY-VCH*, 2006.

23. S Sengottuvel, R Selvaraj, R Patel, S Satheesh, K Gireesan, M Janawadkar and T Radhakrishnan. Non-invasive determination of HV interval using magnetocardiography. *Pacing Clin Electrophysiol.* **40** (2017) 568-577.

24. R Fenici, D Brisinda and A Meloni. Clinical application of magnetocardiography. *Expert Rev Mol Diagn.* **5** (2005) 291-313.

25. J Strasburger, B Cheulkar and R Wakai. Magnetocardiography for fetal arrhythmias. *Heart Rhythm.* **5** (2008) 1073-1076.

26. S Strand, W Lutter, J Strasburger, V Shah, O Baffa and R Wakai. Low-cost fetal magnetocardiography: A comparision of superconducting Quantum Interference Device and Optically pumped magnetometers. *JAHA.* **8** (2019). https://doi.org/10.1161/JAHA.119.013436.

27. B Cuneo, J Strasburger, S Yu, H Horigome, T Hosono, A Kandori and R Wakai. In utero diagnosis of long QT-syndrome by magnetocardiography. *Circulation.* **20** (2013) 2183-91.

28. S Yamada, K Tsukuda, T Miyashita, K Kuga and I Yamaguchi. Non-invasive, direct visualization of macro-reentrant circuits by using magnetocardiograms: initiation and persistence of atrial flutter. *Europace.* **4** (2003) 343-50.

29. J Mooney, S Ghasemi-Roudsari, E Banham, C Symonds, N Pawloski and B Varcoe. A portable diagnostic device for cardiac Magnetic field mapping. *Biomed Phys Eng Express.* **3** (2017) 015008.

30. S Sengottuvel, A Sharma, D Biswal, P Khan, P Swain, R Patel and K Gireesan. Feasibility study on measurement of magnetocardiography using fluxgate magnetometer. *AIP Conf Proc.* **1942** (2018) 060018.

31. Y Shirai, K Hirao, T Shibuya, S Okawa, Y Hasegawa, Y Adachi, K Sekihara and S Kawabata. Magnetocardiography using magnetoresistive sensor array. *Int Heart J.* **60** (2019) 50-54.

32. H Koch. SQUID magnetocardiography: status and perspectives. *IEEE Trans Appl Supercond.* **11** (2001) 49-59.

33. Y Kim, I Sagukov and S Newman. Magnetocardiography with a 16-channeled fiber coupled single-cell Rb optically pumped magnetometer. *Appl Phys Lett.* **114** (2019) 143702.

34. R Ackermann, F Wiekhorst, A Beck, D Gutkeltch, F Ruede, A Schnabel, U Steinhoff, D Drung, J Beyer, C Abmann, L Trahms, H Koch, R Fischer, M Bader, H Ogata and H Kado. Multichannel SQUID system with integrated magnetic shielding for magnetocardiography of mice. *IEEE Trans Appl Supercond.* **17** (2007) 827-830.

35. B Hilgenfeld, E Strahamel, H Nowak and J Haueisen. Active magnetic shielding for biomagnetic measurement using spatial gradient fields. *Physiol Meas.* **24** (2003) 661-669.

36. D Guarin, E Delgado and A Orozco. Testing for nonlinearity in non-stationary physiological time series. *Annu Int Conf IEEE Eng Med Biol Soc.* (2011) 2671-4. doi: 10.1109/IEMBS.2011.6090734.

Chapter 2

SQUID BASED MCG MEASUREMENT SET-UP

2.1 MCG measurement set-up

The MCG measurement system installed at Indira Gandhi Centre for Atomic Research (IGCAR) comprises of different modules (units) such as Magnetically shielded room(MSR), superconducting quantum interference device (SQUID) gradiometers, liquid helium cryostat, SQUID electronics, data acquisition system etc. A block diagram of the whole MCG set-up is shown in figure 2.1. The system for MCG measurement was initially set-up as a single channel system and was subsequently upgraded progressively to house 4, 13 and 37 SQUID sensors [1]. In all such systems, a cryostat with a flat bottom profile (with signal pick-up loops of all the SQUID sensors arranged in a single plane inside the cryostat) is used to match the approximately flat shape of the surface of the thorax.

In the following, we give a brief discussion on each of the modules associated with the MCG measurement system.

2.2 SQUID as the magnetometer

A typical SQUID sensor consists of a superconducting loop interrupted by either one or two weak links, known as Josephson junctions. SQUID sensor with one Josephson junction is known as the RF SQUID and the SQUID sensor with two Josephson junctions is known as the DC SQUID. Usually, the RF SQUIDs are biased with radio frequency (RF) current whereas the DC SQUIDs

use direct current (DC) for biasing. Both types of SQUIDs act as flux to voltage transducers and their output voltage varies periodically with the applied magnetic flux with the periodicity of one flux quantum (ϕ_0). The SQUID sensors based on niobium (having transition temperature, $T_c \sim 9$

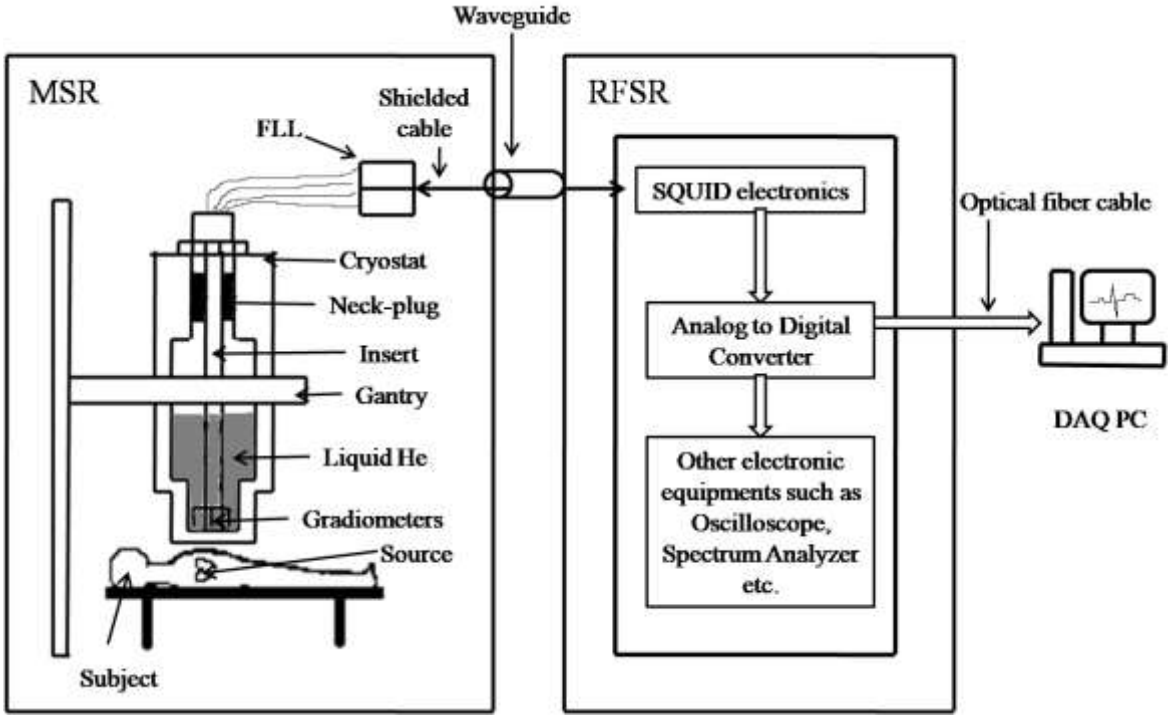

Figure 2.1 Block diagram of the MCG system used in the present work. The liquid Helium cryostat housing the axial SQUID gradiometers is placed inside the magnetically shielded room (MSR). The MCG signal originating from the subject is sensed and detected by the axial SQUID gradiometers. The corresponding SQUID output voltage from each sensor is amplified and processed by the FLL electronics placed inside the MSR. The SQUID output signal is then transferred to the radiofrequency shielded room (RFSR) via waveguides connecting MSR to RFSR, where the signal gets digitized using analog-to-digital converters (ADC). The RFSR houses all the electronic equipments that require supply from electrical mains power. The digitized data is then transmitted via an optical fiber link to a server class computer placed at an unshielded site for storage and graphical display of MCG data.

K) are usually operated at liquid helium temperature (4.2 K) and are known as low T_c SQUIDs (LTSC SQUID), whereas SQUIDs based on high temperature superconductors such as YBCO ($T_c \sim 90$ K) are operated at liquid nitrogen temperature (77 K) and are known as high T_c SQUIDs (HTSC SQUID) [2]. The sensitivity offered by the LTSC SQUIDs in detecting changes in the magnetic field is much superior to that offered by HTSC SQUIDs due to several reasons

including the fact that the thermal noise present at the output of the LTSC SQUIDs is much lower compared to that of HTSC SQUIDs on account of the lower operating temperature of LTSC SQUID. We use low temperature DC SQUIDs as the device for sensing the magnetic fields generated from human heart. The SQUID device used is based on Nb/AlO_x/Nb Josephson junctions. The working principle of the SQUID device is briefly discussed in the following section.

2.2.1 Working principle

In the absence of any external magnetic field, the bias current I_b in a symmetric DC SQUID gets equally divided across its two branches as shown in fig 2.2 and flows through the two Josephson Junctions. In this case, the critical current (the maximum current up to which there is no development of voltage) of the SQUID is $2I_0$, assuming the critical current for a single Josephson junction to be I_0. When an external magnetic field is applied perpendicular to the plane of the SQUID loop, the critical current of the SQUID is decreased. This is because of the circulation of an extra current known as the screening current I_s through the superconducting loop, which is induced in such a way as to produce the necessary magnetic flux required for flux quantization [3]. Mathematically,

$$\Phi_{tot} = \Phi_{ext} + LI_s = n\Phi_0 \qquad (2.1)$$

Here ϕ_{tot} denotes the total flux threading the SQUID loop, ϕ_{ext} is the applied external magnetic flux, I_s is the screening current induced by the applied magnetic flux, n is an integer chosen to minimize I_s, L is the inductance of the SQUID loop and ϕ_0 is the flux quantum (A flux quantum is an extremely small quantity of magnetic flux, being just about 2.07×10^{-15} Wb). When the external magnetic flux linked with the SQUID is $n\phi_0$, screening current induced in the loop is zero and when the externally applied magnetic flux is $(n+1/2)\ \phi_0$, a screening current of

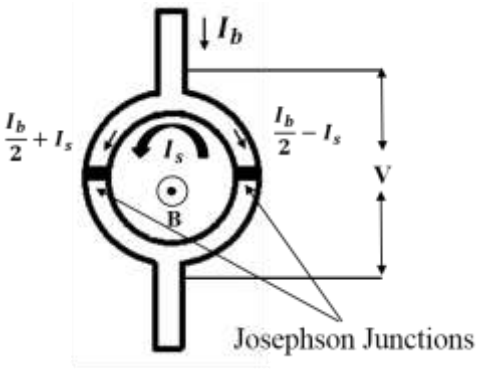

Figure 2.2 Schematic of a DC SQUID sensor.

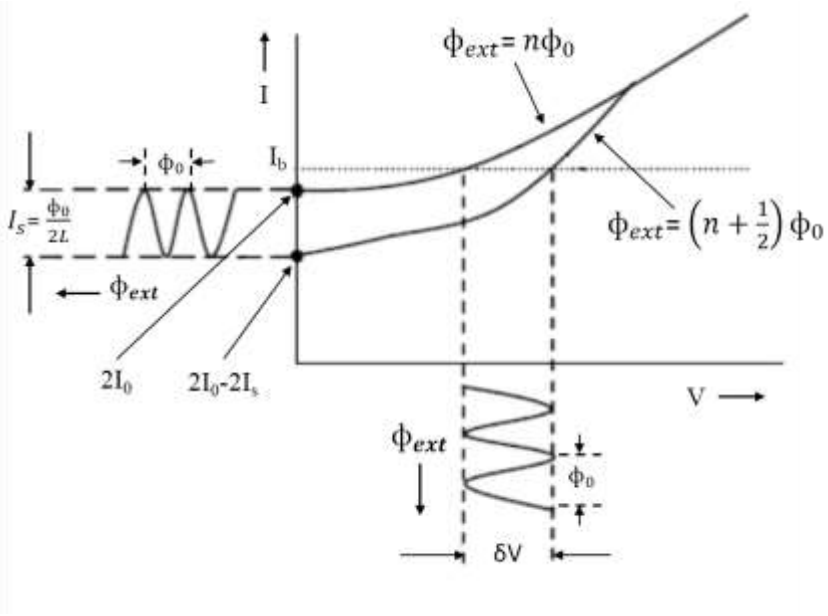

Figure 2.3 I-V characteristics of a DC SQUID in the presence of an externally applied magnetic field. Periodic variation in the screening current with period ϕ_0 and the resulting oscillatory output voltage of the SQUID as a function of magnetic flux are illustrated in the figure.

magnitude ($\phi_0/2L$) gets induced in the SQUID loop. Depending upon the magnitude and direction of the applied magnetic field, the screening current circulates either in a clockwise or anticlockwise direction along the SQUID loop. Accordingly, it gets added to the bias current of one branch and subtracted from the bias current of the other branch. This leads to a total current of $\left(\frac{I_b}{2} + I_s\right)$ flowing in one branch and $\left(\frac{I_b}{2} - I_s\right)$ flowing through the other branch (see figure

2.2). As soon as the total current in any one of the two junctions exceeds the critical current value I_0 of that junction, voltage starts developing across it. This leads to the reduction in the critical current of the SQUID from $2I_0$ to ($2I_0$-$2I_s$) (see figure 2.3). The critical current of SQUID, therefore, varies periodically with applied magnetic flux and is given by [4]:

$$I_{0_{max}}(\Phi_{ext}) = 2I_0 \left|\cos\left(\pi \frac{\Phi_{ext}}{\Phi_0}\right)\right| \quad (2.2)$$

If the SQUID is biased with a dc current slightly above $2I_0$, an output voltage oscillating periodically with the applied magnetic flux could be obtained as shown in figure2.3. In this way, any small variation in the applied magnetic flux reflects as a measurable change in the output voltage from the SQUID and hence the SQUID effectively acts as a flux to voltage transducer. The typical output voltage modulation depth (δV) of low T_c DC SQUID sensors is ~ 20-30 μV. The optimum modulation depth could be achieved by biasing the SQUID just above its maximum critical current.

As the output of SQUID sensor is periodic in nature, it is linearized for most of the practical applications using some dedicated electronics modules to process the SQUID output voltage. A brief discussion on these electronics modules is provided in the following section.

2.2.2 Flux Locked Loop (FLL) electronics

In principle, for a small range of flux (< $\phi_0/2$), it is doable to operate the SQUID around the optimum working point *W* located at the steepest part of the $V \sim \phi$ characteristic (as shown in figure 2.4). However, in cases where the amplitude of the signal flux exceeds this limit, it is quintessential to linearize the SQUID output using a feedback circuit to operate the SQUID as a null detector. Several SQUID read out schemes such as direct read out, flux locked loop mode etc. have been in use for this purpose [4, 5]. In most of these schemes, the SQUID is operated as

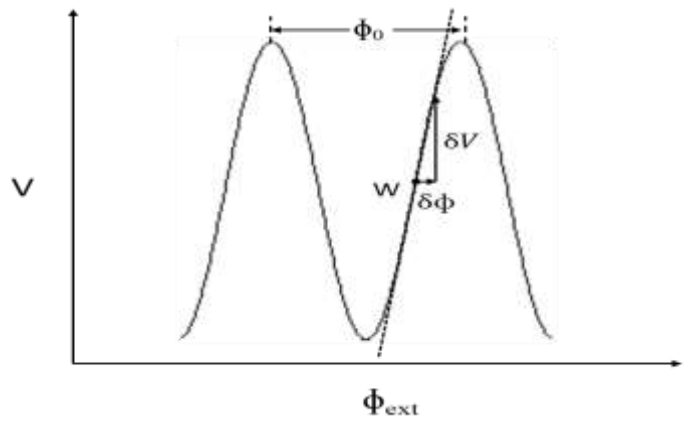

Figure 2.4 $V \sim \phi$ characteristic of SQUID showing periodic variation of output voltage with respect to the applied flux with periodicity of a flux quantum (ϕ_0). The working point *W* and the linear range of SQUID output voltage are indicated in the figure.

part of a feedback loop with a view to use the SQUID as a null detector of magnetic flux. The SQUID is locked to the working point *W* on the $V \sim \phi$ characteristic even when an external magnetic flux is applied by either cancelling the changes in input flux threading through the SQUID loop (flux locked loop mode) or the screening current flowing through the gradiometer (current locked loop mode) using suitable feedback circuits in SQUID electronics [6]. For the flux-locked-loop mode, in addition to using a signal coil to couple the magnetic flux to be detected into the SQUID loop, flux threading through the SQUID loop is modulated at a frequency of ~ 100 kHz using a modulation coil which is inductively coupled to the SQUID. The output voltage of the SQUID is amplified, filtered, phase sensitively detected, integrated and fed back as compensating flux to ensure that the SQUID remains locked to the chosen working point W. Here, we particularly discuss the operation of SQUID in the flux locked loop (FLL) mode, which is largely used for most of the DC SQUID read out systems.

Figure 2.5 shows a typical block diagram of the FLL electronics module used as part of the MCG system at IGCAR [7]. Here the signal flux which is to be measured is modulated by a high frequency sinusoidal modulation flux ϕ_m, (typically at a frequency of ~100 kHz or higher), generated using an oscillator connected to a modulation coil inductively coupled to the SQUID.

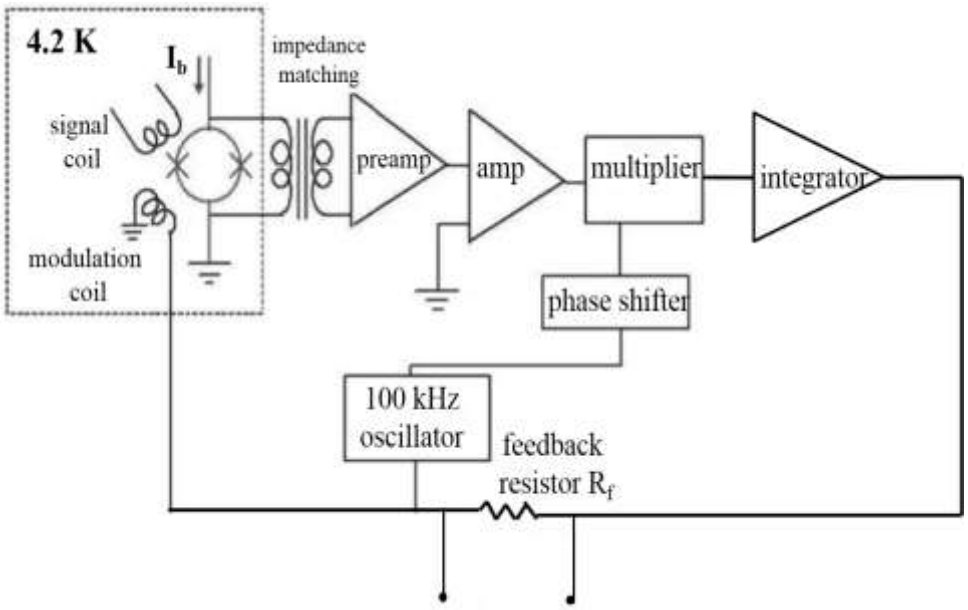

Figure 2.5 Schematic illustration of flux locked loop (FLL) electronics used to linearize the periodic output of the bare DC SQUID.

This shifts the originally low frequency magnetic field signal of interest to a frequency higher than the modulation frequency, and helps in eliminating the contamination of the signal by low frequency noise sources such as the 1/f noise of the preamplifier and low frequency drifts in the critical currents of the Josephson Junctions. Usually, the peak-to-peak amplitude of the modulation flux is set around $\phi_0/2$. When the applied magnetic flux linked to the SQUID loop is either zero or $n\phi_0$, the SQUID produces an output with a frequency twice that of the modulation flux (see figure 2.6). When this output is fed to a phase sensitive detector (PSD) designed to detect the signal synchronous with 100 kHz modulation frequency, there is no signal at the output of the PSD. However, when a signal flux other than $n\phi_0$ is applied, the output of the SQUID contains a component at the modulation frequency which is detected by the phase sensitive detector. The output of the PSD is integrated and the integrator output is fed back through a feedback resistor connected in series with a feedback coil inductively coupled to the SQUID, thereby feeding a current through the feedback coil to inject a compensating flux into the SQUID loop in a direction opposite to the signal flux. This keeps the SQUID locked at

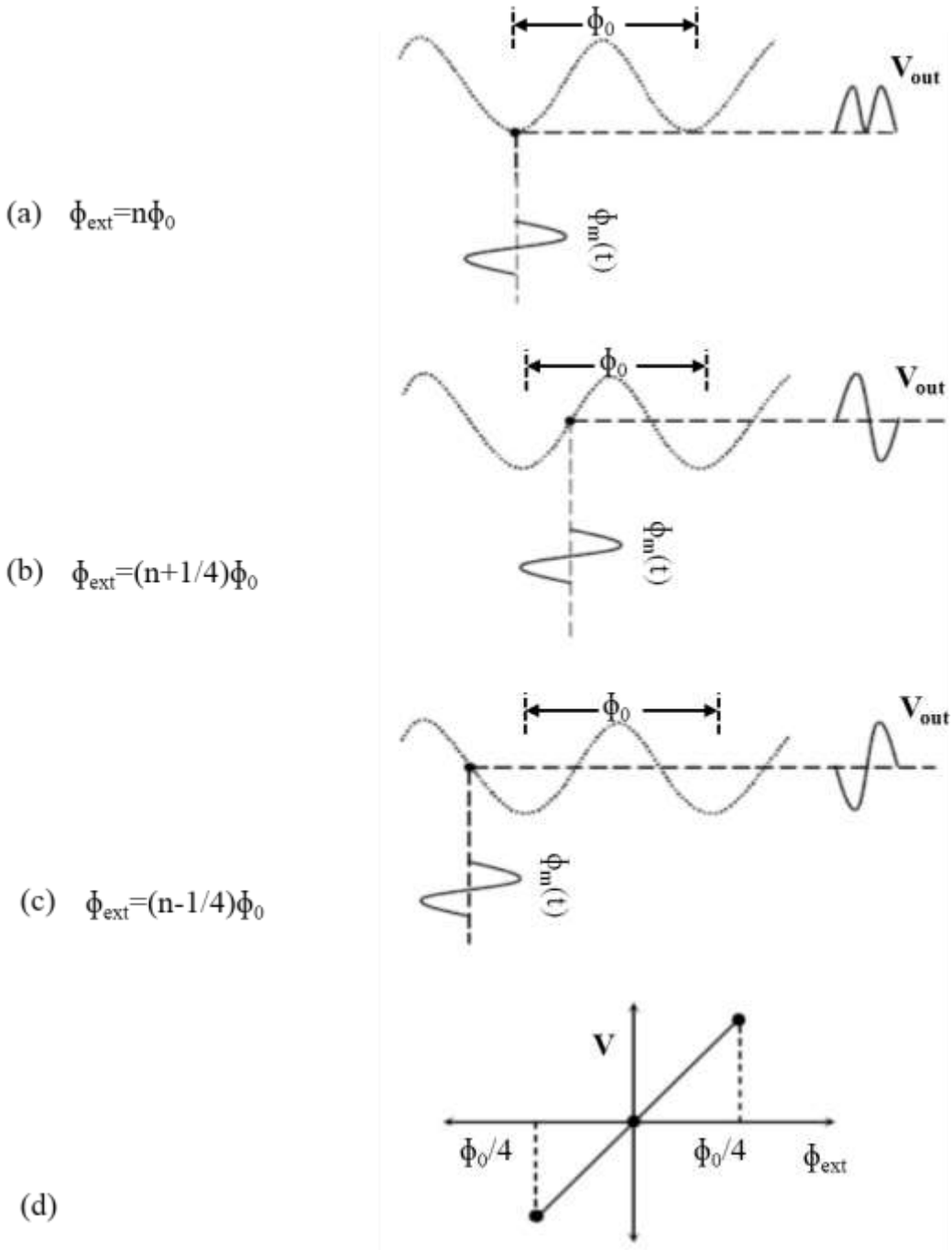

Figure 2.6 Schematic of the flux modulation scheme. (a) When signal flux $\phi_{ext}=n\phi_0$, the frequency of the SQUID output is twice the modulation frequency (b) When signal flux $\phi_{ext}=(n+1/4)\phi_0$, the frequency of the SQUID output is same as the frequency of the modulation signal and both are in phase (c) When signal flux $\phi_{ext}=(n-1/4)\phi_0$, the frequency of the SQUID output is same as the frequency of the modulation signal and there is a 180^0 phase difference between the two (d) Linearly varying FLL output which is phase sensitively detected at the modulation frequency.

the working point W since the feedback flux tends to cancel the signal flux and provides a measure of the signal flux to be detected. The voltage across the feedback resistor (R_f) is taken to be the SQUID output voltage, which is proportional to the signal flux required to be detected.

In the FLL mode, the signal bandwidth gets limited to frequencies lower than the modulation frequency. However, this does not pose a serious limitation in biomagnetic field measurements, since a bandwidth of ~1 kHz suffices for most of the applications. In the FLL mode, the total magnetic flux noise of the DC SQUID is given by [4]:

$$S_{\Phi}^{\frac{1}{2}} = \sqrt{S_{\Phi,SQUID} + \frac{S_{V,AMPL}}{V_{\Phi}^2}} \tag{2.3}$$

where $S_{\Phi,SQUID}$ and $S_{V,AMPL}$ are the flux noise of the SQUID and voltage noise of the preamplifier respectively and V_ϕ ($=\partial V/\partial \Phi$) is the flux-to-voltage transfer function of the bare SQUID. It may be noted that, higher the flux-to-voltage transfer ratio V_ϕ, better is the SNR for any SQUID based measurement.

2.3 Reduction of ambient magnetic noise

As mentioned in chapter 1, the customary way of overcoming the parasitic ambient magnetic noise affecting a typical MCG measurement is by recording the magnetocardiogram inside a magnetically shielded enclosure. Another common means of suppressing the noise is by using superconducting pick-up loops in the form of gradiometers. In the following sections, we give a brief description of the MSR and the gradiometers that have been used in the present study.

2.3.1 Magnetically shielded room(MSR)

(a)

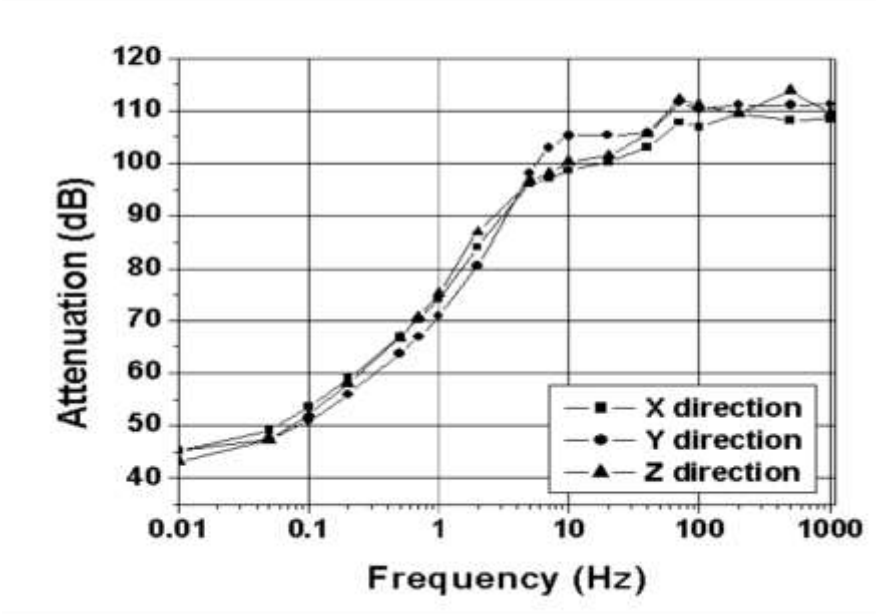

(b)

Figure 2.7 (a) Photograph of the MSR used for shielding external ambient magnetic noise (b) Measured shielding factor for the MSR as a function of frequency for each of the three mutually orthogonal components of the magnetic field along *X*, *Y* and *Z* directions. It may be noted that, the MSR provides a shielding factor of ~70 dB at 1 Hz and ~110 dB at 100Hz and beyond.

Figure 2.7 (a) shows a photograph of the Magnetically shielded room(MSR) which was custom built by IMEDCO, Switzerland and assembled in our laboratory at IGCAR for different types of

biomagnetic field measurements including MCG. The MSR has internal dimensions of 3 m (width) ×4 m (length) ×2.4 m (height) and is constructed using two layers of mu-metal and two layers of aluminum on each of the six sides. The outer mu-metal layer is 2 mm thick and the outer aluminum layer is 4 mm thick. The inner mu-metal layer is 3 mm thick and the inner aluminum layer is 8 mm thick. The principles of magnetic shielding provided by mu-metal and aluminum layers are as follows [3]:

High frequency electromagnetic noise is attenuated by the eddy currents induced across the grounded high electrical conductivity aluminum panels following Lenz's law, since the induced eddy currents produce secondary magnetic fields in a direction opposite to the primary magnetic noise. While this eddy current shielding is reasonably effective at high frequencies, it fails to be effective at low frequencies owing to an inevitable increase in skin depth at low frequencies. For low frequency magnetic shielding, ferromagnetic materials such as mu-metal are usually used for the construction of MSR. Since the mu-metal has very high magnetic permeability in comparison to air, it provides a path of exceedingly low magnetic reluctance to the magnetic lines of force. Consequently, the magnetic field lines are bunched up and are largely bypassed through the mu-metal walls of the MSR, which would have otherwise passed through the shielded region. In this way, the mu-metal shielding helps in reducing the density of magnetic flux lines inside the shielded region (typically by a factor of about 1000, depending on the frequency).

Quantitatively, the shielding effectiveness of a MSR is expressed in terms of shielding factor (S), which is given by:

$$S = 20 \log \frac{H_A}{H_R} \tag{2.4}$$

Here H_A is the magnitude of the externally applied known magnetic field outside the MSR and H_R is the corresponding residual field measured in the interior of the MSR. Since the attenuation

is frequency dependent, the shielding factor *S* also varies with frequency [8]. The shielding performance of the MSR along all the three mutually perpendicular directions (X, Y and Z) is shown as a function of frequency in figure 2.7 (b). The shielding factor provided by the MSR is about 70 dB at 1 Hz which increases to about 110 dB at 100 Hz and beyond [9]. This shielding provided by the MSR is sufficiently high to enable one to record MCG signals with a high SNR. It may be noted that, in the interest of exploring the possibility of a low cost MCG set-up in order to promote a routine use of the MCG technique in hospital environments, some of the MCG measurements quoted in the present study have also been recorded without using the MSR.

2.3.2 SQUID gradiometers

The gradiometers are effective in discriminating the signal of interest originating from nearby sources from the noise originating from more distant sources, and are widely used for suppressing the environmental interferences encountered in unshielded or partially shielded MCG measurements [10, 11]. Usually, the superconducting flux transformers, which are employed to couple the signal flux into the SQUID loop in order to increase the field sensitivity of the SQUID, are wound in the form of gradiometers (see figure 2.8). A n^{th} order gradiometer basically consists of a set of superconducting pick-up loops connected in such a way that the gradiometer is insensitive to all gradients of magnetic field up to and including the $(n\text{-}1)^{th}$ order, and produces a voltage output proportional to the gradient of n^{th} order. Gradiometric pick-up loops are thus relatively insensitive to distant sources of magnetic noise since such sources produce magnetic fields varying slowly in space so that such noise fields and their lower order spatial gradients tend to be uniform over the total volume occupied by the gradiometer coils. They offer high sensitivity for detection of magnetic fields from nearby sources since such nearby sources produce magnetic fields varying rapidly in space, and tend to display very strong spatial gradients.

The gradiometers sense the spatial gradient of the instantaneous magnetic field and couple it to the SQUID to generate a proportionate voltage output. Depending upon the type of spatial gradient sensed by the gradiometers, they can be classified into axial and planar types [12, 13]. The axial gradiometers measure the spatial gradient of the magnetic field along the direction normal to the plane of the pick-up loop, while planar gradiometers measure the spatial gradient of the magnetic field parallel to the plane of the pick-up loop. A first order axial gradiometer comprises of two parallel superconducting pickup loops with equal area, wound in opposition, and separated from each other along the common axis by a certain vertical separation between them known as the baseline (b) of the gradiometer. Out of these two loops, the loop placed nearer to the source is known as the signal loop since it detects the signal of interest while the other loop is known as the compensation loop since it serves to compensate any parasitic pick-up of noise from distant sources. In an ideal gradiometer, the screening current induced by a distant noise source into two different loops (signal loop and compensation loop) of the gradiometer is equal and opposite in direction so that the net screening current induced in the gradiometer is zero and hence no net flux is coupled to the SQUID by a distant noise source. On the other hand, a nearby source (such as cardiac source) ideally induces a strong screening current into the signal loop, but a much weaker screening current in the compensation loop, and the difference ultimately gets detected as the SQUID output. Different orders of gradiometers like first, second, third and so on could be constructed by varying the number of loops as well as the number of turns in the individual loops in an axial gradiometer. As an example, when the areas of all the loops are taken to be equal, a First Order Gradiometer consists of just two superconducting loops wound in opposition, and separated along their common axis by a baseline, whereas a Second Order Gradiometer usually consists of one loop wound counterclockwise at the bottom, two loops wound clockwise at the middle and one loop wound counterclockwise at the top. The higher order gradiometers can provide a better SNR by providing a greater attenuation of contribution

of the distant sources of noise [14]. For example, a first order axial gradiometer is usually insensitive to the uniform magnetic fields and yields an output proportional to the magnetic field gradient along the vertical direction ($\partial B_z/\partial z$), whereas a second order axial gradiometer senses the higher order gradient ($\partial^2 B_z/\partial z^2$) by cancelling the contribution of both the magnetic field as well as its first order gradient. It may not be appropriate to indefinitely increase the order of the gradiometer, however, as the strength of the detected signal may be affected while not significantly improving the SNR [3].

The planar gradiometers consist of two magnetometer loops placed in the same plane next to each other separated by a small baseline, and the difference of the magnetic flux coupled to the two magnetometer loops is measured as the gradiometer output. In other words, these gradiometers measure the off diagonal gradient or the gradient of *z* component of magnetic field along the two directions parallel to the plane of the pickup coil ($\partial B_z/\partial x, \partial B_z/\partial y$) [13].

The degree to which a gradiometer could reject a distant source of noise depends on the precise matching (balancing) of area and orientation of its loops. For a perfectly balanced symmetric First Order Gradiometer (FOG), the following condition should be met:

$$N_{signal}A_{signal}=N_{comp}A_{comp} \tag{2.5}$$

where N_{signal}, A_{signal} denote the number of turns in the signal loop and its area respectively and N_{comp}, A_{comp} denote the number of turns in the compensation loop and its area respectively. A perfectly balanced ideal FOG gives zero output when the magnetic field is uniform over the two loops of the gradiometer; in other words, it rejects uniform magnetic fields. However, if there is a mismatch in the effective areas of the two loops of a gradiometer, the perfect balance is lost and its output may be visualized as that of an ideal gradiometer together with a small magnetometer. With some effort, however, it has been conceivable to achieve a balance as high

as 1% to 0.1% while fabricating axial gradiometers by winding the superconducting wire in grooves precision machined on an insulating former [14]. This degree of balance translates into a noise cancellation capability of 99 % - 99.9 % for these gradiometers. It is possible to achieve a higher degree of balance (by a factor of 10 or more) using planar gradiometers as they can be fabricated to precise dimensions using thin-film technology and photolithography [14].

As an alternative to wire wound gradiometers, electronic gradiometer can be incorporated for cancelling the distant sources of noise in magnetocardiography [10]. In this configuration, two magnetometers are used with the required baseline gap between them and the individual magnetometer output signals are subtracted (either by analog or digital technique) to realize an equivalent of a first order axial gradiometer. In order to realize an n^{th} order gradiometer, $(n+1)$ magnetometers are required in this technique, and outputs of these $(n+1)$ magnetometers have to be suitably combined with specially chosen numerical coefficients to realize an equivalent of n^{th} order gradiometer. Since each magnetometer output has to be read by the corresponding electronics, system may become more complex than the wire wound gradiometer connected to a single SQUID device. Ensuring the stability of each magnetometer with respect to dynamic range and slew rate may also be difficult at noisy measurement sites.

In the present work, all the MCG experiments were performed using SQUID sensors inductively coupled to wire wound axial FOG. A detailed account of evaluating the calibration factor and the spectral density of noise of the SQUID coupled to the FOG is furnished below.

2.3.2.1 Field gradient-to-voltage calibration for SQUID gradiometer

The output of the SQUID sensor inductively coupled to the pick-up coil has to be properly calibrated in advance before performing any biomagnetic field measurement, so that the magnetic field signal of interest or its axial gradient can be correctly inferred from the measured output

voltage. Commonly, calibration of a SQUID gradiometer is performed by relating its measured voltage output to the value of a known external magnetic field gradient produced by a known reference system, and the corresponding calibration factor is expressed in terms of voltage/field gradient. Although various procedures could be adopted for this purpose, a relatively simple yet an effective procedure has been used in the present study for calibrating the FOGs [8, 15] used for MCG measurements in the present study.

A large circular current carrying coil with a diameter nearly 20 times larger than that of the superconducting gradiometer coil was placed near the tail of the liquid helium dewar housing the SQUID gradiometer to be calibrated. This coil was used for generating a known magnetic field (or field gradient) and coupling it to the SQUID sensor as a proportionate magnetic flux. In this arrangement, the axis of the coil was aligned along the axis of the gradiometer and its position was adjusted until a maximum output from the SQUID gradiometer was obtained. From Biot-Savart's law, the magnitude of the magnetic field at a distance *z* from the axis of a circular current carrying coil is given by [15]:

$$B_z(x = 0, y = 0, z) = \frac{\mu_0 N I a^2}{2(a^2+z^2)^{3/2}} \tag{2.6}$$

The corresponding magnetic field gradient along the *z* direction is given by:

$$\frac{\partial B_z}{\partial z}(x = 0, y = 0, z) = -3\frac{\mu_0 N I a^2 z}{2(a^2+z^2)^{5/2}} \tag{2.7}$$

Where *N* is the number of turns in the large circular coil, *I* is the current passed through the coil, *a* is the radius of the coil and *z* is the distance between the sensor and the center of the coil along the vertical axis. The input magnetic field and the field gradient at the location of the gradiometer could be varied by changing the input current *I* (which could be varied by adjusting the sinusoidal voltage output of the signal generator connected to the circular coil) or by varying the distance z

between the sensor and the coil (which could be varied by displacing the cryostat along the vertical direction) and the corresponding voltage outputs from the SQUID gradiometer could be

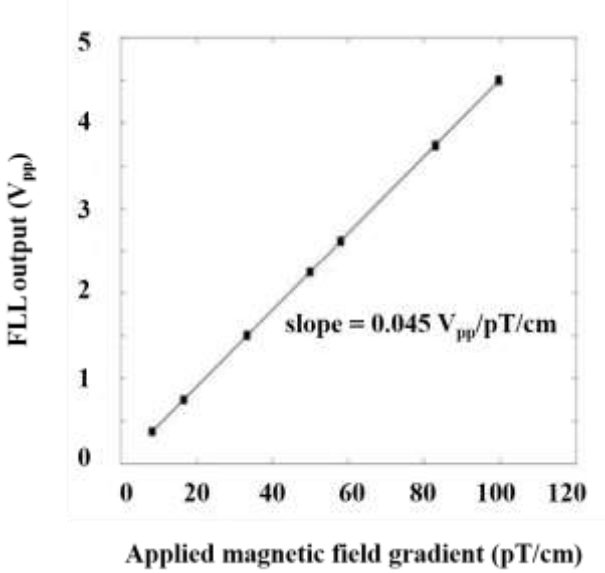

Figure 2.8 The field gradient-to-voltage calibration plot for a typical SQUID gradiometer. A known value of magnetic field gradient has been applied to the sensor by passing sinusoidally varying current of known amplitude through a large circular coil and the corresponding FLL output is recorded. The experiment is repeated for different values of applied magnetic field gradient. The slope of the plot of FLL output as a function of input magnetic field gradient yielded the calibration factor which is used for converting the measured SQUID output voltage into the corresponding magnetic field gradient.

recorded. These measurements showed a linear variation of the output voltage with the input magnetic field gradient as shown in figure 2.8. The slope of this calibration plot gives the calibration factor for the corresponding gradiometer. The calibration factor for the presently used gradiometer with a loop diameter of 15 mm and a baseline of 50 mm was found to be 22.2 pT/cm/V.

2.3.2.2 Field gradient noise level in the SQUID system

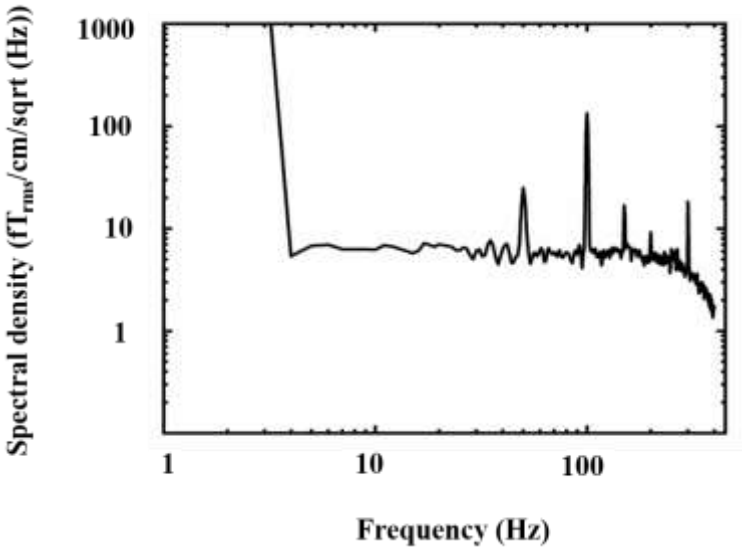

Figure 2.9 The power spectral density plot of magnetic field noise for a typical SQUID sensor coupled to a first order axial gradiometer (baseline 50 mm and loop diameter 15 mm) with output voltage low pass filtered at 300 Hz. Various low frequency noise peaks corresponding to noise associated with vibrations and power line interference could be observed.

For a signal of interest to be measurable, it is important that its amplitude is larger than the sensitivity of the sensor in the required bandwidth. In case of SQUID based systems, the sensitivity is usually limited by the intrinsic noise of the SQUID and the extrinsic noise associated with electronic units, residual ambient magnetic noise, noise associated with vibrations etc. Hence, the background noise (the environmental noise in the absence of the subject) measured using an axial FOG inside the Magnetically shielded roommust be lower than the signal of interest and, in particular, should not exceed several $fT_{rms}/cm/\sqrt{Hz}$ (which represents the spectral density of the noise content in the unit frequency bandwidth) in order to sense all the features of a cardiac signal (from adult as well as fetal hearts). Figure 2.9 shows the typical variation of the spectral density of noise with frequency measured using a SQUID sensor connected to a FOG type pick up coil. The output noise comprises of white noise, noise at power line frequencies and its harmonics as well as low frequency noise associated with various other sources. 1/f noise is

seen to dominate at very low frequencies (< 4 Hz), The average field gradient noise level measured above 10 Hz for the FOGs with loop diameter 15 mm and baseline 50 mm was found to be ~ 3 $fT_{rms}/cm/\sqrt{Hz}$. The field gradient noise measured by the FOGs could be converted into an equivalent magnetic field noise by multiplying the field gradient noise with the baseline of the gradiometer [8]. Accordingly, the average magnetic field noise of our MCG system is inferred to be ~ 15 $fT_{rms}/\sqrt{Hz}$.

2.4 MCG cryostat and the SQUID insert

As already mentioned, the LTSC SQUIDs used in the present study are operated by immersing them inside liquid helium, which has a boiling point of 4.2 K at normal atmospheric pressure. The cryogenic liquids such as liquid helium need to be stored in some specially designed vessels (cryostats and dewars) to reduce their boil-off rate by minimizing the heat leaks associated with thermal conduction, convection and radiation and achieve a sufficiently long holding time for liquid helium for the proposed experiments [3, 8, 16].

While performing the MCG measurements, the liquid helium cryostat housing the SQUID sensors is placed at the measurement site and is supported by a non-magnetic gantry, which also allows the cryostat to move vertically along *z* axis for adjusting the position of the cryostat above the thorax of the subject depending on the experimental requirements. As mentioned earlier, the MCG systems at IGCAR comprise of three different MCG systems with progressively increasing number of channels: four channel system, thirteen channel system and thirtyseven-channel system. Here each SQUID channel consists of an axial First Order Gradiometer, a DC SQUID, a FLL module, an analog-to-digital converter (ADC) module for digitizing the data, and a display module which displays the channel output as a function of time on a personal computer. These individual modules (units) are identical for all the MCG systems with different number of channels. However, there are certain variations among the different MCG systems in use at

IGCAR related to the overall size of the fibre reinforced plastic (FRP) cryostats, number of SQUID gradiometers mounted inside the cryostat, inter-sensor spacing, the number of channels in the data acquisition system hardware etc. Table 2.1 lists the important features of the different MCG systems in use at IGCAR. The photographs of the 4 channel, 13 channel and 37 channel MCG systems are respectively shown in figure 2.10 (a), (b) and (c).

The 4, 13 and 37 channel MCG systems were assembled in liquid helium cryostats capable of

Table 2.1 The different MCG systems presently operational at IGCAR, Kalpakkam. While the individual modules are identical for MCG systems with different channels, there are variations in the size of the cryostat, the number of SQUID gradiometers, inter-sensor spacing, the number of data acquisition channels etc.

No. of channels	Liquid Helium Capacity (litres)	Warm-to-Cold distance (mm)	Liquid He boil-off rate (litres/day)	Area covered on thorax (cm^2)	Geometrical configuration of sensor array	Inter-sensor spacing (mm)
4	11.5	10	2	40	square	42
13	13	10	3	106	hexagonal	28
37	18	16	5	300	hexagonal	30

holding a maximum of 11.5, 13 and 18 liters of liquid helium respectively. The evaporation rates of the cryostats dictate the holding time of liquid helium and are listed in table 2.1. The inter-sensor spacing and the geometrical coverage of the sensor array for each of the MCG cryostats, which ultimately determine the spatial sampling of the magnetic field signal and the total coverage area over the thorax, are also tabulated in table 2.1.

Since the magnetic field decreases as one moves away from the source, it is essential that the sensors are located as close as possible to the source of interest in order to achieve a high Signal-to-Noise ratio for the corresponding measurement. For a MCG cryostat, it is therefore desirable to bring the signal pick-up coil of the gradiometer at liquid helium temperature as close as possible to the subject at room temperature by minimizing the warm-to-cold distance

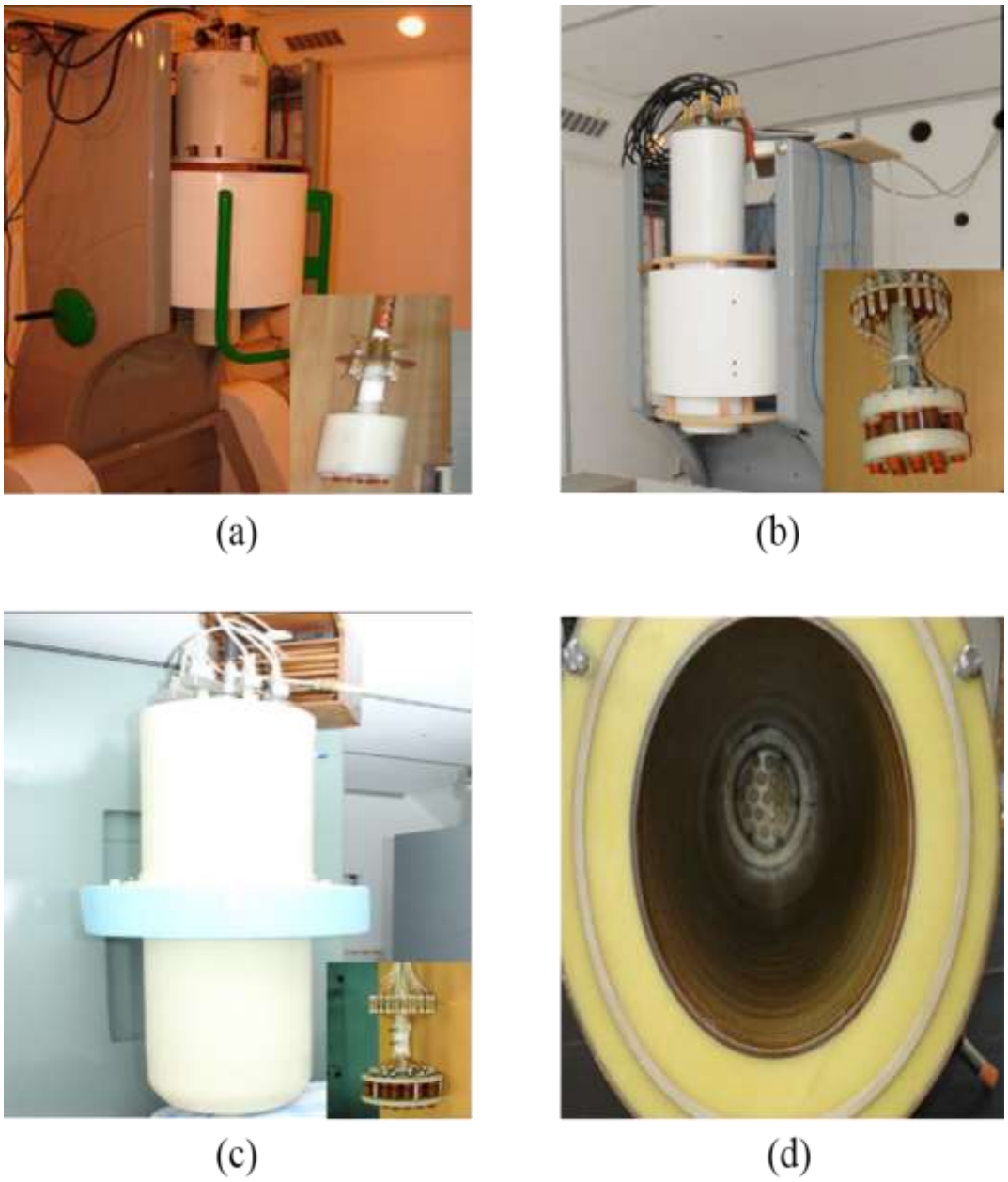

Figure 2.10 (a) The photograph of the four channel system; the inset shows the SQUID holder in which the first order axial gradiometers are housed in a square configuration with an inter-sensor spacing of 42 mm (b) The photograph of the thirteen channel system; the inset shows the SQUID holder in which the First Order Gradiometers are arranged in a hexagonal configuration with an inter-sensor spacing of 28 mm (c) The photograph of the thirty-seven channel system; the inset shows the SQUID holder in which the First Order Gradiometers are arranged in a hexagonal configuration with an inter-sensor spacing of 30 mm (d) The photograph of the top view of the thirteen channel liquid helium cryostat showing the recesses (for positioning the gradiometers) provided on the bottom flange of the liquid helium vessel.

of the cryostat. For this purpose, bottom flange of the liquid helium vessel is provided with a number of recesses in which the gradiometers are located. In this way, the sensors could be fitted to sit snugly into the recesses with only a minimum distance to the thorax of the subject at room temperature. The warm-to-cold distance for the four channel and thirteen channel cryostats is about 10 mm, whereas it is 16 mm for the thirtyseven channel cryostat.

Use of cryostats having lower number of channels (such as four and thirteen channel systems) may require sequential measurements in multiple configurations of sensor positions over the thorax to cover the entire thoracic area of interest. This way of performing MCG measurement may lead to errors owing to the inherent inaccuracies in positioning of the sensors during sequential measurements, which may also take a long time to complete the scan over the entire thoracic area. However, using the thirtyseven channel cryostat, it is possible to record the MCG signals covering the entire anterior thorax of a typical subject in just a single run and by obviating the requirement of sequential scanning, it enables the MCG scans to be performed much faster. As the sensor positions inside the 37 channel cryostat are accurately known, the error in the source reconstruction from the MCG data measured using the 37 channel cryostat is considerably lower compared to the measurements performed using other MCG systems with lower number of channels [17].

For each cryostat, suitable inserts were designed to allow the gradiometers to be mounted on the SQUID holders, and lowered into the cryostat in such a way that each gradiometer fits snugly into the corresponding recess on the bottom flange of the liquid helium vessel. The insert, fabricated out of fiber-reinforced plastic (FRP), is furnished with a set of mounting plates to support the SQUID gradiometers at the bottom and the LEMO electrical connectors (which is used to connect the electrical leads of the SQUID) at the top. Each gradiometer, consisting of two oppositely wound superconducting loops with diameter of 15 mm and baseline of 50 mm,

was connected via superconducting contacts to the input coil of the SQUID device, which is integrated on-chip. The insert was also provided with radiation baffles to reduce the boil-off of liquid helium by minimizing the radiative heat leak into the cryostat. Figure 2.11 shows the photograph of the insert designed and fabricated for the four channel system. The insert and the SQUID holder are configured in such a way that as the insert is carefully lowered into the cryostat, each gradiometer sits gently into the recess provided at the bottom flange of the liquid helium vessel, thereby bringing the sensors as close as possible to the subject's thorax.

2.5 SQUID electrical leads

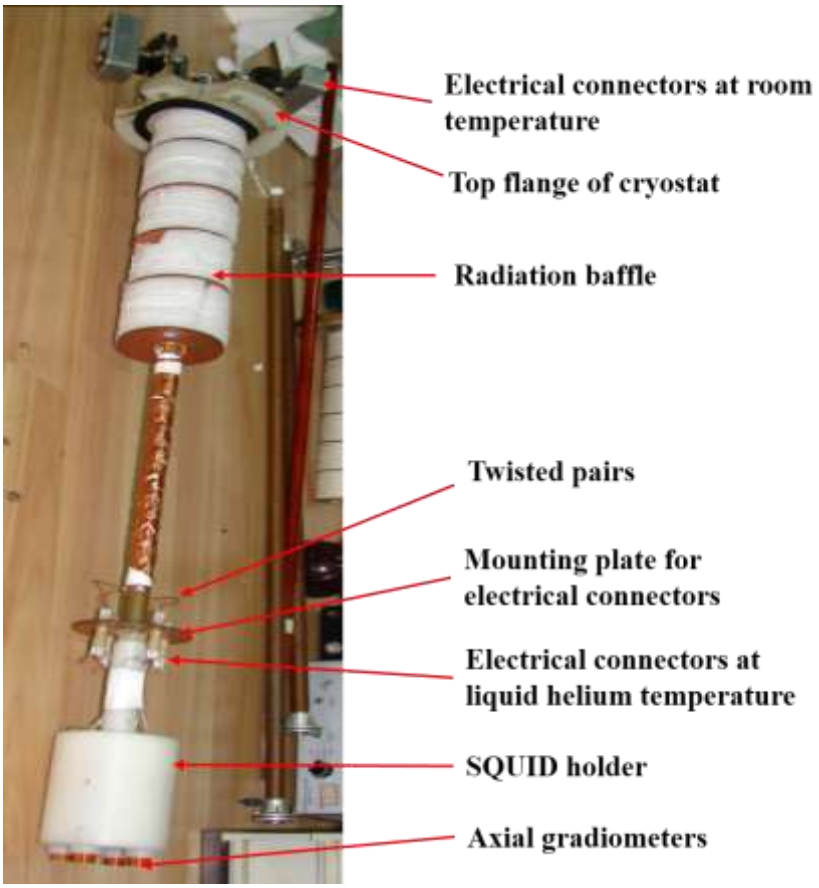

Figure 2.11 Photograph of the insert of the four channel MCG system that comprises of SQUID holder, electrical connectors, radiation baffles, mounting plates etc. The first order axial gradiometers are mounted on the SQUID holder in a square configuration with an inter-sensor spacing of 42 mm. The whole assembly is inserted inside the four channel cryostat.

Each SQUID module is usually connected with four twisted pairs of electrical leads, one pair each for bias current, flux modulation, heater and SQUID output voltage. The twisted pairs

provide a significant immunity to the measured signal against possible contamination from various sources of inductively coupled noise. 40 SWG low resistive (~ 1 Ωm^{-1}) copper wires are used for bias current and output voltage leads, whereas40 SWG high resistive (~ 35 Ωm^{-1}) manganin wires are used for flux modulation and heater leads. Low resistive copper wires were used for the SQUID output voltage leads of the SQUID to reduce the possibility of any signal loss, especially when the relatively low impedance of the SQUID sensor has to be matched to the source impedance of the preamplifier using an impedance matching transformer in order to operate the preamplifier with an optimal noise performance. High resistive manganin wires with low thermal conductivity were used for flux modulation and heater leads to minimize the heat leak into the cryostat, thereby reducing the boil-off rate of liquid helium and increasing the holding time of the cryostat. Occasionally, the magnetic flux could get trapped in the vicinity of the Josephson junctions of the SQUID sensors in the form of vortices leading to a reduction in critical current of the SQUID as a result of flux-trapping. Such flux trapping results in an undesirable reduction of the modulation depth of the SQUID. In such a case, the heater may be activated for a few seconds by passing a current through the heater in order to raise the temperature of the SQUID sensor above the superconducting transition temperature T_c, so that the trapped flux could be removed and the critical current as well as the modulation depth of the SQUID could be restored to their original optimum values when the SQUID sensor is cooled to its operating temperature of 4.2K after switching off the heater. The output voltage signals from all the channels are first brought to the electrical connectors fixed over the mounting plate inside the insert and then transferred to the electrical connectors at the top of the insert by twisted pairs of electrical leads.

2.6 Radio Frequency Shielded Room (RFSR)

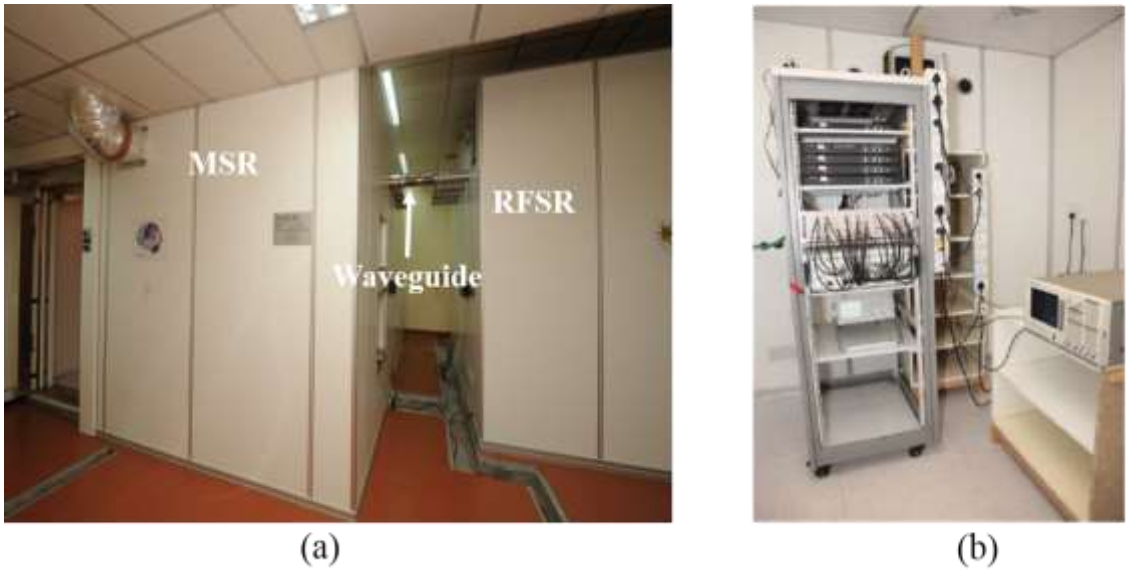

Figure 2.12 (a) Photograph of the Radio Frequency Shielded Room (RFSR) connected to the magnetically shielded room (MSR) via waveguides (b) A view of the electronic instrumentation kept inside the RFSR. The RFSR offers shielding against high frequency noise with a shielding factor of ~100 dB at 1 MHz and beyond.

After linearization, the output voltages from all the SQUID channels are routed via shielded cables from the MSR to the adjoining Radio Frequency Shielded Room (RFSR) through four large waveguides, each of 100mm diameter. All the necessary electronic equipment for analog-to-digital conversion and data acquisition are located inside the RFSR. A photograph of the RFSR and the way it is connected to the MSR is shown in figure 2.12 (a). As shown in figure 2.12 (b), the RFSR houses all the electronic instrumentation requiring mains power supply such as the control units for FLL, ADC modules to digitize the SQUID output voltage of each channel, waveform generators, oscilloscopes, spectrum analyzer and other test and measuring apparatus required for the proposed experiment. The RFSR is constructed using 2 mm thick aluminum plates with high electrical conductivity and it provides a shielding factor of about 100 dB at frequencies of 1 MHz and beyond. All the electronic equipments located inside the RFSR derive

mains power from a special isolation transformer, located far away from the MSR and RFSR and the 220 V, AC power enters the RFSR via a filter.

The digitized output data of all the SQUID channels is transmitted to a data acquisition PC (DAQ PC) located in the unshielded area over a fiber optic cable through a port provided for this purpose on the rear wall of the RFSR. The fibre optic cable is capable of supporting digital data transfer rates upto75 Mbps, while being immune to possible contamination by the ambient electromagnetic noise.

2.7 Data acquisition system

At the final output stage, the FLL voltage output of each SQUID channel, may be low pass filtered with user desired cut-off frequency, which may be set at any of the four values: 30 Hz, 100 Hz, 300 Hz or 1 kHz, depending on the specific experimental needs [9]. The FLL output voltage from each channel could be digitized using individual Delta-Sigma ADC with 24 bit resolution at any user desired sampling rate up to 200 kHz. However, a sampling rate of 1 kHz usually suffices for most of the biomagnetic signal measurements. The digitized data received from the ADC via the optical fiber link is stored in a server class PC, which is equipped with custom-designed data acquisition and display software. This LABVIEW based display platform enables real-time graphical display of acquired signals as a function of time, with optional user defined modules for low pass, high pass or band pass filtering for possible use depending on the specific experimental requirements. Apart from just visualizing the data in time domain, it is also possible to investigate the spectral contents of the acquired signal in frequency domain using the software. A module is also provided in the software for trigger based epoching and averaging to suppress the uncorrelated noise, which is important for improving the Signal-to-Noise ratio of the measured biomagnetic signal. The output data of all the channels along with the experimental details as well as the sensor coordinates are stored in the DAQ PC for further off-line analysis.

2.8 MCG measurement

Prior to the recording of MCG, the bias current through the SQUID is adjusted to give optimum modulation depth when a modulation flux with an amplitude of $\Phi_0/4$ is applied (heater may be activated to detrap flux, if necessary, before setting the bias current to its optimal value). The SQUID sensors are locked to the working point by appropriate adjustments of circuit parameters and turning the feedback switch of flux-locked-loop electronics to "ON" position. The feedback resistor is selected to operate the flux-locked-loop circuit at a gain setting (V/Φ_0) as desired by the user. The subject is instructed to take out and deposit all the magnetic and metallic objects before entering inside the MSR since the existence of such objects in the vicinity of the cryostat is likely to be a potential source of avoidable magnetic noise. Next, the subject is positioned under the cryostat in a supine posture and the cryostat is adjusted along the vertical direction in such a way that there is minimum possible gap between the bottom (flat part) of the cryostat and the subject's thorax. However, care is taken to ensure that the cryostat does not touch the subject and that there is a clear gap between them. After the subject is positioned properly under the cryostat by aligning the sensor array with respect to various anatomical landmarks to ensure that the MCG measurements are performed at standardized positions on the thorax, the pneumatically operated door of the MSR is closed. Spatial distribution of cardiac magnetic field is sensed by an array of gradiometers housed inside the liquid helium cryostat and the data is digitized and transmitted over the optical fibre link to the server PC for the purpose of storage and real-time display. The MCG of the subject is thus automatically recorded and displayed on the server PC. Typically, our MCG recordings are performed at a sampling rate of 1 kHz and a low pass filter

(a)

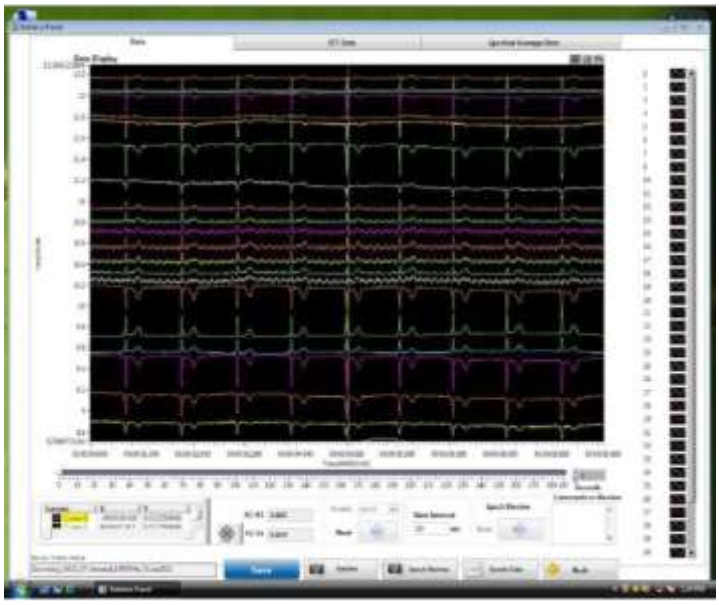

(b)

Figure 2.13 (a) Photograph of an ongoing MCG recording on a human subject using 37 channel MCG system inside the magnetically shielded room (MSR). The subject is positioned in such a way that, the sensors are just above the anterior thoracic surface (b) a screenshot of the recorded MCG getting displayed on the screen of the data acquisition computer. For clarity, only a few channels are shown on an expanded scale.

setting of 300 Hz for each channel. The FLL gain setting is fixed to be 5 V/ϕ_0. A photograph of the MCG recording in progress for a human subject using the 37 channel MCG system is shown

in figure 2.13 (a). Figure 2.13 (b) shows the photograph of the recorded MCG for the same subject as it is displayed on the monitor of the data acquisition system PC.

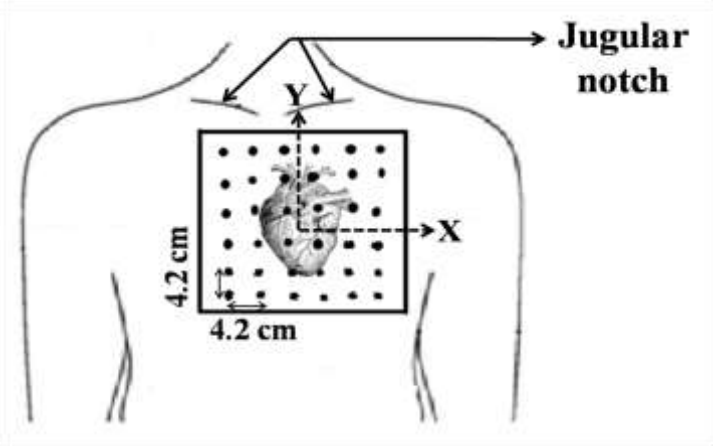

Figure 2.14 A (21 cm×21cm) paper grid used for sequential scanning of MCG recordings. The grid is pasted over the chest of the subject with respect to standard anatomical landmarks as indicated. The origin of the coordinate system lies at the centre of the grid.

Although it is easier and less time consuming to perform a MCG scan covering the entire thoracic area in a single measurement session using the large 37 channel MCG system, it may also be sometimes desirable to perform the MCG measurements using the smaller 4 or 13 channel MCG systems for other advantages including ease of use and portability, even though sequential measurements are required in this case for covering the entire thoracic area by repeated repositioning of the subject relative to the sensor array. In the present study, the 4 channel MCG system (apart from the 37 channel system) has been used for carrying out several MCG measurements and the procedure of performing a complete MCG scan covering the entire thoracic area of interest using such a system is described below.

The MCG scan is performed by recording MCG on the subject's chest by sequentially repositioning the subject relative to the cryostat at nine different positions so that MCG is recorded at a total of 36 locations on a 6×6 square lattice covering a total area of 21 cm×21 cm on the chest as shown in fig 2.14. The 6×6 grid is usually drawn on a sheet of paper and is pasted

over the subject's chest by aligning the grid with respect to various anatomical landmarks on the chest to ensure that the MCG measurements are always performed at standardized and reproducible positions on the subject's chest. Fig 2.14 shows the grid pattern of the measurement positions superimposed on a representation of chest surface to indicate the typical measurement locations relative to the heart.

2.9 Preprocessing of MCG signal

The MCG signal measured inside a MSR may still be contaminated by some residual magnetic noise and also the noise specific to the subject such as artifacts related to his breathing and motion etc. Further, possible imbalance in practical gradiometers may also contribute a component of noise at the output. The reduction of such sources of noise is usually carried out by preprocessing the signal using various software based denoising techniques. Several of these software based denoising algorithms such as smoothing, filtering, averaging, wavelet transform, principal component analysis (PCA), independent component analysis (ICA), adaptive filtering etc., that are being used for denoising the ECG signal, can be implemented for preprocessing the MCG signal as well, as both the signals share similar morphological features. It may be noted that each of these techniques has its own advantages and disadvantages. In the present case of MCG recorded inside the MSR, we have primarily relied upon wavelet transform, ICA, averaging technique and occasionally on filtering and smoothing for denoising the recorded MCG signal. A brief discussion on each of these techniques is given below [18-21].

(a) Trigger lock averaging

This time domain based signal denoising technique is conventionally used for eliminating the uncorrelated noise in measured MCG data. In this method, a large number of nominally identical cardiac cycles are epoched and aligned with respect to a chosen fiducial reference point. For convenience, the time instants of occurrence of the R wave peaks on the cardiac cycle may be

chosen for this purpose. The aligned epochs are then averaged to suppress the uncorrelated noise. The method relies on the fact that the signal components are identical across all the epochs and survive even after averaging, while the noise components are inherently random and hence tend to vanish after averaging a large number of cardiac cycles. The SNR of the denoised signal improves by a factor of $\sqrt{N}$, where N is the number of cardiac cycles (beats) taken for averaging. Any inter-beat variation in the cardiac signal may, however, get lost during the averaging procedure, which replaces N nominally identical cardiac cycles measured at a particular location on the chest by a single averaged cardiac cycle representative of the cardiac waveform at that location.

(b) Filtering

In filtering, the frequency components other than those corresponding to the signal of interest can be eliminated by carefully selecting the bandwidth of the output filter using the available filter settings which may include the low pass, high pass, band pass, band stop, notch filtering etc. This method eliminates noise by allowing signal within the selected bandwidth to pass through, while preventing noise outside the selected bandwidth. However, such techniques based on Fourier decomposition cannot be expected to satisfactorily denoise nonlinear, non-stationary signals such as MCG, as the measurement bandwidth of MCG signal often overlaps with the noise and, hence, the application of this simple filtering technique may actually distort the signal features.

(c) Wavelet transform

The use of Fourier transform is neither very effective nor very efficient in analyzing non-stationary signals such as MCG, since it can only identify the various frequency components present in the measured signal with no information on the time of occurrence of these components along the measured time-series. However, the wavelet transform performs a time frequency

decomposition of the measured signal, thereby allowing preservation of the required local features of the signal components and discarding the noise components. In this technique, the signal is decomposed into a linear combination of a set of basis functions known as wavelets which are localized in both time and frequency domains. The wavelet is usually a localized oscillatory waveform with the different basis functions of the set being related to each other by operations such as shifting and scaling. Thus, the wavelet transform technique decomposes the measured signal into components corresponding to different time scales and enables the use of a temporal resolution which is appropriate to each time scale. As the wavelet coefficients corresponding to different components represent the energy contents of the respective wavelets, the wavelet coefficients with higher amplitude may be taken to correspond to the signal of interest and the wavelet coefficients with lower amplitude may be taken to correspond to noise. While denoising, these wavelet coefficients with small amplitudes corresponding to noise components are suppressed by applying a thresholding technique. Finally, the inverse wavelet transform technique is used to reconstruct the denoised signal from the remaining wavelet components using the processed wavelet coefficients.

(d) Independent component analysis (ICA)

This is a statistical approach for denoising the signal by visualizing the measured signal as an admixture of statistically independent components (including noise). When multichannel MCG measurements are performed, each channel output is actually an admixture of a signal due to cardiac activity and noise arising from different sources; thus, multiple admixtures of signal and noise are available in the measured multichannel MCG data. ICA provides a method for unmixing these multiple admixtures into original components and recovering the denoised signal by suppressing the components attributed to noise during the signal reconstruction phase. The independent components are identified by requiring that a suitably selected measure of non-

Gaussianity is maximized when the measured admixtures of independent components are unmixed. This method is limited by the requirement that the number of measurement channels should be necessarily more than the number of independent components; however, this limitation is not very restrictive in the context of multichannel MCG data with a large number of channels.

2.10 Interpretation of MCG signal

Figure 2.15 (a) shows the spatial distribution of the denoised MCG traces measured over 36 locations on the chest. It may be noted that the signal polarity at the R peak instant is positive in the upper right half of the figure, but is negative in the lower right half. These time series MCG signals could be interpreted in several ways for gaining a better understanding of the underlying cardiac electrical activity or for obtaining additional insights. Some of the conventional methods for further analysis and interpretation of the measured MCG data include construction of Magnetic field map and Pseudo-Current Density map for visualization of data as well as eventual localization of the cardiac source [22-24]. A brief discussion on each of these techniques is provided below.

(a) Magnetic field map (MFM)

A Magnetic field map (MFM) or an iso-field contour map forms an empirical way of visualizing the measured magnetic field distribution produced by the cardiac source. For any given time instant on the cardiac cycle, MFM is generated by spatial interpolation of the measured MCG data followed by joining the spatial locations with identical magnetic field values over the thorax by smooth iso-field contour lines. As a convention, the magnetic fields coming out of the chest are taken as positive and assigned red color in the MFM, whereas those entering into the chest

are assumed to be negative and are assigned blue color in the MFM. Presuming the cardiac source to be dipolar, the strength of the magnetic field for both positive and negative maxima on the MFM should be equal for a healthy heart. Figure 2.15 (b) shows the MFM generated for the normal subject at the T peak time instant of the cardiac cycle. MFM provides various quantitative measures which can be used to classify healthy and unhealthy subjects. Typical parameters include maximum current angle, field map angle, maximum to minimum field ratio etc. The maximum current angle (θ_c) is defined as the angle subtended by the current dipole with respect to a horizontal reference line passing through the center of the MFM (Fig 2.15(b)). The field map angle (θ_m) refers to the angle subtended by the line connecting the two extrema of the MFM with

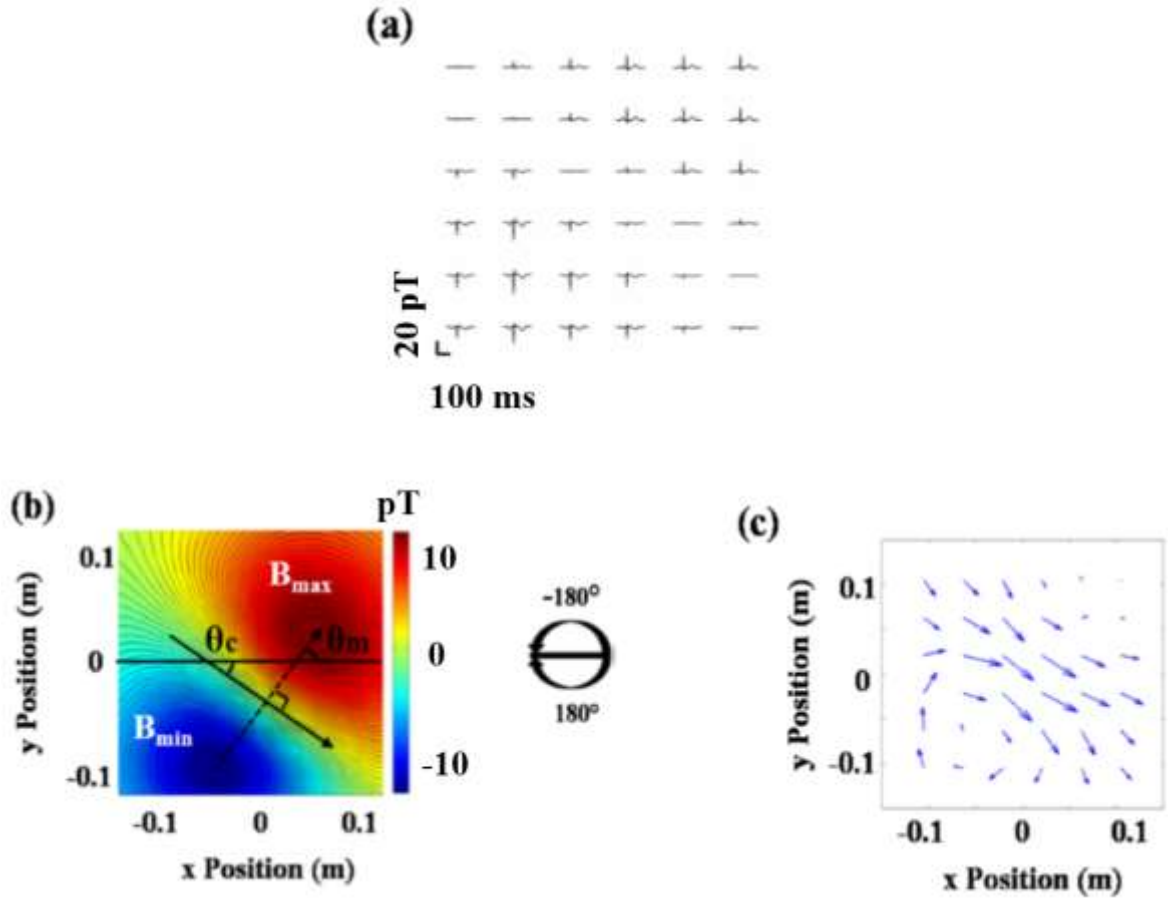

Figure 2.15 (a) spatial distribution of averaged cardiac traces over 36 locations of a normal subject (b) MFM constructed at the T peak time instant of the cardiac cycle illustrating an approximately dipolar pattern. Measurement of maximum current angle and field map angle is depicted (c) PCD map for the corresponding MFM plotted by taking the spatial gradient of the MFM.

respect to the reference line. A convention has been adopted to assign positive sign for angles traversed clockwise and to assign negative sign for angles traversed anticlockwise, where all the angles are calculated starting from the extreme right end of the reference line. The maximum to minimum field ratio is defined as the ratio of the magnitudes of the maxima and minima of magnetic fields in the Magnetic field map. It is to be noted that, for an MFM generated at the T peak instant of the cardiac cycle of a normal subject, the maximum current angle is found to be between -5^0 to 77^0, field map angle is found to be between -86^0 to -45^0 and the maximum to minimum field ratio is found to be between 0.5 to 1 [22]. Deviation of the MFM from its expected morphology and deviation of these derived parameters from their standard ranges of values could possibly indicate the presence of one or more cardiac disorders.

(b) Pseudo-current density (PCD) map

A PCD map provides another way to visualize the current source responsible for the measured cardiac magnetic field distribution at each instant of time during the cardiac cycle. However, it yields more quantitative information on the possible distribution of cardiac currents when compared to the MFM. Here, the underlying cardiac source could be visualized by taking the spatial gradient of the measured magnetic field distribution over the thorax. The magnitude and orientation of the pseudo currents $\vec{c}\ (x, y)$ in a PCD map is given by the equation [23]:

$$\vec{c}(x, y) = \frac{\partial B}{\partial y}\vec{e}_x - \frac{\partial B}{\partial x}\vec{e}_y \qquad (2.8)$$

where $\vec{e}_x$ and $\vec{e}_y$ are the unit vectors along *x* and *y* directions respectively and *B* represents the measured normal component of the magnetic field. Figure 2.15 (c) shows the PCD map obtained by taking the spatial gradient of the MFM shown in figure 2.15 (b).

(c) Source localization

The measured spatial distribution of cardiac magnetic field can be used to localize the underlying cardiac source at each instant of time using a suitable model for the source and calculating the source parameters which best fit the measured data. Reconstruction of the source from the measured magnetic field distribution is known as the inverse problem. This method may be considered to be a reliable way of diagnosing various cardiac problems if the assumed source model represents an accurate description of the underlying physical reality. The inverse problem in the context of MCG may be formulated as a standard optimization problem, where the source parameter values are determined by minimizing the sum of squares of the residual differences between the measured magnetic field and the magnetic field calculated using the assumed model at the location of each channel [24]. Various local and global search methods such as Nelder-Mead, pattern search, genetic algorithm, simulated annealing etc. could be useful in this context for calculating the optimal values of source parameters.

References

1. C Parasakthi, R Patel, S Sengottuvel, N Mariyappa, K Gireesan, M Janawadkar and T Radhakrishnan. Establishment of 37 channel SQUID system for magnetocardiography. *AIP Conf Proc*. **1447** (2012) 871-872.

2. A Braginski and J Clarke. "Introduction" in The SQUID handbook – Fundamentals and Technology of SQUIDs and SQUID systems – Vol I. *WILEY-VCH, 2004*.

3. R Fagalay. Superconducting quantum interference device instruments and applications. *Rev Sci Instrum.* **77** (2006) 101101 doi:10.1063/1.2354545.

4. V Pizella, S Penna, C Gratta and G Romani. SQUID systems for biomagnetic imaging. *Supercond Sci Tech.* **14** (2001) R 79–R 114.

5. D Drung and M Muck. "SQUID Electronics" in: The SQUID Handbook – Fundamentals and Technology of SQUIDs and SQUID Systems – Vol I. edited by J Clarke and A Braginski. Weinheim: *WILEY-VCH*, 2004.

6. G Stroink, B Hailer and P Leeuwen. "Cardiomagnetism" in: Magnetism in Medicine, edited by W Andra, H Nowak. Weinheim: *WILEY-VCH*, 2006.

7. M Janawadkar, R Baskaran, R Saha, K Gireesan, R Nagendran, L Vaidhyanathan, J Jayapandian and T Radhakrishnan. SQUIDs: Highly sensitive magnetic sensors. *Curr Sci.* **77** (1999) 759–769.

8. C Foley, M Keene, H Brake and J Vrba. "SQUID system issues." in: The SQUID Handbook - Fundamentals and Technology of SQUIDs and SQUID Systems - Vol I. edited by J Clarke and A Braginski. Weinheim: WILEY-VCH, 2004.

9. M Janawadkar, T Radhakrishnan, K Gireesan, C Parasakthi, S Sengottuvel, R Patel, C Sundar and B Raj. SQUID-based measurement of biomagnetic fields. *Curr Sci.* **99** (2010) 36-45.

10. X Kong, S Zhang, Y Wang, J Zeng and X Xie. Multi-Channel magnetocardiography system based on low T_c SQUIDs in an unshielded environment. *Physics Procedia.* **36** (2012) 286 – 292.

11. K Kobayashi, M Yoshizawa and D Oyama. Development of SQUID magnetometer with direct-feedback noise cancellation for magnetocardiogram without Magnetically Shielded Room. *IEEE Trans Appl Supercond.* **27** (2017) 1601504 1-4.

12. P Swain, S Sengottuvel, R Patel, A Mani and K Gireesan. A feasibility study to measure magnetocardiography using First Order Gradiometer. *Biomed Sig Proces Cont.* **55** (2020) 1–9.

13. Y Lee, J Kim, K Yu, K Kim, H Kwon, I Kim and Y Park. 64-channel second-order planar gradiometer system for magnetocardiograms. *IEEE Trans Appl Supercond.* **17** (2007) 831-834.

14. J Clarke and A Braginski "Practical DC SQUIDs: Configuration and Performance" in The SQUID handbook – Fundamentals and Technology of SQUIDs and SQUID systems – Vol I. *WILEY-VCH, 2004*.

15. P Ornelas, A Bruno, C Barbosa, E Lima and P Ribeiro. A survey of calibration procedures for SQUID gradiometers. *Supercond Sci Technol*. **16** (2003) 427-431.

16. J Vrba and S Robinson. Signal processing in magnetoencephalography. *METHODS*. **25** (2001) 249-271.

17. P Ribeiro, S Williamson and L Kaufman. SQUID arrays for simultaneous magnetic measurements: calibration and source localization performance. *IEEE Trans Biomed. Eng*. **35** (7) 551-560.

18. S Sengottuvel, A Sharma, D Biswal, P Khan, P Swain, R Patel and K Gireesan. Feasibility study on measurement of magnetocardiography (MCG) using fluxgate magnetometer. *AIP Conf Proc.* **1942** 060018 (2018).

19. Z Xue-Min, R Yu-Feng, Y Hong-Wei, Z Shi-Ping, C Geng-Hua, Z Li-Hua and Y Qian-Sheng. A digital filtering scheme for SQUID based magnetocardiography. *Chinese Phys*. **15** (2006) 100-103.

20. L Zhao, J Feng, G Zhai and L Zhang. Wavelet transformation for magnetocardiography signal. *Acta Physics Sinica*. **54** (2005) 1943-1949.

21. K Kim, Y Lee, H Kwon, J Kim and J Bae. Independent component analysis for synthetic aperture magnetometry in magnetocardiography. *Comput Biol Med*. **36** (2006) 253-261.

22. H Lim, H Kwon, N Chung, Y Ko, J Kim, I Kim and Y Park. Usefulness of magnetocardiogram to detect unstable angina pectoris and non ST-elevation myocardial infarction. *Am J Cardiol*. **103** (2009) 448-454.

23. W Haberkorn, U Steinhoff, M Burghoff, O Kosch, A Morguet and H Koch. Pseudo-Current Density maps of electrophysiological heart, nerve or brain function and their physical basis. *Biomagn Res Technol*. **4** (2006) 1-18.

24. J Nenonen. Solving the inverse problem in magnetocardiography. *IEEE EMBS*. **13** (1994) 487-496.

Chapter 3

MEASUREMENT OF MCG INSIDE MAGNETICALLY SHIELDED ROOM

3.1 Introduction

The advantages of magnetocardiography (MCG) have been reviewed in the context of various clinical applications [1-6]. Unfortunately, the MCG set-ups currently in use all over the world differ considerably from each other as far as system parameters such as the number and type of SQUID sensors, sensor spacing, the type of pick-up coils, baseline distance, site of MCG measurement (heavily shielded room, moderately shielded room, lightly shielded room, unshielded site) etc. for reasons of cost, expediency and user specific requirements. Hence, unlike the standard 12-lead electrocardiogram (ECG) which is widely accepted as a routine investigation technique for the assessment of electrical activity of the heart with clinically validated interpretation of possible deviations observed, MCG is a relatively new technique which requires standardization of measurement protocols (sensor locations, type of sensor used, measurement SNR which depends on ambient magnetic noise and shielding factor of the MSR, signal sampling rate, data preprocessing methodology, data visualization tools etc.) in order to evolve a standardized procedure for a meaningful and clinically valid interpretation of the measured MCG signals, and for an easy visualization of the data that could be quickly and directly interpreted by a clinician using a standard and validated methodology.

However, even in the absence of a well-established and clinically validated way to interpret the measured magnetocardiogram, it is generally accepted that the use of magnetic field maps

(MFMs) constructed from the spatial distribution of cardiac magnetic field serves as a quintessential tool for interpreting the measured MCG data. For a healthy heart with normal electrical conduction pathway, modelling the cardiac activation wave front at each instant of time as a single equivalent current dipole (ECD) with well-defined magnitude and direction has been widely accepted to be valid and any deviation from a clear dipolar pattern in the measured MFM itself has been suggested to hint at an anomaly which needs further investigations in detail. Assuming the validity of this model, MFMs plotted at specific time instants on the cardiac cycle also aid in visualizing the underlying cardiac current distribution in a completely non-invasive manner [7]. Measured MFMs have been shown to exhibit a qualitative agreement with those expected on the basis of an ECD model, lending further credence to this model and enabling the computation of certain quantitative parameters characterizing the inferred ECD for further analysis. It is also possible to elucidate the temporal evolution of measured magnetic field patterns by sequential generation of MFMs at different time instants of the cardiac cycle in order to obtain a more intuitive visualization of the cardiac activity; indeed, such visualization tools may be important not only for a quick recognition of cardiac abnormalities, if any, but also for providing useful insights into the underlying cardiac electrophysiology.

In the present series of investigations, MCG measurements have been used to construct MFM of subjects with two specific cardiac disorders, viz., coronary artery disease (CAD) and right bundle branch block (RBBB), in order to quantitatively analyze the MFM parameters and develop an empirical understanding of how these functional abnormalities manifest in the measured MFM. In addition, MFM generated from MCG recorded on the posterior thoracic surface has also been examined to explore the possibility of obtaining complementary information on intra-atrial activation.

3.2 Materials and methods

3.2.1 CAD and RBBB

Coronary artery disease (CAD) or myocardial ischemia is the most common type of heart disease which occurs when the major blood vessels supplying blood, oxygen and nutrients etc. to the heart muscle become damaged [8]. The cholesterol containing deposits (plaques) are often blamed to be the root cause of CAD as their build up can narrow the arteries, decreasing blood flow to the heart. Eventually, the reduced blood flow may cause chest pain, shortness of breath or other CAD symptoms. A complete blockage of the coronary artery can lead to heart attack or myocardial infarction (MI). These ischemic signatures are usually manifested in the ST segment of the cardiac cycle in the conventional ECG test, with a relatively low sensitivity [2]. Therefore, in clinical practice, exercise ECG is performed as the first level noninvasive diagnosis of CAD. However, in many patients, other additional invasive and more expensive procedures such as Single Photon Emission Computed Tomography (SPECT), nuclear stress test, coronary angiography etc. may be needed [9-10]. Hence, a noninvasive procedure to diagnose ischemia at an early stage with a relatively high sensitivity is much sought after.

Right bundle branch block (RBBB) is a conduction anomaly that occurs due to the blockage of the right bundle branch of the electrical conduction system of the heart [11]. As a result of this block, the right ventricle is not directly activated by the usual route of conduction and passively gets activated through myocardial muscle (causing delayed conduction) after the depolarization of the left ventricle. The condition of RBBB is usually manifested as a broad QRS interval (more than 150 ms) in the ECG signal with widened S wave in lead I and V6 [12].

3.2.2 Study subjects

The present study group comprised three different categories of subjects.

Group I consisted of 12 patients diagnosed with CAD based on treadmill tests, following a standard protocol (ST segment in ECG showing a horizontal or down sloping depression of 1 mm or greater during peak exercise) and this diagnosis of CAD was subsequently corroborated by coronary angiogram. Group II consisted of 3 patients with RBBB with their ECG showing a broad QRS complex exceeding 150 ms in width, and standard patterns in V1-V6. Group III comprised of 20 healthy control subjects with no prior history of hypertension or heart disease in the family and a having a normal rest ECG. The characteristics of the study group are summarized in table 3.1.

TABLE-3.1

Clinical characteristics of the study population

	Group I (CAD)	*Group II (RBBB)*	*Group III (Healthy controls)*
Number of subjects	12	3	20
Male sex (%)	50	100	60
Age (years)	57 ± 7	50 ± 6	34 ± 8
Diabetes (%)	33	33	0
Hypertension (%)	25	33	0

3.2.3 MCG recording and data processing

MCG was recorded inside the magnetically shielded room (MSR) for all the patients (group I and group II) as well as normal healthy subjects (group III). For patients of group I and group II, MCG was measured on the anterior thoracic surface using thirty-seven channel and four channel MCG systems respectively. The MCG measurements for subjects of group III were performed over both anterior and posterior thoracic surfaces using the four channel MCG system. All the MCG measurements made with a four channel MCG system necessitated sequential scanning of the entire thoracic area of interest by appropriate repositioning of the subject relative to the sensor array at nine different positions, thereby recording MCG at a total of 36 locations ($9 \times 4 = 36$) on

the thoracic surface, since recording at each position yielded MCG data only at four sensor locations covering a relatively small thoracic area. Hence, sequential repositioning of the subject relative to the sensor array was essential to obtain the MCG data at 36 locations spread over the entire thoracic area of interest in these studies. At each location, MCG was recorded for a total duration of about 5 minutes for each subject in order to include sufficiently large number of nominally identical cardiac cycles in each recording.

The recorded MCG data was primarily processed using wavelet technique (dB 10 with 10-12 levels of decomposition) for removing baseline drifts and correcting the offset, if any [13]. The baseline corrected data of the 37 channel MCG system were then subjected to Fast ICA algorithm in order to eliminate the contribution of noise from the measured multichannel data [14]. Out of a total of twelve independent components, 6 or 7 independent components were typically identified to be associated with cardiac signals of interest and the rest were identified as associated with power line, vibration and other high frequency noise. Denoised MCG signal was reconstructed after eliminating the independent components associated with noise during the reconstruction of the signal. The time series data sets denoised using ICA were then subjected to trigger based averaging, where a large number of nominally identical cardiac cycles were epoched using the R wave peak as the fiducial reference point for the purpose of aligning, and the aligned cardiac cycles were averaged to suppress any residual uncorrelated noise with a view to generate a representative cardiac waveform pertaining to the particular location on the thoracic surface. The baseline corrected data involving only four channels (recorded using the four channel MCG system) could not be processed using the ICA technique and were directly signal averaged using the cardiac R peaks as the trigger points.

Since the electrical manifestations of CAD are usually observed during the repolarization phase of the ventricles in the ST-T duration (time interval between the end of S wave peak to the T

peak) of the cardiac cycle, this region of interest was divided into three equal segments [15]. MFMs were generated at each of these four instants of time by spatial interpolation of the denoised MCG data corresponding to the representative averaged cardiac waveform at each thoracic location, and joining the interpolated points exhibiting similar magnetic field values by smooth contour lines. For patients with RBBB, MFM was generated at the S peak time instant on the cardiac cycle [16] following an identical procedure. In order to study the instantaneous atrial excitation in normal subjects, the P wave interval (the time interval between P_{onset} + 10 ms and P_{offset} - 10 ms) of subjects from group III was divided into three equal segments and analysis was performed by generating MFMs at each of the four time instants [17].

3.2.4 MFM parameters

Two parameters have been inferred from the MFMs generated at different time instants of the cardiac cycle. The parameters are related to the overall appearance of Magnetic field map (dipolar and multi-polar shape of the MFM) and the maximum current angle (angle subtended by the deduced current dipole vector with a horizontal reference line traversed clockwise). It may be noted that, the maximum current angle (θ_c) plotted at the S peak time instant of the cardiac cycle is expected to be in the range of -96^0 to -45^0 for healthy subjects [18]. The expected range of the maximum current angle is -5^0 to 77^0, when plotted at the T peak time instant of healthy subjects [19].

3.3 Results

3.3.1 Evaluation of MCG parameter for study group I

Out of the 12 subjects with CAD, MFM generated at the ST-T interval of five subjects were found to be resembling an overall dipolar pattern, although orientation of the dipole appeared to be relatively different compared to that expected for healthy subject. The orientation of the current dipole at the T peak time instant was found to be $120^0 \pm 59^0$.

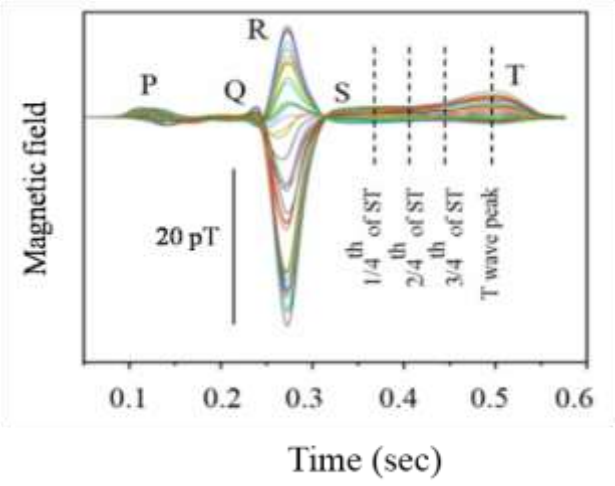

Figure 3.1 Butterfly plot for a subject with CAD. The ST-T time segment was equally divided into four intervals as shown in the figure, and MFMs were generated at each of these time instants.

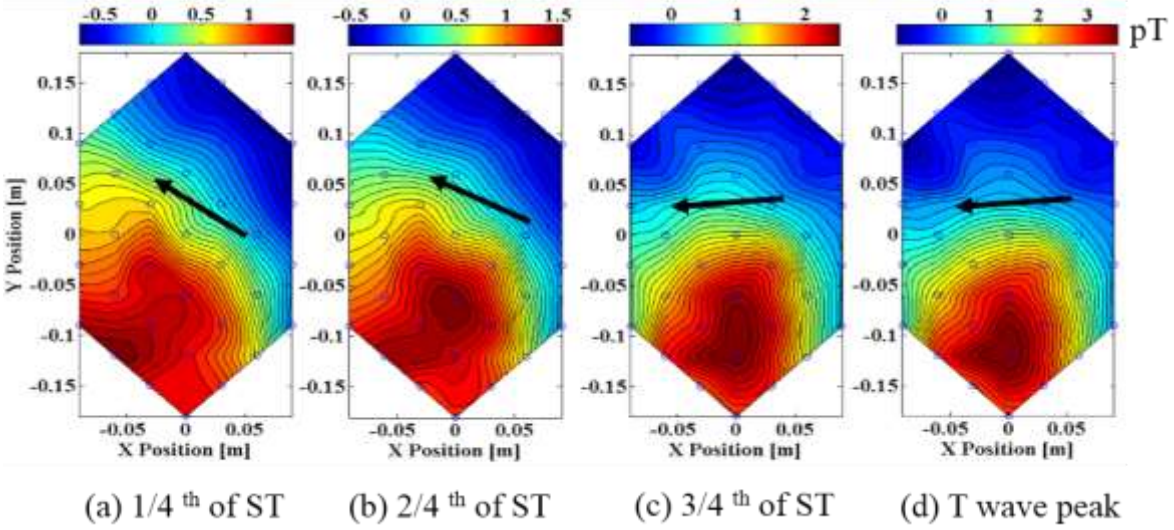

Figure 3.2 MFMs generated for a subject with CAD at (a) 1/4th of the time segment (b) 2/4th of the time segment (c) 3/4th of the time segment and (d) T wave peak instant. The black solid arrows indicate the direction of current dipole. The orientation of the dipole is observed to change as one approaches the T wave peak.

Figure 3.1 shows the superposition of the averaged cardiac traces collected from all the thirty-seven locations over the thorax (the butterfly plot) of a representative subject. The corresponding MFMs generated at different time instants on the ST-T interval of the cardiac cycle are shown in figure 3.2. For rest of the seven CAD patients, the MFM patterns were seen to be abnormal (broken or rotated or compressed) [19]. As an illustration, figure 3.3 shows the butterfly plot for

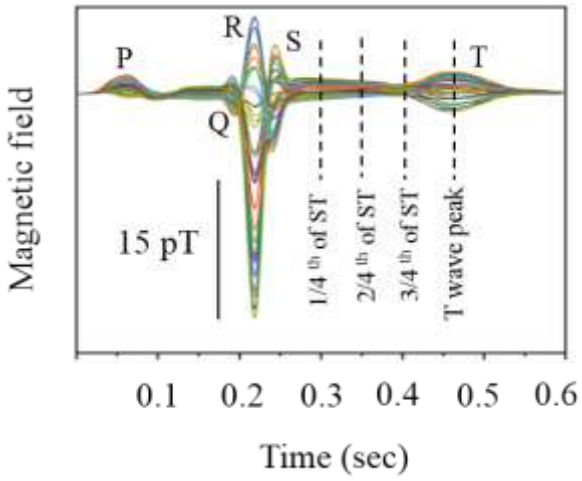

Figure 3.3 Butterfly plot for another representative subject with CAD. The ST-T time segment was equally divided into four intervals and MFMs were generated at each of these time instants.

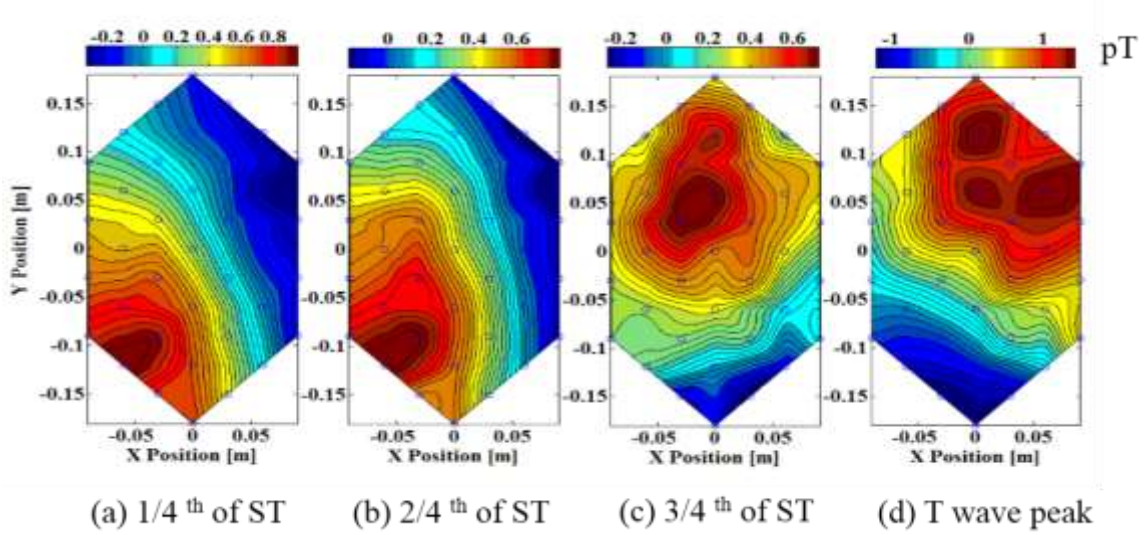

Figure 3.4 MFMs generated for a subject with CAD at (a) 1/4th of the time segment (b) 2/4th of the time segment (c) 3/4th of the time segment and (d) T wave peak instant. Complex MFM pattern, possibly resulting from activation of multiple dipoles or even multipoles, is seen at T peak instant.

a CAD patient from this category, whose MFMs generated at the ST-T instants (as shown in figure 3.4) were observed to be broken.

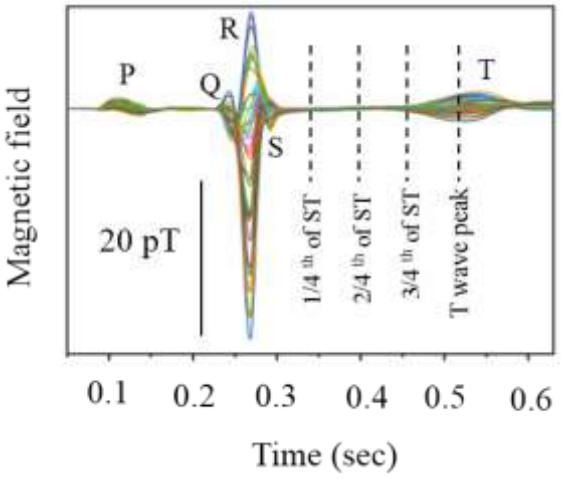

Figure 3.5 Butterfly plot for a normal subject. The ST-T time segment was equally divided into four intervals and MFMs were generated at each of these time instants.

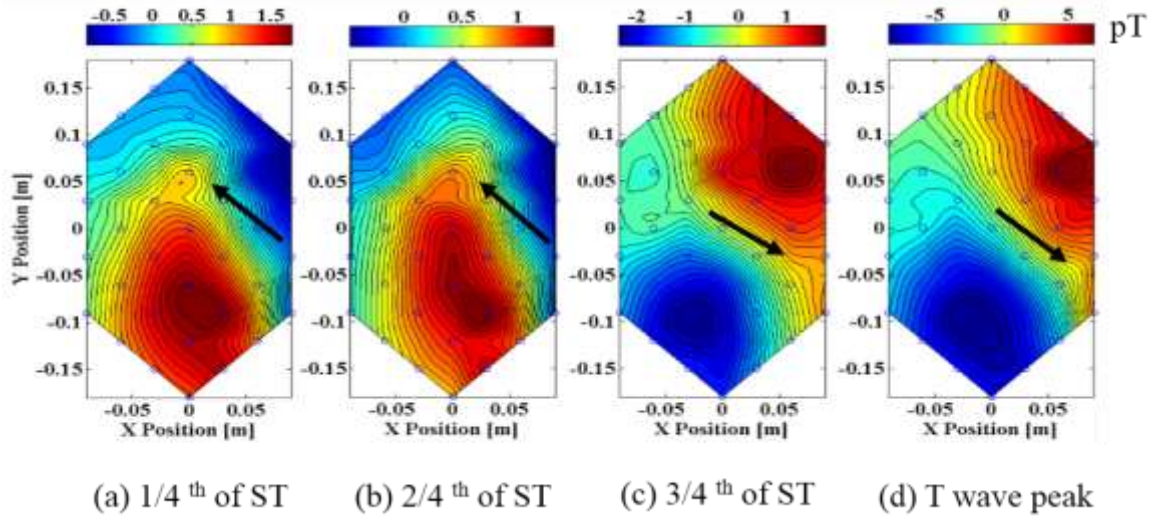

Figure 3.6 MFM generated for the normal healthy subject at (a) 1/4th of the time segment (b) 2/4th of the time segment (c) 3/4th of the time segment and (d) T wave peak instant. The MFMs are indicative of a typical dipolar pattern with a maximum current angle of 30^0 at the T peak time instant. The black solid arrows indicate the inferred direction of the current dipole.

For comparison, figure 3.5 shows the cardiac waveforms at all the channel locations plotted together as a butterfly plot for a normal subject, while the corresponding MFMs generated at the

ST-T interval is depicted in figure 3.6. In this case, the MFMs were observed to be clearly dipolar with a maximum current angle of 30^0 at the T peak time instant.

3.3.2 Evaluation of MCG parameter for study group II

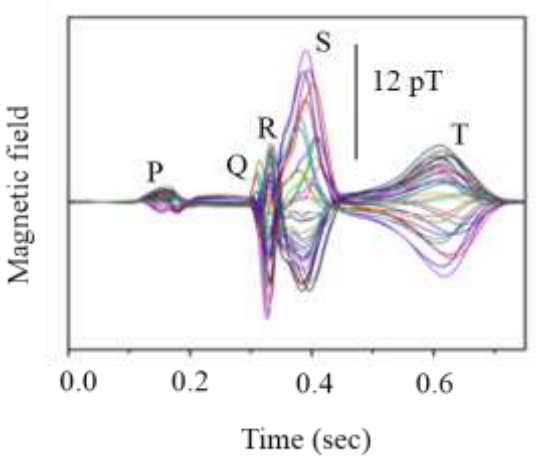

Figure 3.7 Butterfly plot for a subject with RBBB. The delay in the activation of the right ventricle is manifested as a wide QRS (> 150 ms) complex in the cardiac cycle.

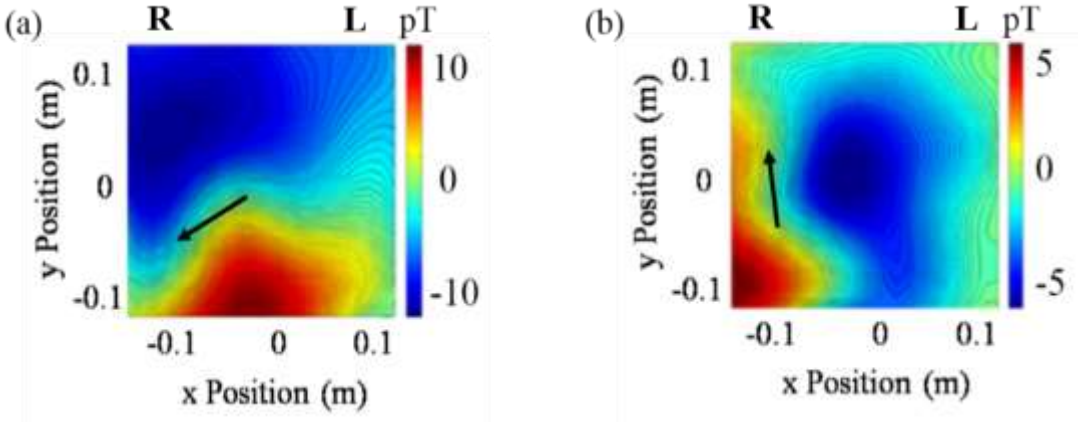

Figure 3.8 MFM generated at the S peak time instant of the cardiac cycle for the (a) subject with RBBB (b) normal subject. The black solid arrows indicate the direction of the inferred current dipole.

Figure 3.7 shows the representative cardiac waveforms at different locations on the chest plotted together as a butterfly plot for a subject with RBBB. As mentioned earlier, the duration of the QRS complex for this group is expected to be larger than the range for normal subjects,

and hence, the QRS complex may be seen to be relatively broad (exceeding 150 ms) for this subject as opposed to a narrow QRS seen for normal subjects (figure 3.5). Figure 3.8 (a) shows the MFM generated at the instant of time corresponding to S peak for the subject with RBBB shown along with those generated for a healthy subject in figure 3.8 (b). A significant deviation in the current dipole angle for the subject with RBBB as compared to a normal subject is discernible with the current dipole for the subject with RBBB oriented towards right as opposed to an upright orientation for the healthy subject. Quantitatively, current angle at the S wave peak was measured to be in the range of ($148^0 \pm 35^0$) for all three subjects in group II. It is to be noted that, the maximum current angle for the 20 healthy subjects (taken from group III) as inferred from their MFM plot at the S wave peak instant was found to be $-86^0 \pm 10^0$.

3.3.3 Evaluation of MCG parameter for study group III

Figure 3.9 illustrates the overlay plots of P waves measured sequentially using the 4 channel MCG system across 36 locations on both anterior and posterior surfaces of the thorax for a

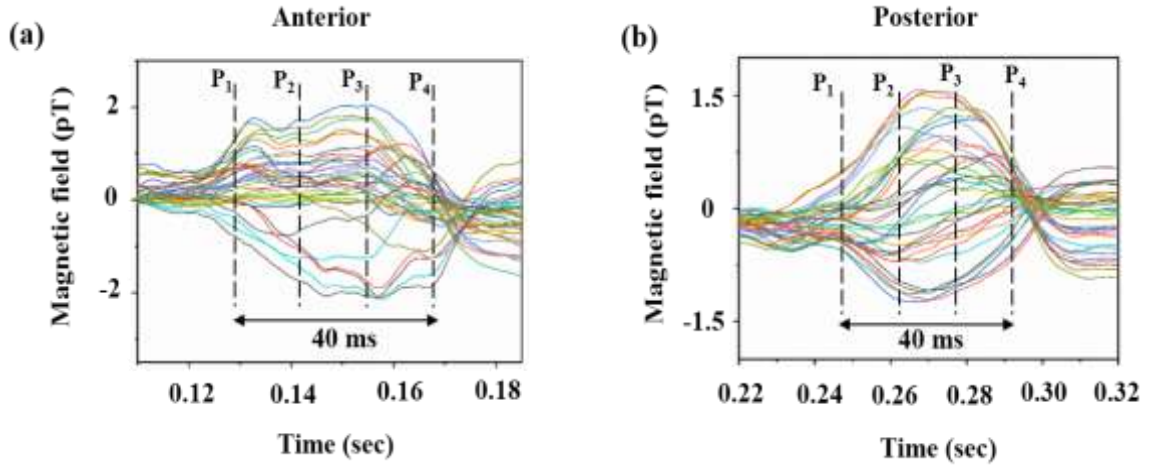

Figure 3.9 Averaged MCG traces featuring P waves of all 36 cardiac traces overlaid for (a) anterior side (b) posterior side.

normal subject. The dotted lines in figure 3.9 (a) and (b) represent the time instants at which the MFMs shown in figure 3.10 were generated.

The MFMs generated at different time instants on the P wave (including both early and late

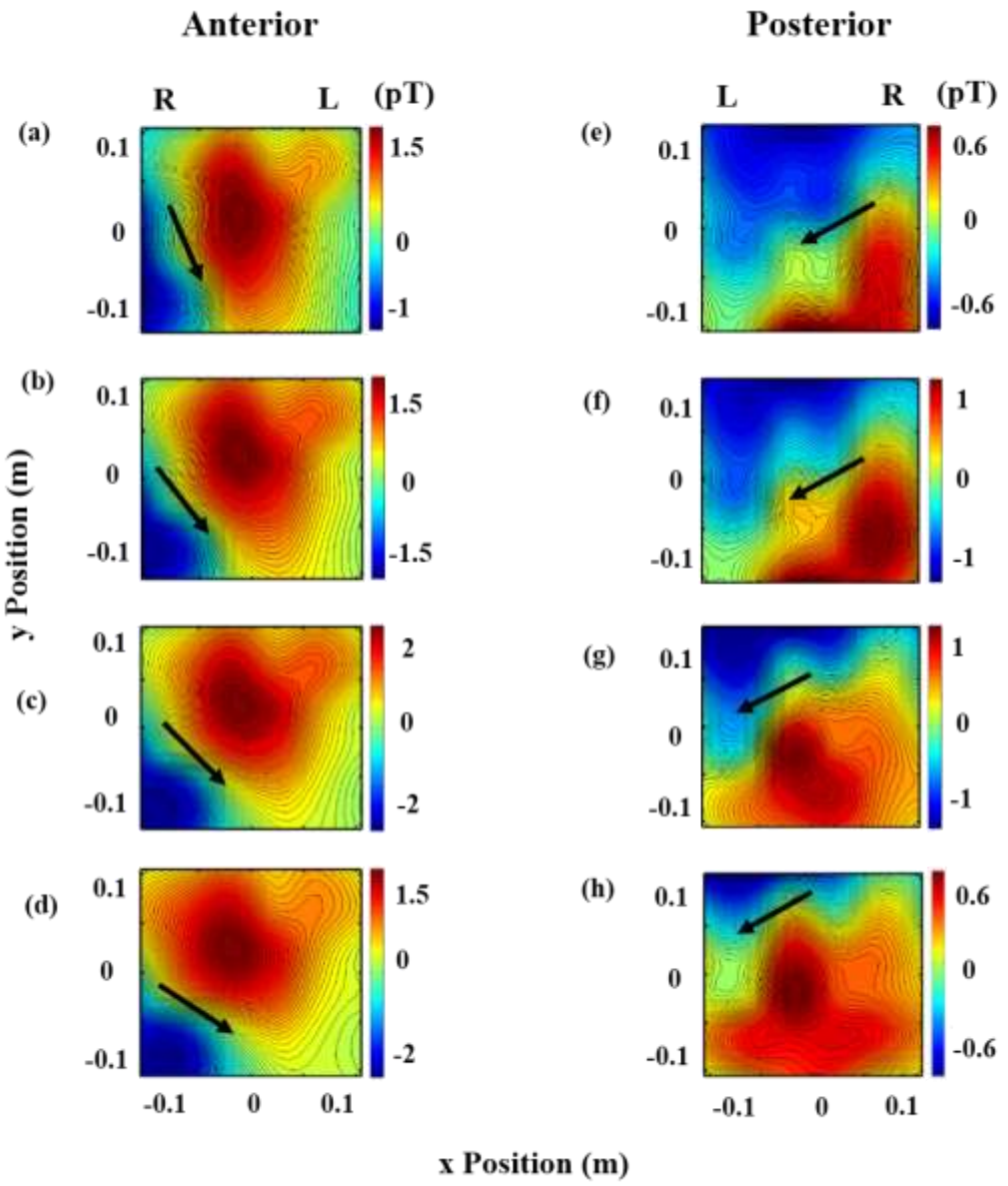

Figure 3.10 MFMs plotted at various time instants on the P wave of a normal subject for MCG measured on the (a) anterior thoracic surface (b) posterior thoracic surface. The black solid arrows indicate the direction of current dipole. The MFM patterns remain almost unchanged during atrial excitation for the anterior case. However, for the posterior case, the pattern of MFM was found to have changed slightly at the later stages of P wave compared to those corresponding to early stages; the points representing minimum and maximum magnetic field were found to have shifted slightly towards the left, displacing the position of the inferred current dipole towards the left side of the heart during this phase of the activation.

stages of P wave) for the anterior case showed a positive maximum in the left upper part of the map and a negative maximum in the right lower part with only a relatively minor change in pattern from the onset to offset of the P wave. Hence, the inferred current dipole associated

with this phase of activation was found to be located in the right part of the heart directed inferiorly and towards the left as shown in figure3.10. Similarly, the MFMs generated at the early time instants of the P wave (at P_1 and P_2 time instants) measured for the posterior case signified a current dipole located on the right part of the heart directed inferiorly and towards the left. However, during the late stages of the P wave (at P_3 and P_4 time instants), the posterior MFM was found to be slightly displaced from the earlier ones (those at P_1 and P_2 time instants) in such a way as to indicate that the current dipole during the later phase of the P wave was shifted further towards the left side of the heart. The direction of maximum current dipole inferred from both the anterior and posterior MCG data sets of the study group III was in the range of 17^0 to 85^0 degrees and 103^0 to 175^0 degrees respectively.

3.4 Discussion

Results presented in this chapter show that MFM of subjects with CAD deviated clearly from that observed for a healthy subject, especially when MFM is plotted during the repolarization phase of the ventricles. While the MFMs observed for a healthy subject were predominantly dipolar with characteristic changes in the orientation of the current dipole during repolarization of ventricles along the ST segment, MFMs observed for a subject with CAD were found to be complex and multipolar. Thus, MFM emerges as a visualization tool that has the potential to easily and clearly differentiate between a healthy subject and a subject with CAD, and thereby aid the clinician in routine diagnosis of CAD on the basis of MCG measurements.

Similarly, the MFM of subjects with RBBB at the instant of S wave peak deviated considerably from that observed for a healthy subject. While the current dipole inferred from the MFM for a healthy subject was found to be nearly upright at the S wave peak that for a subject with RBBB was found to be oriented towards the right inferior region. The abnormal appearance of the MFM at the S wave peak of RBBB patients indicated an anomalous electrical excitation in

the anteroseptal region of the heart. It is evident that conduction abnormalities like RBBB manifest as characteristic signatures in the MFM plotted at a specially selected point (or a set of points) along the cardiac waveform, thereby highlighting the possible potential of MFM to quickly and unambiguously recognize such abnormalities from the MCG measurements. The observed differences in MFM for a healthy subject and a subject with conduction abnormality illustrate the effectiveness of MFM in identification of the abnormality, consistent with the pathophysiology of their respective conditions.

The MFM constructed during P wave of the cardiac cycle using MCG data measured on both anterior and posterior thoracic surfaces of normal subjects indicated the presence of current dipole directed inferiorly and to the left. However, the positions of current dipole inferred using the anterior and posterior MFMs differed slightly, especially towards the end of the P wave. While the current dipole inferred from anterior MFM was found to be located towards right part of the heart and directed inferiorly towards the left, the current dipole inferred from the posterior MFM towards the end of the P wave was found to be further shifted to the left. The atrial excitation may be divided into right and left atrial activities; however, the anterior MFMs were predominantly indicative of the right atrial activity while the posterior MFMs appear to capture the signatures of activation front shifting from right to left atrium as the P wave progresses [20] as suggested by the displacement of the maximum and minimum field areas in the posterior MFMs towards the end of P wave. The reason for the ability of the posterior MFMs to capture the left atrial activities better may be attributed to the anatomical orientation of the left atrium towards the posterior surface [21].

In the present study, it was observed that the MFM patterns of subjects with different types of cardiac dysfunctions differed significantly from those of normal subjects. It was also possible to observe significant variations in the pattern of MFM for normal subjects when the MCG

measurement side was altered from anterior to posterior by changing the posture of the subject from supine to prone position. Owing to these variations, MFM appears to be a viable visualization tool capable of capturing the "signature" of the underlying cardiac electrophysiology.

3.5 Conclusion

In the absence of an equivalent of the standardized ECG lead system for the measurement and interpretation of MCG data, we have highlighted the use of Magnetic field maps (MFMs) to infer useful diagnostic information from the MCG data measured using different MCG systems in three different groups of subjects. Despite differences in the number of channels, sensor positions and geometrical configuration of sensors etc. in MCG systems used for the measurement, MCG data could be presented in the form of MFM in each case, enabling one to gain better insight into cardiac electrophysiology by a detailed analysis of the position and orientation of the current dipole inferred from the MFM. This graphical analysis allows one to pick up important features of the underlying cardiac electrophysiology, notwithstanding the differences in the measurement conditions (such as number of sensors, type of pick-up loop etc.), which otherwise tend to make comparison of results obtained using different MCG systems relatively difficult. The approach also enables one to interpret the measured MCG data better by offering new insights compared to what is possible from the recorded time series MCG data alone. The two basic parameters, viz., the overall appearance of the MFM pattern and the maximum current angle derived from the MFM were also shown to be useful in discriminating between healthy and abnormal activations of the heart. This technique provides a simple yet reliable way to noninvasively diagnose different types of cardiac disorders, and hence could be used as a valuable diagnostic procedure. Possibility of a quick display of the measured MCG data in the form of MFM at selected time instants of cardiac cycle makes the technique useful for mass screening of different

cardiac conditions in a cardiovascular OPD since, unlike ECG, there is no need to attach electrodes at the standard positions.

References

1. T Inaba, Y Nakazawa, K Yoshida, Y Kato, A Hattori, T Kimura, T Hoshi, T Ishizu, Y Seo, A Sato, Y Sekiguchi, A Nogami, S Watanabe, H Horigome, Y Kawakami and K Aonuma. Routine clinical heart examinations using SQUID magnetocardiography at University of Tsukuba hospital. *Supercond Sci Technol*. **30** (2017) 1-6.

2. B Hailer, I Chaikovsky, S Auth-Eisernitz, H Schafer, F Steinberg and D Gronemeyer. Magnetocardiography in coronary artery disease with a new system in an unshielded setting. *Clin Cardiol.* **26** (2003) 465-471.

3. R Fenici and D Brisinda. Magnetocardiography provides non-invasive three-dimensional electroanatomical imaging of cardiac electrophysiology. *Anatol J Cardiol.* **22** (2006) 23-27.

4. H Li, S Zhang, C Zhang and X Xie. SQUID-based MCG measurement using a full-tensor compensation technique in an urban hospital environment. *IEEE Trans Appl Supercond.* **26** (2016) 1601805 1-5.

5. Y Seki, A Kandori, Y Kumagai, M Ohnuma, A Ishiyama, T Ishii, Y Nakamura, H Horigome and T Chiba. Unshielded fetal magnetocardiography system using two-dimensional gradiometers. *Rev Sci Instrum.* **79** (2008) 036106 1-3.

6. F Shanehsazzadeh, N Kalantari, F Sarreshtedari and M Fardmanesh. Environmental noise cancellation for high-T_c SQUID-based magnetocardiography systems using a bistage active shield. *IEEE Trans Appl Supercond.* **27** (2017) 1602306 1-6.

7. H Koch and W Haberkorn. Magnetic field mapping of electrophysiological function. *Phil Trans R Soc Lond A.* **359** (2001) 1287-1298.

8. Coronary heart disease. National Heart, Lung and Blood Institute. http://www.nhlbi.nih.gov/health/health-topics/topics/cad. Accessed Apr 28, 2020.

9. G Beller and R Heede. SPECT imaging for detecting coronart artery disease and determining prognosis by noninvasive assessment of myocardial perfusion and myocardial viability. *J Cardiovasc Transl Res.* **4** (2011) 416-24.

10. S Kohsaka and A Makaryus. Coronary angiography using noninvasive imaging techniques of cardiac CT and MRI. *Curr Cardiol Rev.* **4** (2008) 323-330.

11. Chou's electrocardiography in clinical practice: Adult and Paediatric, 6e.

12. C Mueller, K Laule-Kilian, T Klima, T Breidthardt, W Hochholzer, A Perruchoud, M Christ. Right bundle branch block and long-term mortality in patients with acute congestive heart failure. *J Intern Med.* **260** (2006) 421-428.

13. L Zhao, J Feng, G Zhai and L Zhang. Wavelet transformation for magnetocardiography signal. *Acta Physics Sinica.* **54** (2005) 1943-1949.

14. S Comani, D Mantini, G Alleva, S Luzio and G Romani. Fetal magnetocardiographic mapping using independent component analysis. *Physiol Meas.* **25** (2004) 1459-72.

15. R Ramesh, S Sengottuvel, S Satheesh, P Swain, R Patel, A Pillai, K Gireesan and R Selvaraj. Magnetocardiography for identification of coronary ischemia in patients with chest pain and normal resting 12- lead electrocardiogram. *Ann Noninvasive Electrocardiol.* **25** (2020) 178-185.

16. R Verzola, O Baffa, R Wakai and P Sousa. Magnetocardiography in normal subjects and in patients with right bundle branch block. *Braz J Med Biol Res.* **28** (1995) 1327-31.

17. M Sato, Y Terada, T Mitsui, T Miyashita, A Kandori and K Tsukuda. Vizualization of atrial excitation by magnetocardiogram. *Int J Cardiovasc Imaging.* **18** (2002) 305-12.

18. B Leithauser, J Park, P Mill, Y Lam and F Jung. Magnetocardiography in patients with acute chest pain and bundle branch block, *Int J Cardiol.* **168** DOI: 10.1016/j.ijcard.2013.01.254.

19. H Lim, H Kwon, N Chung, Y Ko, J Kim, I Kim, Y Park. Usefulness of magnetocardiogram to detect unstable angina pectoris and non ST-elevation myocardial infarction, *Am J Cardiol.* **103** (2009) 448-454.

20. K Ogata, A Kandori, T Miyashita, K Tsukuda, S Nakatani, W Shimizu, H Kanzaki, K Miyatake, S Yamada, S Watanabe and I Yamaguchi. Noninvasive visualization of three-dimensional atrial electrical excitation using anterior and posterior magnetocardiogram. *Comput Cardiol.* **32** (2005) 527-530.

21. J Malmivou and R Plonsey. Bioelectromagnetism. Oxford University press, New York, ISBN: 9780195058239, 1995.

Chapter 4

MEASUREMENT OF MCG AT UNSHIELDED SITE

4.1 Introduction

Human cardiac magnetic signals are known to have a relatively higher amplitude compared to other biomagnetic signals such as those originating from the physiological activities of the human brain, intestines and other organs when measured non-invasively on the outer skin surface. This fact encourages one to try to explore the possibility of measuring the MCG signal either inside a partially shielded enclosure or even at a completely unshielded site, thereby avoiding the necessity of an expensive magnetically shielded room (MSR) for the MCG measurements. Further, since all the features in a cardiac signal are expected to repeat themselves in each cardiac cycle, there are possibilities of improving the Signal-to-Noise ratio of the recorded MCG signal using averaging and other suitable software-based denoising algorithms. Although the use of higher order gradiometers (especially the Second Order Gradiometers) is the conventional way of combating the excessively high noise encountered in any unshielded MCG measurement, they are reported to diminish the measurement sensitivity by attenuating the signal of interest (especially signals originating from deeper sources) [1-2].

In the present work, we have attempted to measure MCG at a totally unshielded site using First Order Gradiometers (FOGs). The goal was to try to achieve a clinically acceptable quality of MCG data in an unshielded configuration without significant loss of information related to the signal. We employed software-based signal denoising techniques to handle the excessively

high external electromagnetic noise. While the importance of signal denoising algorithms for measuring MCG in an unshielded environment has been discussed by various research groups [3-6], our investigations are particularly focused on examining the efficacy of ensemble empirical mode decomposition (EEMD) technique for this purpose [7]. The features of cardiac signal have been extracted from noisy MCG traces recorded at an unshielded site using a combination of the EEMD technique for signal denoising as well as the conventional approach of averaging a large number of cardiac cycles after aligning them with respect to time instants of the R wave peaks derived from the simultaneously measured single lead electrocardiogram signal. An improvement in Signal-to-Noise ratio (SNR) of about 18 dB could be achieved using a combination of the two methods. As part of this effort, the MCG signals derived from measurements carried out in an open unshielded environment were quantitatively compared with those measured inside the MSR for a few healthy subjects along with a subject with a known cardiac disorder (right bundle branch block, or RBBB). The results of the present study indicate that it is possible to obtain reasonably good quality MCG signals from measurements carried out at an unshielded site, and encourage further efforts directed at improvements in the technique so as to enable a possible reduction in cost of the MCG system, and thereby promote a more widespread practical use of the MCG technique in clinical environments.

4.2 Methods

4.2.1 Basic principles of EEMD

Ensemble empirical mode decomposition (EEMD) is a noise assisted data analysis method, which is an extension of the original Empirical Mode Decomposition (EMD) method [8]. Unlike the Fourier and wavelet-based signal decomposition techniques, which rely on the use of predefined set of basis functions, EMD method has a distinct advantage of deriving its basis functions, EMD method has a distinct advantage of deriving its basis functions, known as the

Intrinsic Mode Functions (IMFs), adaptively from the input data itself through a process known as sifting. EMD seeks to decompose the original signal and express it as a linear combination of IMFs, with each IMF representing an elementary oscillatory function with variable amplitude, which captures a particular time scale present in the original signal; this signal decomposition facilitates the recognition of signal and noise components by analysis of inherent time scales of each IMF, and thereby offers a useful method to denoise the measured original signal by suppressing the components attributed to noise during the signal reconstruction process. However, the EMD process is sometimes prone to mode mixing, especially, in the presence of intermittent signal or noise. Mode mixing refers to the occurrence of the same time scale in different IMFs or different time scales in a single IMF [7]. The objective of EMD to decompose the original signal into components corresponding to different time scales is not fulfilled when mode mixing occurs. The EEMD method helps in mitigating this challenge faced by the EMD and thereby improves the robustness of its performance in a wider variety of noisy situations (especially, when signal or noise are not present continuously, but only intermittently). In this section, we briefly describe both EMD and EEMD algorithms along with an account of the thresholding technique, which has been used to suppress noise from the original signal after it is decomposed into IMFs using EEMD.

4.2.1.1 EMD

As already mentioned, EMD decomposes a given time-series signal into a set of IMFs by repeated use of a specially designed sifting process [8] to successively identify components corresponding to progressively slower time scales. The first IMF corresponds to the fastest time scale present in the signal, while the last IMF corresponds to the slowest time scale present in the signal. A function qualifies to be designated as an IMF, if it satisfies the following two conditions [8]. (a) The number of extrema and the number of zero crossings of the function should either be the same or at most differ by one (b) The mean value of the upper and lower envelopes defined

by the local maxima and local minima of the function at any instant of time within the total span should be zero. These IMFs form a complete and nearly orthogonal basis for the original signal. The decomposed IMFs are then individually analyzed using the Hilbert spectral analysis/ Hilbert Huang Transform (HHT) which yields an energy-time-frequency spectrum, and enables calculation of the instantaneous frequency and amplitude of each IMF and thereby allows the identification of inherent localized features in the original signal [9].

For a given signal *x(t)*, the sifting process followed by the EMD algorithm to determine the corresponding IMFs is as follows:

(i) Locate all the local maxima and minima of the original signal *x(t)*. Join all the maxima using a cubic spline to form an upper envelope, and all the minima using a cubic spline to form a lower envelope.

(ii) Calculate the difference between the original signal *x(t)* and the mean of the upper and lower envelopes, $m_1(t)$.

Let $h1(t) = x(t) - m_1(t)$ (4.1)

(iii) Check whether the difference $h_1(t)$ satisfies the two criteria prescribed for an IMF. Otherwise, repeat the steps (i) and (ii) by replacing *x(t)* by $h_1(t)$. This procedure is successively repeated until a function satisfying the criteria prescribed for an IMF is reached. To find an IMF, it is usual to repeat the above procedure successively on the functions $h_1(t)$, $h_2(t)$, $h_3(t)$,……..until the following stoppage criterion is met. Defining a sum of the differences (SD) given as:

$$SD = \sum_{t=1}^{N} \frac{|h_{k-1}(t) - h_k(t)|^2}{{h_{k-1}}^2(t)} \quad , \qquad (4.2)$$

The sifting process is terminated when the SD is less than a pre-defined value.

The first IMF determined using the above iterative procedure and the stopping criterion is denoted by $c_1(t)$.

(iv) Once the first IMF $c_1(t)$ is obtained, calculate the residue $r_1(t)$ as:

$$r_1(t) = x(t) - c_1(t) \tag{4.3}$$

(v) Now, the residue $r_1(t)$ is taken up as the new signal to be decomposed and all the previous steps are repeated over $r_1(t)$ to obtain the subsequent IMFs $c_2(t)$, $c_3(t), \ldots . c_m(t)$ and the corresponding residues $r_2(t)$, $r_3(t) \ldots \ldots$, $r_m(t)$.

(vi) The process stops when the residue $r_m(t)$ is a monotonic function so that any further attempt to repeat the procedure on $r_m(t)$ turns out to be futile and no further IMF can be produced from $r_m(t)$.

Hence, the original signal $x(t)$ can be written as the sum of all constituent IMFs. Mathematically,

$$x(t) = \sum_{i=1}^{m-1} c_i(t) + r_m(t) \tag{4.4}$$

where $c_i(t)$ represents the i th order IMF and $r_m(t)$ represents the residue (or the last IMF). The time series analysis of the constituent IMFs indicates a progressive variation from fine to coarse scales with increase in the order of the IMF. EMD has been shown to perform as a dyadic filter for various kinds of noise present in the original data, including both white and fractional Gaussian noise [10, 11]. The method has also been used for signal denoising by ignoring the IMFs attributed to noise, and reconstructing the denoised signal by summing selected IMFs (partial sums of IMFs) pertaining to the signal of interest [12]. However, the EMD may sometimes fail in separating the different time scales present in the original signal into separate IMFs, and consequently, may result in mode mixing [7].

4.2.1.2 EEMD

EEMD method was proposed by Wu and Huang to solve the problem of mode mixing, which was sometimes encountered when the traditional EMD method was used on certain types of input signals, especially, those involving intermittent presence of either signal or noise [7]. In EEMD, a controlled amount of white noise *w(t)* is added to the original signal *x(t)* to obtain a noise contaminated signal $\widetilde{x_n}(t)$, which is then decomposed into IMFs following the usual EMD technique. The process is repeated for a reasonably large number (M) of times (trials) with different embodiments of white noise $w_n(t)$ at the n^{th} (n=1,2,3,….,M) trial. Subsequently, the corresponding IMFs from all the trials are ensemble averaged to get the true IMFs corresponding to the original signal *x(t).* Because of averaging over the M independent trials, the added noise gets reduced by a factor of $(\epsilon_0/\sqrt{M})$ in the final IMF, where ϵ_0 is the amplitude of the added noise and *M* is the total number of trials which are averaged. This reduction of added noise occurs as there is no correlation between the different realizations of the time series representing the noise $w_n(t)$ added in each of the *M* trials.

The basic steps followed during the EEMD algorithm are as follows.

(i) Add a finite amount of white noise time series $w_n(t)$ to the original signal *x(t)* in the n^{th} trial to obtain a new signal $\widetilde{x_n}(t)$. The amplitude of the added noise can be a fraction (typically 0.1-0.4) of the standard deviation of the original signal *x(t).*

$$\widetilde{x_n}(t) = x(t) + \epsilon_0 w_n(t) \tag{4.5}$$

Here $\widetilde{x_n}(t)$ is the new signal after the addition of white noise $w_n(t)$ to *x(t)* at the *n* th trial, *x(t)* is the original signal, $w_n(t)$ is the white noise added to *x(t)* at the *n* th trial and ϵ_0 is the scaling factor that controls the overall amplitude of white noise $w_n(t)$ which is added to the original data.

(ii) Use EMD to decompose the new signal $\widetilde{x_n}(t)$ into its constituent IMFs for each of the *M* trials (n = 1, 2, 3,……, M).

(iii) Average the corresponding IMFs obtained from different trials to get the final IMFs.

4.2.1.3 Thresholding

As mentioned earlier, conventionally, both EMD and EEMD methods reconstruct the denoised signal by using a partial sum of selected IMFs for the reconstruction of denoised signal [12, 13]. Usually, the first order IMF (high frequency component) is expected to be a noise only IMF and the rest of the IMFs may contain noise or signal depending on the outcome of a statistical test (based on the empirical model [13]) [12, 13]. During signal reconstruction, the IMFs having energy content similar to the first order IMF (noise only case) are discarded and all other IMFs are added together. However, practically, in the partial sum of IMFs, there may be a possibility of excluding some high energy high frequency content of the signal of interest and including some low energy high frequency oscillations representing noise into the signal of interest. In order to overcome this problem, a thresholding approach has been proposed to be used over the IMFs for selective retention of the signal components alone [14]. Based on a prior knowledge of the typical time duration and occurrence of each signal component, thresholding is applied over selected portions on the IMFs. Here, the samples of an IMF having their energy below a particular set value (threshold) can be assigned to noise and are made zero, whereas the samples which lie above the threshold are assigned to signal components and are retained [14]. Finally, all the denoised IMFs are added together to reconstruct the denoised version of the signal.

4.2.2 Experimental set-up

Before attempting to measure MCG in an unshielded environment, a three-axis flux gate sensor (Bartington Instruments, Oxfordshire, United Kingdom) was used to conduct a site survey of

ambient magnetic noise at potential measurement sites to identify a suitable location with relatively low level of ambient magnetic noise in the frequency range of interest. The measurement bandwidth of the fluxgate electronics was fixed as 0-200 Hz. The background ambient magnetic noise measured at different sites was digitized at a sampling rate of 2 kHz and the measured data was stored in a work station in the time domain. The corresponding power spectral density (PSD) as a function of frequency was also computed and stored in the frequency domain. Among the potential sites available for attempting unshielded MCG measurements, the site which exhibited the lowest ambient magnetic noise was selected to measure MCG in the unshielded environment using superconducting First Order Gradiometers coupled to low-T_c DC SQUIDs as sensors.

The four channel MCG system was equipped with four low-T_c DC SQUID sensors, where each sensor was inductively coupled to an on-chip integrated pick-up coil connected in series via superconducting contacts to a First Order Gradiometer type pick up coil of 15mm diameter and 50mm baseline wound using superconducting niobium wire. The system was used to measure MCG at the selected unshielded site by locating the cryostat at the selected site. The average noise floor measured for all the four SQUID sensors was about 12 $fT_{rms}/\sqrt{Hz}$ when the sensors were operated inside the MSR. At the site chosen for unshielded MCG measurement, the average noise floor measured for the SQUID sensors was about 3 $pT_{rms}/\sqrt{Hz}$ with noise peaks ranging from 1-3.5 $nT/\sqrt{Hz}$ at the line frequency and its harmonics. MCG measurements were carried out for a total of nine subjects at 36 locations on the anterior thoracic surface by a sequential repositioning of the subject relative to the sensor array at nine different positions during the MCG scan. Out of the nine subjects, eight were healthy and one patient was diagnosed with right bundle branch block (RBBB) based on prior ECG measurement. For each subject, ECG in lead I configuration was simultaneously recorded along with the unshielded MCG. This helped in deriving the time information on the occurrence of R wave peak in each cardiac cycle. The R

wave peak of ECG served as a fiducial reference for aligning and averaging the noisy cardiac cycles measured by the four channel MCG system at the unshielded site. The cardiac features were extracted during post processing of unshielded MCG signals using the standard trigger locked averaging procedure to suppress the uncorrelated noise [15]. After the completion of unshielded MCG measurements, the subjects were taken inside the MSR to perform regular MCG measurements by transferring the four channel MCG measurement system inside the MSR. All the measurement settings and the signal processing schemes were kept identical for both shielded and unshielded measurements.

4.2.3 MCG signal processing

4.2.3.1 MCG signal denoising

The raw as recorded MCG traces were low pass filtered with a cut off at 200 Hz using a second order butterworth filter to eliminate the high frequency noise components. The filtered data was then baseline corrected to remove slow drifts from the baseline of MCG [16]. Next, the MCG time series was subjected to trigger locked averaging by aligning the measured cardiac cycles with respect to the R-peak time instants derived from a simultaneously recorded single lead ECG. The exact time instants of occurrence of the R wave peaks in single lead ECG waveform were automatically identified using a suitable algorithm, and were then used to epoch the MCG time series measured at the unshielded site, and align a large number of measured cardiac cycles with respect to the time instants of R wave peaks [16]. Subsequently, the aligned MCG epochs were averaged to suppress uncorrelated noise and obtain one representative trace corresponding to each measurement location. The averaged MCG traces were treated with EEMD for further denoising. The selection of IMFs in EEMD has been traditionally executed via Hilbert spectral analysis. The IMFs which could be ascribed to noise components were totally eliminated, while the IMFs which contained some signal as well as noisy features were denoised using the

thresholding approach. In the present work, the number of ensemble averages for EEMD was fixed as 100.

4.2.3.2 Evaluation of MCG parameters

The denoised MCG signals have been assessed quantitatively using the following parameters.

(a) Signal-to-Noise ratio

Signal-to-Noise ratio (SNR) was calculated from the denoised MCG trace in each case using the following equation:

$$SNR = 20\ log_{10} \frac{B_S}{B_N} \tag{4.6}$$

Where B_S (signal) represents the peak-to-peak amplitude of the R wave of MCG and B_N (noise) represents the peak-to-peak amplitude of the signal observed at a time instant 0.2 s before the onset of the P wave where no signal of cardiac origin is expected to be present (and any signal observed at this instant of time is fully dominated by the contribution of the external sources of noise during the MCG recording) [17]. SNR was calculated for both shielded and unshielded MCG data for a comparative evaluation.

(b) MFM parameters

The spatial distribution of cardiac magnetic field at each instant of time was derived by interpolating the denoised MCG data measured at thirty-six different locations on the thorax, Magnetic field map (MFM) was generated at selected instants of time in the cardiac cycle by drawing smooth contour lines to join the spatial points on the anterior thoracic surface corresponding to the same value of cardiac magnetic field. Three standard parameters, viz., maximum current angle (θ_c), field map angle (θ_m) and maximum to minimum field ratio, were calculated from the generated MFMs at the T peak time instant for normal subjects and S peak

time instant for the subjects with RBBB, and the values of these parameters were compared with those derived from the corresponding sets of shielded MCG measurements for all subjects.

(c) Pearson correlation coefficient

Pearson's correlation coefficient (r) was computed to measure the level of correlation which exists between the denoised MCG traces measured in shielded and unshielded environments.

4.3 Results

The results have been summarized in three different sub-sections describing the process of selection of a suitable unshielded site for MCG measurements, recording of MCG signal at the selected unshielded site, augmentation of SNR using EEMD technique, and comparison of the denoised unshielded MCG traces with their shielded counterparts.

4.3.1 Measurement of MCG at an unshielded site

Table 4.1: Magnetic noise measurement using a fluxgate sensor

Site no.	B_x *(nT)*	B_y *(nT)*	B_z *(nT)*
1	27	12	80
2	50	20	80
3	40	60	120

The peak-to-peak ambient magnetic noise measured by the fluxgate sensor at three different locations along all the three mutually orthogonal directions are listed in table 1. As observed

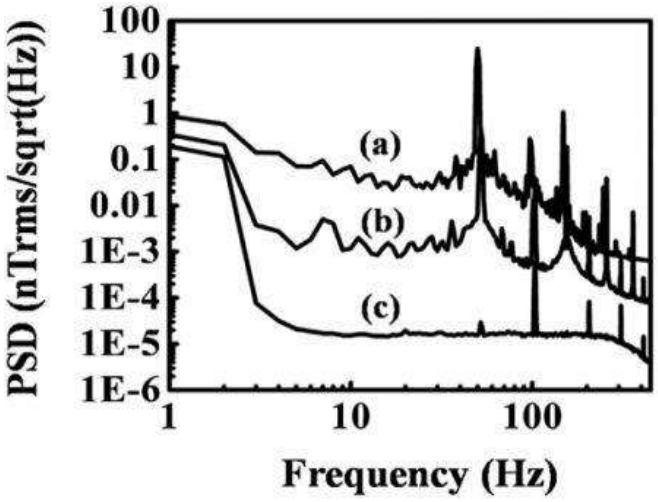

Figure 4.1 Power spectral density (PSD) of noise at the site selected for unshielded MCG measurements as recorded using (a) the flux gate sensor (b) superconducting gradiometer coupled to a low T_c DC SQUID sensor. For comparison, noise measured using the superconducting gradiometer coupled to a low T_c DC SQUID sensor inside the magnetically shielded room is also shown in (c).

from the table, site-1 shows the least ambient magnetic noise along all the three directions. Figure 4.1 shows the power spectral density of the background ambient magnetic noise measured at site 1 by fluxgate magnetometer and one of the four SQUID based First Order Gradiometers. In both the cases, the PSD spectra were seen to be dominated by line frequency (50 Hz) and its harmonics.

The fluxgate sensor shows a prominent 50 Hz peak of the order of 70 $nT_{rms}/\sqrt{Hz}$ with slightly lower amplitudes for its harmonics occurring at 100 Hz and 150 Hz making it impossible to use a fluxgate sensor to directly measure MCG at the unshielded site since the excessive magnetic noise is expected to completely mask the immensely weak MCG signal. However, spectral density of noise recorded by a first order superconducting gradiometer coupled to a low-T_c DC SQUID at the selected unshielded site indicates a reduction of about two orders of magnitude in both the overall noise as well as the noise at line frequency and its harmonics as compared to the noise recorded by the fluxgate magnetometer. This may be ascribed to the effect of the gradiometer in reducing the contributions of distant sources of magnetic noise.

White noise of the order of 1 $pT_{rms}/\sqrt{Hz}$ at frequencies of 10-40 Hz recorded by the SQUID gradiometer at the selected unshielded site outside MSR is indicative of its possible suitability for measuring MCG, since the R wave peak amplitude in MCG is expected to be about 50 to 100 pT. The spectral density of noise measured by the same SQUID sensor, when it is located inside the MSR, is also shown in figure 4.1 for comparison. The SQUID inside MSR showed the lowest white noise of the order of 12 $fT_{rms}/\sqrt{Hz}$; this hugely low magnitude of white noise

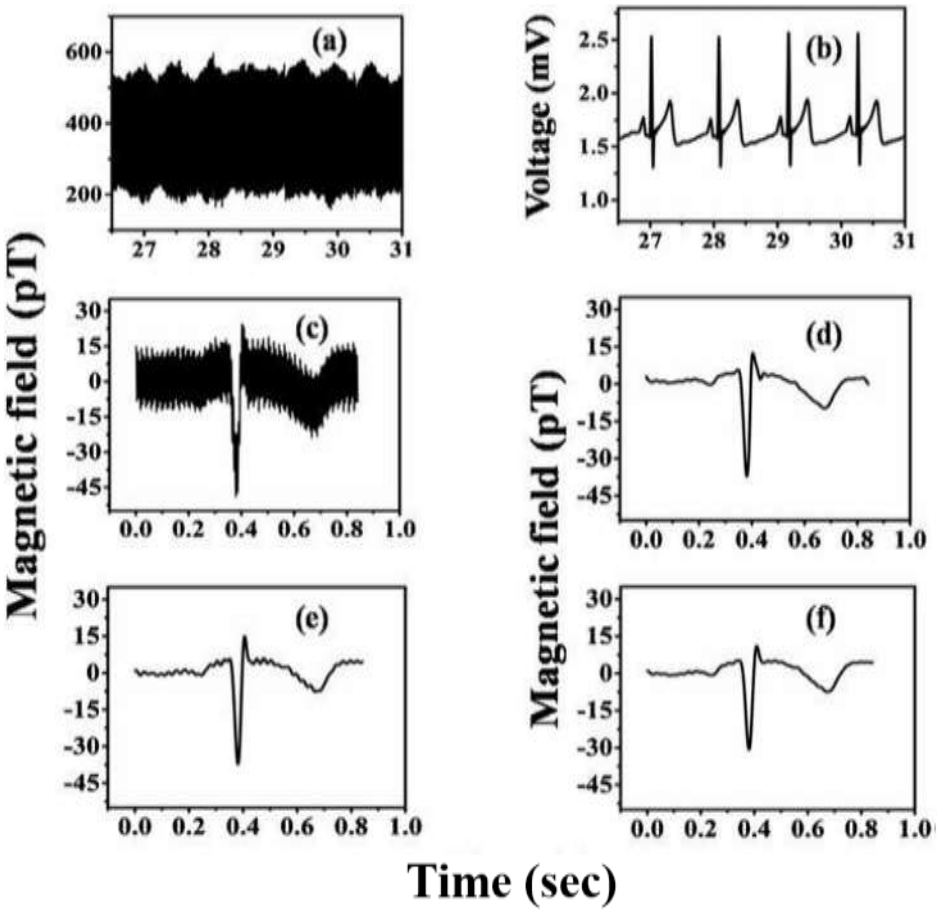

Figure 4.2 (a) A portion of the time segment of the noisy raw MCG signal measured at the unshielded site with no clear indication of cardiac features visible in the raw data; (b) Single lead ECG recorded simultaneously with MCG to be used as reference signal for identification of R-peak time instants required for trigger locked averaging of unshielded MCG shown in (a); (c) MCG signal derived by performing trigger locked averaging of the raw MCG signal shown in (a); (d) MCG signal obtained by performing EEMD based denoising of signal shown in (c); (e) 45 Hz low pass filter applied to trigger locked averaged MCG signal shown in (c); (f) Filtered data shown in (e) subjected to 20 point smoothening.

in the magnetically shielded environment makes it possible to measure MCG signals inside MSR with a very high SNR.

Figure 4.2 (a) shows a time segment of the raw as recorded MCG signal measured at the selected unshielded site using first order superconducting gradiometer coupled to a low T_c DC SQUID sensor. Figure 4.2 (b) shows the single lead ECG which was recorded simultaneously with unshielded MCG. Using R wave time instants derived from ECG shown in figure 4.2 (b), a large number of nominally identical cardiac cycles were aligned and averaged to suppress uncorrelated noise. Following this procedure, about 200 MCG cardiac cycles have been subjected to trigger locked averaging to obtain a representative cardiac waveform for each measurement location on the thorax as shown in figure 4.2 (c). Figure 4.2 (d) shows the output obtained when this averaged signal is subjected to EEMD based denoising to obtain reconstructed MCG signal with significantly reduced noise. To show the efficacy of EEMD method over other denoising techniques such as filtering, the averaged data shown in figure 4.2 (c) has also been subjected to low pass filtering with a cut-off at 45 Hz and the corresponding output is shown in figure 4.2 (e). As some of the noise components were present still after filtering, the filtered signal was further smoothened with a moving window average of 20 sampling points. As seen in figure 4.2 (f), while smoothening reduced the noise, it also reduced the signal amplitude.

Figure 4.3 shows the steps followed in a typical EEMD based denoising of MCG trace. Figure 4.3 (a) illustrates the decomposition of the averaged MCG trace into a set of six IMFs. The corresponding Hilbert-Huang transform (HHT) spectrum of each of the IMFs is shown in figure 4.3 (b), displaying the dynamics of the instantaneous frequencies of the highly non-stationary cardiac features and noise components present in every IMF. The cardiac features which are prominent in many IMFs (say 2, 3, 4 and 5) appear as higher energy components at the time of

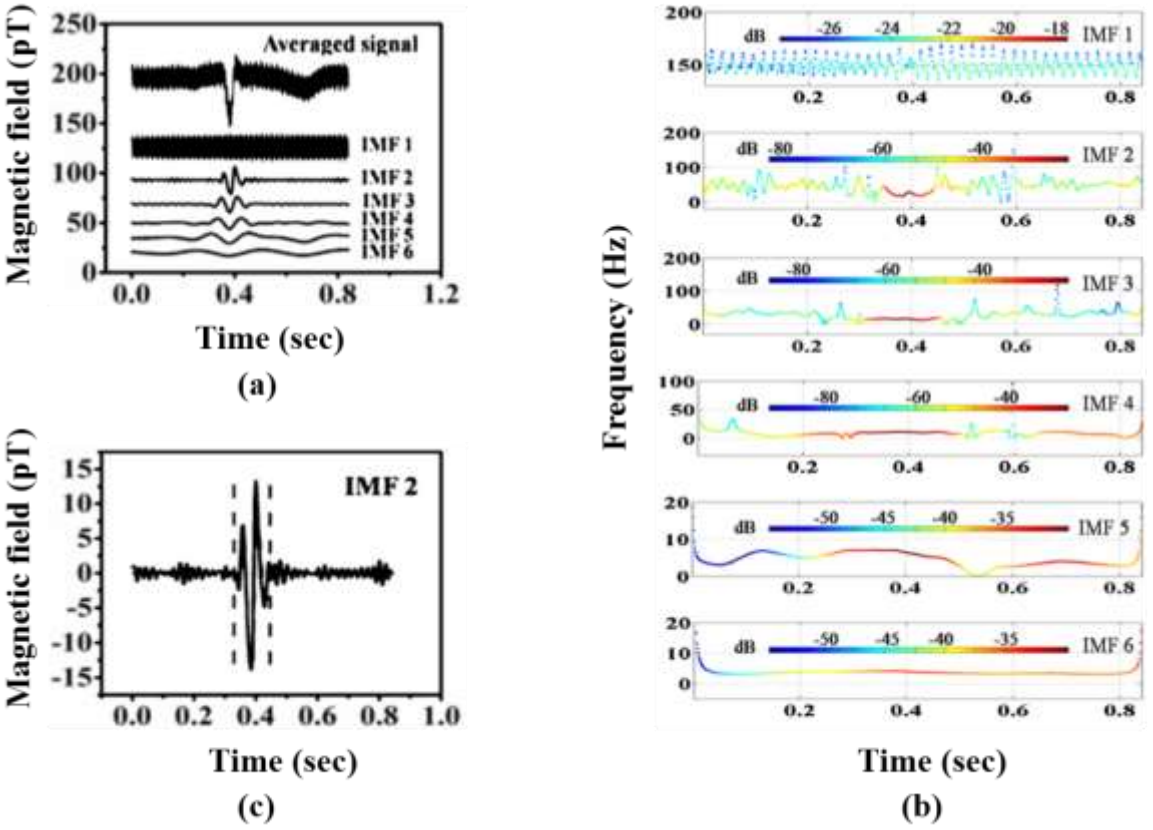

Figure 4.3 (a) Averaged MCG signal (top trace) and its decomposition into six IMFs (1–6) using EEMD technique (b) HHT spectrum of each IMF exhibiting the dynamics of instantaneous frequency along with the energy (c) interval thresholding for IMF 2 which contains some features of cardiac signal as well as some noisy wiggles.

their occurrences (QRS time regime) in their respective HHT spectrum. In particular, the high frequency components of the MCG signal are contained in the IMFs 2, 3 and 4, while low frequency components namely P and T waves are contained in IMF 6. It is evident that IMF 1 captures only line frequency components as corroborated by its HHT spectrum exhibiting frequencies around the third harmonic of line frequency (~ 150 Hz) and thus could be totally removed. The rest of the IMFs are subjected to interval thresholding. Figure 4.3 (c) illustrates interval thresholding performed on IMF 2, in which the chosen interval encompassing QRS duration is preserved and low amplitude high frequency oscillations adjacent to it are thresholded to zero.

Figure 4.4 illustrates a comparison of the denoised MCG traces measured in unshielded environment against those measured inside the MSR for a subject at two representative locations on the chest. Both figure 4.4 (a) and (b) show the consistency of the features of the cardiac cycle

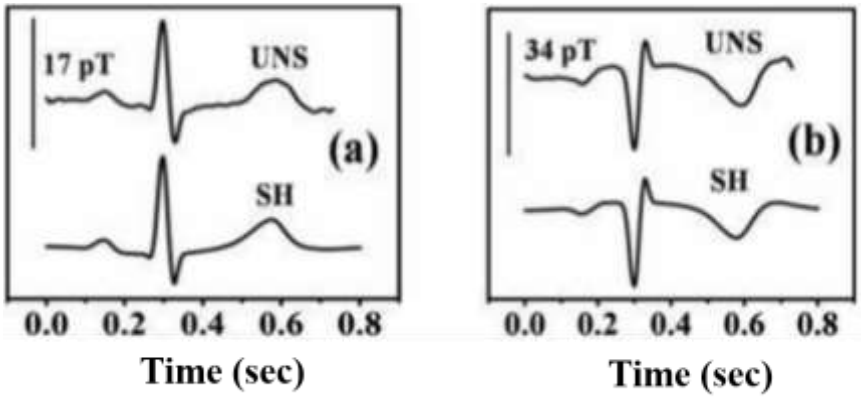

Figure 4.4 Comparison of the unshielded MCG (UNS) traces de-noised using EEMD method with those measured inside MSR (SH) for two representative measurement locations (a and b) on the thorax.

as observed across the two measurements.

4.3.2 Signal-to-Noise Ratio (SNR)

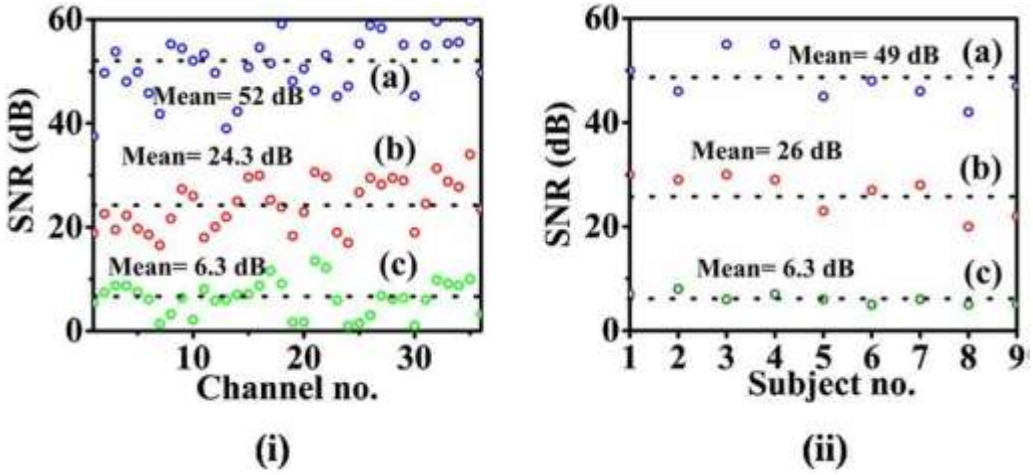

Figure 4.5 SNR of shielded-MCG, unshielded-MCG with and without EEMD are shown as (a), (b), (c) respectively (i) across measurement locations (ii) across subjects for a particular measurement location.

The improvement in SNR of the unshielded MCG as a result of EEMD based denoising is quantitatively assessed across the measurement locations and subjects as shown in figure 4.5. Figure 4.5 (i) depicts SNR calculated on MCG traces at different locations on the thorax measured at the unshielded site for a subject with and without EEMD based denoising and its comparison with SNR obtained in MCG measurements carried out inside the MSR. The horizontal dotted lines in the figure indicate the mean value of the SNR in each of the three cases. It is clear from the figure that the mean SNR of ~ 6 dB for the unshielded MCG could be improved to ~ 24 dB when the EEMD based denoising technique was used for signal denoising, indicating that it is possible to achieve an improvement of ~ 18 dB using EEMD technique. Similar analysis performed at one particular measurement location for all the subjects affirms the consistency of this improvement in SNR provided by EEMD as shown in figure 4.5 (ii).

4.3.3 MFM parameters

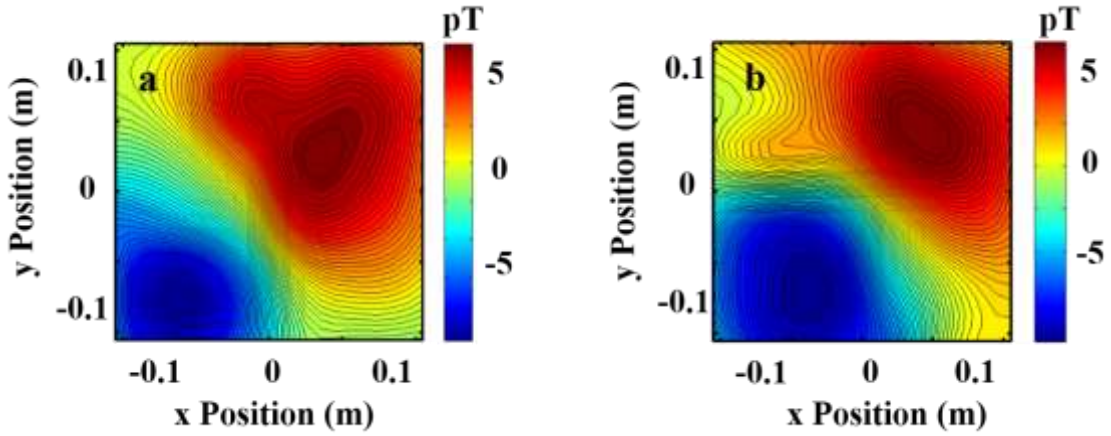

Figure 4.6 MFMs generated at the T wave peak time instant of the cardiac cycle from MCG (a) measured inside MSR (b) measured in an unshielded environment outside MSR for a healthy subject.

Figure 4.6 shows the MFM generated at a time instant corresponding to the T peak during the ventricular repolarization in the cardiac cycle for a healthy subject derived from the MCG measurements carried out both inside and outside the MSR. The three quantitate ve parameters,

viz., field map angle, maximum current angle and the maximum to minimum field ratio, calculated at the T peak time instant of the cardiac cycle for measurements inside the MSR were found to be $-50^0 \pm 3.5^0$, $40^0 \pm 3.5^0$ and 0.7 ± 0.1 respectively. The corresponding values of these parameters for the measurements carried out at the unshielded site outside the MSR were found to be $-49.5^0 \pm 5^0$, $40.5^0 \pm 5^0$ and 0.7 ± 0.1 respectively. It may be noted that MFM parameters inferred from measurements at unshielded site are in reasonable agreement with those inferred from measurements inside the Magnetically shielded roomand any small deviations in the values of these parameters may be attributed to minor errors in reproducing the exact positions of the subjects relative to the sensor array when the two sets of sequential measurements were carried out successively. Nevertheless, the differences in MFM parameters are within acceptable limits, highlighting the potential of unshielded MCG in correctly capturing the clinically significant information, when EEMD is used to denoise the MCG data measured at the unshielded site.

The maximum current angle has been calculated from the MFM constructed at the S wave peak time instant for the subjects diagnosed with RBBB. The values of maximum current angle were found to be 148^0 and 144^0 for the MCG measurements carried out in shielded and unshielded environments respectively. It may also be noted that the maximum current angles inferred from the MFM constructed at the S wave peak time instant in the cardiac cycle for a typical normal subject were found to be -86.2^0 and -91.7^0 for the measurements carried out in the shielded and unshielded environments respectively.

4.3.4 Pearson correlation coefficient

By taking MCG measurements carried out inside the Magnetically shielded roomas a reference bench mark for assessing the possible reliability of the MCG measurements at the unshielded site, correlation coefficient was calculated for unshielded MCG traces at all the thirty-six locations on the thorax with the corresponding traces measured inside the MSR on position-

by-position basis as illustrated in figure 4.7. It may be noted that the values of the correlation coefficient are found to be significantly higher when unshielded MCG data is denoised using EEMD. Higher correlation existing between the unshielded MCG (denoised using EEMD) and shielded MCG traces indicates that the quality of the unshielded MCG signal, after it is improved by using EEMD to denoise the data, is relatively close to that provided by measurements carried out inside the MSR. The correlation was statistically significant with $p < 0.01$.

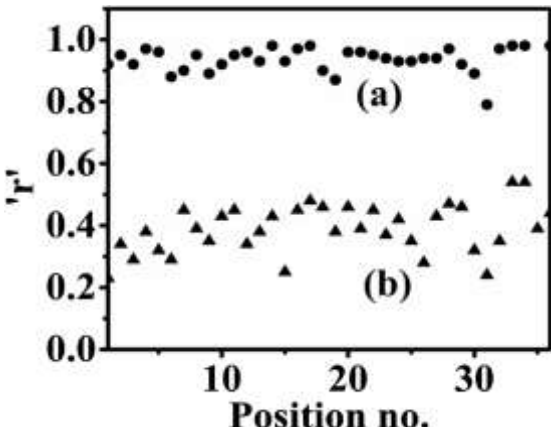

Figure 4.7 Correlation coefficient between unshielded MCG and shielded MCG traces across the 36 measurement locations (a) with EEMD based denoising and (b) without EEMD based denoising.

4.4 Discussion

The use of a First Order Gradiometer coupled to a low T_c DC SQUID sensor for unshielded MCG measurements is not much discussed in the literature. It is known that, the SNR achieved in measuring unshielded MCG using SOG is generally higher than that achieved using FOG [18]. This has also been reported in a simulation study based on the analysis of first and second order gradients of magnetic fields for unshielded environments by Rau and Baltag [19]. The simulation involved computation of the SNR achievable using FOG and SOG for varying distance ratios (2-10) of the signal and noise sources. The SNR provided by the Second Order Gradiometer (SOG) was found to be at least 3-10 dB higher than that provided by the FOG. However, the results

obtained in the present work indicate that by using FOG for measurement of MCG along with EEMD for denoising, it is possible to obtain an enhancement in the SNR of about 18 dB. This enhancement in SNR using EEMD, therefore, makes the signal measured with FOG comparable in quality to that measured using SOG, but without the possible signal loss accompanying the use of second or higher order gradiometers. As the distance of the source from the sensor increases, the value of the magnetic field gradient at the sensor location decreases. It is well known that this decrease is more for the second order gradient than for the first order gradient. Hence for relatively deeper sources, use of FOG is advantageous compared to SOG if some higher level of noise expected to be present at the output of FOG could be eliminated using other means (such as software-based noise reduction algorithms), and hence, use of FOG might pave way for characterizing such deeper sources in a better way compared to what is possible using SOG. A combination of first and Second Order Gradiometers for detecting weak signals from fetal heart (where the sources are located at greater depths from the sensor plane) in unshielded environments has been shown to give acceptable performance [20]. Indeed, such requirements are not uncommon even in the context of adult MCG, for example, in measuring MCG from the posterior side of the thorax (where the sensor to source distance is expected to be larger) [21].

Secondly, we have demonstrated the efficacy of EEMD based denoising technique in delivering good quality MCG data in an unshielded environment with reasonable values of SNR. Our investigations show that the proposed technique not only improves the quality of the cardiac features by enhancing the SNR, but also yields results that are very close to those measured inside the MSR. This validates the use of FOG along with EEMD based denoising procedure in extracting MCG data in an unshielded environment. It may be noted that the use of EEMD based denoising has not been much discussed in the literature in the context of MCG measurements in an unshielded environment. Use of signal denoising schemes like adaptive filtering has also been used with some success to extract the MCG signal when measurements are performed in

unshielded environments [22]. However, use of a single reference channel to denoise MCG from all the measurement locations would rely on the validity of some specific assumptions regarding noise and signal components, which may be difficult to justify in some contexts. EEMD is well known for its suitability to handle nonlinear admixtures of signals and noise [7].

Use of digital filters has also been explored for noise suppression [23]; however, this necessitates prior knowledge on the frequency range of either signal or noise components in order to selectively admit or remove them for the purpose of signal denoising. However, the present approach of EEMD incorporated with interval thresholding utilizes both types of information in an effective way by eliminating purely noisy IMFs while preserving the signal components by thresholding whenever an overlap occurs. Cardiac signals are highly non-stationary and the signal components themselves are spread over a wide range of frequencies (as is evident in their HHT spectrum). Hence, an optimal selection of filters which are universally suitable for a wide range of subjects, measurement channels and situations to denoise MCG signals without introducing any significant distortion in the signal of interest is difficult to achieve in practice [23]. Further, in the presence of multiple sources of artifacts contaminating the measured unshielded MCG data (besides the line frequency) as in the present case, implementation of just a band pass filter/ notch filter over the whole time series will be impractical and inadequate to eliminate all of them. Hence, EEMD with thresholding successfully manages this problem as evident from our results (Figure 4.2). The close agreement with MCG measured inside MSR indicates that it may be possible to reliably measure MCG in unshielded environment if EEMD based denoising procedure is used to suppress the noise. For the subject with RBBB, the maximum current angle is characterized by positive values at the S peak time instant of the cardiac cycle as opposed to the expected negative values observed for healthy subjects [24]. It is clear that the angles calculated from the MFM generated from unshielded MCG data are in reasonable agreement with those calculated using MCG data measured inside the MSR,

reaffirming the suitability of the unshielded MCG in providing clinically significant diagnostic information. The consistency of the diagnostic information provided by the maximum current angle derived from MFM corresponding to unshielded MCG data for the subject with cardiac dysfunction provides reasonable confidence that unshielded MCG could be used as a stand-alone modality (without requiring shielded MCG for further corroboration). It is hoped that this would promote a more wide-spread use of the MCG technique in practical environments inside a clinical setup in a hospital setting by obviating the necessity of an expensive Magnetically Shielded Room.

One of the limitations of the present study is the difficulty in keeping the SQUID sensors locked during their operation over the entire duration of time required for carrying out the unshielded MCG measurements. This is in view of the modest slew rate of the system used to track the MCG signals in unshielded environments, which resulted in loss of data recorded during time segments where the system unlocked. This problem could be partially alleviated by providing magnetic shielding around a part of the cryostat and by using flux locked loop (FLL) electronics with much higher slew rate.

4.5 Conclusion

A feasibility study has been conducted to explore the possibility of measuring MCG in a totally unshielded environment using First Order Gradiometer. The present work involved addressing a wide spectrum of issues and pre-requisites for establishing an unshielded MCG setup, such as site survey for identification of a suitable site, demonstration of MCG measurement in unshielded environment, enhancing the SNR using a software-based approach, comparative assessment of the MCG signals measured at the unshielded site with the MCG measurements inside MSR, deriving diagnostically important parameters from MFMs in subjects with cardiac dysfunctions etc. These results based on the use of FOG for detection of MCG signals at an

unshielded site provide the necessary confidence in establishing a low-cost MCG measurement setup in an unshielded clinical environment, especially for applications involving the detection of deeper sources, which are more difficult to detect using second or higher order gradiometers.

References

1. R Fagaly. Superconducting quantum interference device instruments and applications. *Rev Sci Instrum*. **77** (2006) 101101 1-45.

2. H Koch. SQUID magnetocardiography: status and perspectives. *IEEE Trans Appl Supercond.* **11** (2001) 49-59.

3. Y Liao, C He and Q Guo. Denoising of magnetocardiography based on improved variational mode decomposition and interval thresholding method. *Symmetery.* **10** (2018) 1-14.

4. M Bick, K Sternickel, G Panaitov, A Effern, Y Zhang and H Krause. SQUID gradiometry for magnetocardiography using different noise cancellation techniques. *IEEE Trans Appl Supercond.* **11** (2001) 673-676.

5. B Arvinti, A Isar, R Stolz and M Costache. Removal of repetitive magnetic interferences upon unshielded magnetocardiograms. *Rom Rep Phys.* **72** (2020) 1-11.

6. D Paolo. Numerical methods for improved signal to noise ratios in spatio-temporal biomedical data in dissertation, 2010, urn: nbn: de: gbv: ilm1-2010000179.

7. Z Wu and N Huang. Ensemble empirical mode decomposition method: a noise assisted data analysis method. *Adv Adapt Data Anal.* **1** (2009) 1-41.

8. N Huang, Z Shen, S Long, M Wu, H Shih, Q Zheng, n Yen, C Tung and H Liu. The empirical mode decomposition and the Hilbert spectrum for nonlinear and non-stationary time series analysis. *Proc R Soc Lond A: Math Phys Eng Sci.* **454** (1998) 903-995.

9. N Huang and Z Wu. A review on Hilbert-Huang transform: Method and its applications to geophysical studies. (RG 2006) 46: doi: 10.1029/2007RG000228.

10. P Flandrin, G Rilling, and P Goncalves. Empirical mode decomposition as a filter bank. *IEEE sig Process Lett.* **11** (2004) 112-114.

11. Z Wu and N Huang. A study of the characteristics of white noise using the empirical mode decomposition method. *Proc R Soc Lond A.* **460** (2004) 1597-1611.

12. P Flandrin, P Goncalves and G Rilling. “EMD equivalent filter bank, from interpretation to applications” In Hilbert-Huang Transform: Introduction and Applications, edited by N Huang and S Shen. Singapore: World Scientific. vol.5, 2005, pp 57-74.

13. Z Zhidong, J Liu and S Wang. Denoising ECG signal based on empirical ensemble mode decomposition. *Proc. SPIE*. 8285 (ICGIP 2011) doi: 10.1117/ 12.913515.

14. D Kwon, M Vannucci, J Song, J Jeong and R Pfeiffer. A novel wavelet based thresholding method for the pre-processing of mass spectrometry data that accounts for heterogeneous noise. *Proteomics.* **8** (2008) 3019-3029.

15. K Kim, Y Lee, H Kwon, J Kim, I Kim and Y Park. Averaging algorithm based on data statistics in magnetocardiography. *Neurol Clin Neurophysiol.* **42** (2004) 1-4.

16. S Sengottuvel, C Parasakthi, N Mariyappa, Rajesh Patel, K Gireesan, M Janawadkar, T S Radhakrishnan and M Thoddi. Enhancing the reliability in the noninvasive measurement of the his bundle magnetic field using a novel signal averaging methodology. *Ann Noninvasive Elecrocardiol.* **17** (2012) 186-94.

17. L Hua, S Zhang, Y Qiu, Y Zhang, C Zhang, X Kong and X Xie. Baseline optimization of SQUID gradiometer for magnetocardiography. *Chin Phys B.* **24** (2015) 028501.

18. J Clarke and A I Braginski, The SQUID handbook, vol II, WILEY-VCH, 2006, ISBN 9783527609956, pp 321.

19. M Rau and O Baltag. Analysis of magnetic gradient signal in unshielded electromagnetic environment. *Environ Eng Manage J.* **12** (2013) 1187-1192.

20. Y Seki, A Kandori, Y Kumagai, M Ohnuma, A Ishiyama, T Ishii, Y Nakamura, H Horigome and T Chiba. Demonstration of unshielded fetal magnetocardiography system using two dimensional gradiometers. *IEEE Trans Appl Supercond.* **19** (2009) 857-860.

21. K Ogata, A Kandori, T Miyashita, K Tsukuda, S Nakatani, W Shimizu, H Kanzaki, K Miyatake, S Yamada, S Watanabe and I Yamaguchi. Visualization three-dimensional

cardiac electrical excitation using standard heart model and anterior and posterior magnetocardiogram. *Int J Cardiovasc Imaging.* **22** (2006) 581-593.

22. V Tripolini. Magnetocardiography in unshielded environment based on optical magnetometry and adaptive noise cancellation in Ph D dissertation, Edith Cowan University, Joondalup WA, Australia, 2013.

23. S Comani, D Mantini, G Alleva, S Luzio and G Romani. Optimal filter design for shielded and unshielded ambient noise reduction in fetal magnetocardiography. *Phys Med Biol.* **50** (2005) 5509-5521.

24. D Brisinda and R Fenici. Magnetocardiography study of patients with right and left bundle branch blocks. *Int Congr Ser*. **1300** (2007) 451-454.

Chapter 5

SOURCE LOCALIZATION IN MCG

5.1 Introduction

Quantitative measurement of the spatial magnetic field distribution produced by human electrophysiological activity, in principle, has the potential to facilitate non-invasive localization of the underlying biological sources within the organ of interest using inverse problem techniques. Non-invasive localization and detailed characterization of the sources responsible for the measured magnetic field distribution is important not only for basic research relating to physiological functions of the organ of interest, but also for recognizing possible abnormalities with a view to devise suitable management strategies based on the knowledge of the identified sources and their locations within the organ of interest. Techniques based on electric potential measurements on the body surface (such as ECG) have been in routine use for the assessment of cardiac disorders. However, their ability to localize the underlying sources responsible for the measured electric potential distribution on the thoracic surface is considerably hampered by the fact that the electric potential distribution measured on the body surface is tremendously affected by the electrical conductivity profile of the intervening body tissues (some of which, like bones, are electrically insulating, and severely affect the propagation of electrical signals from the site of origin to the outer skin surface). Hence such electric potential measurements on the skin surface present a distorted picture of the underlying sources. Since the measured magnetic fields are not much affected by the electrical conductivity of the intervening tissues (which are mostly weakly diamagnetic and do not distort the external magnetic field distribution) [1], there is hope that analysis of MCG data may enable a more accurate solution to the inverse problem and

succeed in localizing the underlying sources more reliably compared to what is possible with ECG. It is also well known that MCG signal is sensitive to the primary currents originating directly from cellular activation, while ECG signal depends on the secondary volume currents flowing in the surrounding tissues acting as a passive electrical conductor while responding to the effects of time varying electric and magnetic fields produced by primary cellular activation; indeed, in special models such as horizontally layered conductor model, spherically symmetric conductor model etc., the contribution of volume currents to the external magnetic field vanishes exactly. Sensitivity of MCG signal to actual primary currents makes the MCG technique ideally suited for non-invasive localization of sources responsible for cardiac arrhythmias such as ventricular tachycardia, premature ectopic beats, supraventricular arrhythmias etc. as also for pre- and post-surgical mapping of cardiac activities, especially when a catheter intervention is required [1].

Solution of the inverse problem is often non-unique i.e. a large number of source configurations can yield similar magnetic field distributions to within the inherent measurement errors [2]. However, there are several approaches to overcome this ambiguity in choosing the correct solution corresponding to the actual source. For example, one or more anatomical and physiological constraints can be imposed on the source configuration and the source which meets all such realistically imposed constraints could be chosen to be the actual cardiac source responsible for the measured magnetic field distribution at a given instant of time [2].

The inverse problem in MCG is often posed as an optimization problem. The technique primarily assumes that a specific current source model characterized by certain source parameters (location, orientation, strength etc.) is responsible for producing the actual spatial distribution of magnetic fields measured across the sensor locations, and attempts to minimize the sum of squares of differences between the theoretically calculated magnetic field values at the sensor

locations based on the assumed model of the source, and the actual experimentally observed magnetic field values at the same locations (the minimized function is usually known as the cost function) in order to estimate the optimal values of the source parameters. The details of the model chosen for the source may depend on the problem under investigation; however, for simplicity, the source model usually chosen is either an equivalent current dipole (ECD) model, or multiple current dipole model, or a single magnetic dipole model etc. which can be characterized by a small number of source parameters (location, orientation, strength), although more extended current distributions with realistic volume conductor geometries of the organ of interest have also been sometimes used for this purpose. Many nonlinear optimization algorithms such as Levenberg-Marquardt (LM) [3], Nelder-Mead (NM) [4], genetic algorithm (GA) [5], simulated annealing etc. [6] have been used for solving the MCG source localization problems. It is known that, when the global search methods such as GA or simulated annealing methods are used, the solution obtained is usually an approximate one, corresponding to the optimal values of the source parameters for which a suitably chosen cost function attains its global minimum [7]. On the other hand, local search methods such as NM and LM often guarantee convergence to a local minimum of the chosen cost function in the neighborhood of an initial guess for the values of source parameters, which has to be provided to the search algorithm at the start of the iterative process [6]. Sometimes, these preliminary estimates are just randomly initiated, for example, using a set of pseudorandom numbers [3] for the initial values of source parameters, and it is possible to repeat the process with a large number of different sets of pseudorandom numbers in an attempt to scan the landscape of the cost function with the objective of reaching a global minimum, if possible. A major drawback of this approach is that the exact number of iterations required for the search process is not known apriori and for data sets containing noise, the search operation for the possible source position needs to be carried out over the whole scanning area (due to the existence of a large number of local minima of the cost function over

the large volume of the region which has to be potentially scanned), thereby considerably increasing the computational complexity. In order to circumvent these difficulties in estimating the initial guess values of source parameters in the presence of noise, derivative-free optimization methods have been recommended. The present work employs one of such derivative-free local search method namely, the Nelder-Mead method, to solve the magnetocardiographic inverse problem. In particular, as opposed to the conventional use of pseudo-random numbers for initializing the search, the present work suggests that taking the initial guess values of the source parameters derived from the pseudo-current density (PCD) map and iteratively refining the solution using the Nelder-Mead method appears to work well in practice.

The spatial distribution of magnetic fields measured across the sensor locations are widely used in MCG studies to empirically visualize the current source by generating Magnetic field maps (MFM) and pseudo-current density (PCD) maps. It is well known that, as compared to MFMs, PCD maps offer more quantitative information on the cardiac source in elucidating the position of maximum gradient vector on the sensor plane. Nevertheless, the exact position of cardiac sources with respect to *x*, *y* and *z* co-ordinates is essential to draw meaningful conclusions in clinically relevant problems. The present work utilizes the *x* and *y* coordinates of a point over the maximum gradient vector on the PCD maps as initial estimates of the source position for the Nelder-Mead method. The efficacy of this idea in estimating the cardiac source has been extensively tested on two different simulated test data-sets, namely, one computer generated data-set with magnetic field calculated using the forward problem with source parameters known apriori, and an experimentally measured data-set generated by measuring the magnetic field produced by a small test coil fed with synthetic cardiac signal from a waveform generator. The test data-sets have been analyzed under different Signal-to-Noise ratios (SNR) by admixing controlled amount of noise with the data. After extensive testing on the test data-sets, the method

has been applied for localizing cardiac sources from actual MCG measurements carried out on a few healthy subjects as well as subjects with different cardiac dysfunctions.

5.2 Methods

5.2.1 Nelder-Mead simplex method

This is a method for finding the minimum value of a function by generating simplexes, and examining the values of the function at the vertices of the simplex. A simplex is a structure in n dimensional space formed by (n+1) number of points that do not lie on the same hyper-plane. The values of the function are calculated at each of the vertices of the simplex and then compared with each other. The vertex which has the largest functional value is rejected and replaced with a new point chosen suitably relative to the centroid of the simplex using a set of operations. The search is usually performed with the help of four operators known as reflection, expansion, contraction and shrinking which are performed on the vertices of the previously generated simplex to obtain a new simplex for the next iteration. A sequence of simplexes is generated in this way and the search continues till the size of the simplex is eventually reduced to a sufficiently small region in the neighborhood of the correct solution. Finally, the coordinates of the point corresponding to the minimum value of the function are found. A detailed description of this method may be found elsewhere [8].

5.2.2 Modelling the source

In the present study, the cardiac source at any given instant of time has been modelled as a single equivalent current dipole (ECD) having an unknown location, orientation and strength, which comprise the source parameters, whose optimal values are required to be determined by minimizing the cost function. This particular model is simple, yet provides a reasonably accurate description for many problems in MCG [4]. The model assumes that only a single localized

current source is active at any given time instant of the cardiac cycle. Six-parameters consisting of three coordinates describing the position of the ECD and three components of dipole moment of the ECD along three mutually orthogonal directions are used to characterize the cardiac source in this model. As a simplification, the thorax can be assumed to be a horizontally layered conductor with layers parallel to the *X*-*Y* plane; in this model, *z*-component of the dipole moment does not contribute to the magnetic field component measured along the *z*-direction and hence may be disregarded for the analysis of the present data [3].

The *z*-component of the magnetic field produced at any point (x, y, z) by a current dipole positioned at (x′, y′, z′) with dipole moment (Q_x, Q_y, Q_z) is given by [9],

$$B_z(x, y, z) = \frac{\mu_0}{4\pi} \frac{[Qx\,(y-y') - Qy\,(x-x')]}{[(x-x')^2 + (y-y')^2 + (z-z')^2]^{3/2}} \tag{5.1}$$

where μ_0 is the permeability of free space.

As the present experiments were performed using first order axial gradiometers, the experimentally observed data was fitted to the gradient of equation (5.1) along the *z* direction, which is given by,

$$\frac{\partial B}{\partial z'}(x_j, y_j, z_j) = \frac{3\mu_0}{4\pi} \frac{(-z')[Qx\,(y_j-y') - Qy\,(x_j-x')]}{[(x_j-x')^2 + (y_j-y')^2 + (z_j-z')^2]^{5/2}} \tag{5.2}$$

where (x_j, y_j, z_j) represent the position of j^{th} channel. For convenience, the thorax and the sensor plane were assumed to be parallel to the *X*-*Y* plane with the origin of the coordinate system fixed at the point of intersection between the central axis of the cryostat and the sensor plane. In view of this choice of the coordinate system, all the sensors are located on the *X*-*Y* plane so that z_j =0.

5.2.3 Setup for the study

5.2.3.1 Problem statement

The purpose of the proposed NM simplex method for source localization is to use it for a wide range of inverse problems in the context of MCG, where the MCG data is measured in controlled conditions such as inside a Magnetically shielded roomas well as in unshielded environments with noise levels ranging from low to very high (differing SNRs). Hence, the method has been extensively tested in the following way before applying it to the actual MCG data recorded from real subjects. This has helped to validate the method initially to assess its suitability to correctly ascertain source parameters like source position, strength and depth.

(i) Generating computer simulated magnetic field data corresponding to a single current dipole based on equation (5.1), and using the simulated data as input to the proposed NM simplex algorithm to infer the source strength and location.

(ii) Measuring the magnetic field generated by passing current through a small multi-turn coil (mimicking a point dipole) at different locations on the sensor plane using SQUID sensors, and using this data as input to the proposed NM simplex algorithm to infer source strength and location.

5.2.3.2 Experimental design

(i) Computer simulation

For the simulation study, ECD model has been used to represent the current source. Typical set of source parameters, which are comparable in magnitude to those usually found by research workers in the context of actual MCG measurements [10], have been used as input to the forward model to calculate the magnetic field values at a discrete set of points simulating the sensor locations in actual MCG measurements. In order to see the effect of noise on source localization accuracy, an additive Gaussian noise was progressively added to the calculated signals, so that the resultant SNR could vary in a range from 55 dB to 10 dB in steps of 5 dB. This could mimic

a set of different noise conditions starting from the noise inside a typical MSR to the noise at a representative unshielded site.

(ii) Hardware setup

The hardware part consisted of the four channel low T_c DC SQUID based MCG system housing four DC SQUID sensors each connected to a superconducting pick-up coil in the form of a first order axial gradiometer configuration. The sensitivity of the four gradiometers was about 15 $fT_{rms}/\sqrt{Hz}$ when measured inside the MSR, and nearly 3 $pT_{rms}/\sqrt{Hz}$ at the chosen unshielded site (as mentioned in chapter 4) [11].

As a part of validating the NM algorithm, a small 10 turn copper coil having a diameter of 5 mm was placed under the MCG cryostat at certain known positions from the sensor plane to act as a source of magnetic field of known value when a current is passed through the coil. A synthetic cardiac signal of known amplitude and period was generated using a waveform generator and was applied through a series resistor to pass a proportionate current through the coil. The magnetic field generated due to the coil current at each sensor location was measured as a voltage output from the corresponding SQUID sensor. A sequential scanning was performed by moving the coil to different locations relative to the sensor plane and cryostat axis. Here, the algorithm was used to infer the parameters such as source position and source strength by using experimentally measured data-sets corresponding to different positions of the coil within an area of 21cm×21cm in the horizontal plane while the source depth was varied between 5 cm to 15 cm below the bottom of the cryostat.

MCG measurements were performed inside the MSR and at the unshielded site for 8 healthy normal subjects. MCG measurements were also performed inside the MSR on one subject with right bundle branch block (RBBB) and one subject with coronary artery disease (CAD). For each

subject, a total of nine scanning positions relative to the sensor array were covered sequentially to obtain a large number of cardiac magnetic waveforms at each of the thirty-six equispaced locations covering an area of 21cm by 21cm over the anterior thoracic surface. Single lead ECG for all the subjects was also simultaneously recorded in lead 1 configuration along with the MCG to serve as reference in order to extract the R-wave peak time instants for the purpose of epoching and averaging the noisy MCG data measured at the unshielded site in order to suppress uncorrelated noise and thereby improve the SNR.

5.2.4 MCG signal processing

The raw MCG data of all the channels were subjected to baseline correction using the wavelet transform algorithm for removing the unwanted low frequency undulations due to respiration of subjects. Then the baseline corrected data of each channel were epoched and then aligned with respect to the R peak time instants identified from the simultaneously recorded single lead ECG. Subsequently, a large number of these epoched cardiac cycles were averaged to obtain a single representative cardiac waveform corresponding to each measurement location. The averaged cardiac waveforms corresponding to each measurement location were then subjected to ensemble empirical mode decomposition (EEMD) technique to eliminate noise and further improve the SNR. A spatial map of cardiac waveforms was created by associating the averaged and denoised cardiac waveform with the corresponding measurement location. Using this data on magnetic field measured at discrete positions on the thoracic surface, interpolation techniques were used to obtain the magnetic field values at a very dense grid of points so that magnetic field values are available almost as a continuous function of position on the thoracic surface. At any instant of time on the cardiac cycle, the locations corresponding to equal magnitudes of magnetic fields (found by interpolation, if necessary) are joined to generate iso-field contour maps (also known as Magnetic field maps). By computing the spatial derivative of these MFM maps, PCD maps

were generated. It is known that when the source is assumed to be a dipole, maximum amplitude of the pseudo-current density occurs just above the source position, and the direction of the strongest pseudo-current corresponds to the direction of the source dipole moment. These values of source position inferred from the PCD maps were taken as the initial guess values for the position and orientation of the actual source for starting the NM method. Initial guess value of the *z* coordinate was based on the well-known relationship between the dipole depth and spatial separation between the positive and negative extrema in the MFM [12]. The initial guess value of the dipole moment was based on prior numerical simulation results, and was generally in the range of nA-m.

5.2.5 Evaluation criteria

Performance of the NM method has been evaluated in terms of three quantitative parameters which describe how well the magnetic field at all the sensor locations, calculated from the inferred source parameters, matches with the corresponding values of measured magnetic field [13]. They are computed as:

(a) R-Square (RSQ)- It is defined as:

$$\mathrm{RSQ}(\%) = \left(\sqrt{1 - \frac{\sum_{i=1}^{N}(B_{zi} - B_{si})^2}{\sum_{i=1}^{N}(B_{zi} - \overline{B_z})^2}}\right) \times 100 \tag{5.3}$$

(b) Root mean square error (RMSE) - It is defined as:

$$\mathrm{RMSE} = \sqrt{\frac{1}{N}\sum_{i=1}^{N}(B_{zi} - B_{si})^2} \tag{5.4}$$

(c) Goodness of fit (GOF) – It is defined as:

$$\mathrm{GOF} = \sqrt{1 - \frac{\sum_{i=1}^{N}(B_{zi} - B_{si})^2}{\sum_{i=1}^{N} {B_{zi}}^2}} \tag{5.5}$$

In the above equations, B_{zi}, and B_{si} denote the measured and calculated magnetic field gradient along the *z* direction for *i* th sensor respectively. $\overline{Bz}$ is the mean of the measured magnetic field gradients. The total number of points over which the measurement was performed (N) is 36.

5.3 Results

This section consists of two parts. At first, the results obtained from validation of the proposed method using data derived from computer simulation of an ECD source and those obtained by analyzing measured magnetic field produced by a small multi-turn coil excited with a synthetic cardiac waveform are presented. Subsequently, we present the results obtained by application of the method to actual experimental MCG data measured in both shielded and unshielded environments.

5.3.1 Results from simulation study

5.3.1.1 Localization of a dipolar source using computer simulated data admixed with noise

Table 5.1 presents the source parameters identified using the NM method to solve the inverse problem for the input data-set of calculated magnetic field distribution corresponding to an ECD assumed to be positioned at (-0.021m, 0.005m, -0.11m) with dipole moment of the current dipole set as (-560 nA-m, 260 nA-m). To simulate the presence of noise in the experimentally measured data, controlled levels of white noise were admixed with the calculated data to realize new data sets with different SNR values ranging from 10–55 dB in steps of 5dB. RSQ and RMSE values calculated for each case are also shown in table 5.1. It is observed that, when the SNR is

Table 5.1: RSQ AND RMSE for the simulated equivalent current dipole

SNR (dB)	$Q_x \times 10^{-7}$ *(Am)*	$Q_y \times 10^{-7}$ *(Am)*	*x (m)*	*y (m)*	*z (m)*	*RSQ (%)*	*RMSE (pT)*
55	-5.6	2.6	-0.021	0.005	-0.1100	100	0
50	-5.6	2.59	-0.021	0.005	-0.1101	99.998	5.7×10^{-3}
45	-5.6	2.59	-0.0211	0.0050	-0.1101	99.997	7.4×10^{-3}
40	-5.58	2.59	-0.0208	0.0048	-0.1099	99.988	1.5×10^{-2}
35	-5.61	2.61	-0.0213	0.0052	-0.1099	99.976	2.2×10^{-2}
30	-5.75	2.62	-0.0208	0.0051	-0.1115	99.860	5.3×10^{-2}
25	-5.72	2.71	-0.0195	0.0042	-0.1114	99.673	8.2×10^{-2}
20	-5.91	2.82	-0.0223	0.0044	-0.1136	99.232	1.2×10^{-1}
15	3.33	-2.23	-0.0076	-0.0187	-0.1030	95.474	3.0×10^{-1}
10	3.75	-2.22	-0.0210	-0.0104	-0.1096	85.298	5.4×10^{-1}

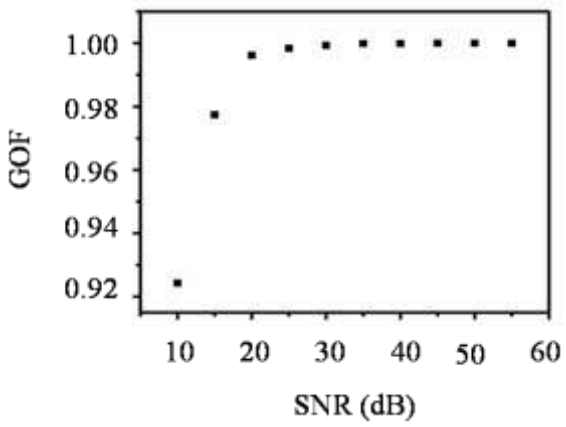

Figure 5.1 Variation of goodness of fit (GOF) for the fitted magnetic field data with respect to Signal-to-Noise ratio (SNR) of the input data used for estimation of source parameters. The GOF approaches unity as the SNR increases beyond 20dB.

sufficiently high, the method yields accurate and consistent values of source parameters such as dipole strength and dipole position, which is also evident from the computed RSQ and RMSE values. Figure 5.1 shows the plot of GOF for data sets corresponding to different values of SNR. It is evident that the magnetic field distribution taken as input to the N magnetic field distribution calculated using the inferred values of source parameters are in fair agreement with each other as long as the SNR is higher than 20 dB. M method to identify the source parameters and the This

minimum value of SNR required for a reliable estimation of source parameters is comparable to the values of SNR generally encountered when MCG measurements are performed in unshielded environment, [11]. The similarity of the MFM map of the ECD having a SNR of 20dB (which was taken as input to the NM algorithm for estimating the source parameters), and the MFM map calculated from the source parameters estimated using the NM method lends further credence to this conclusion, as shown in figure 5.2.

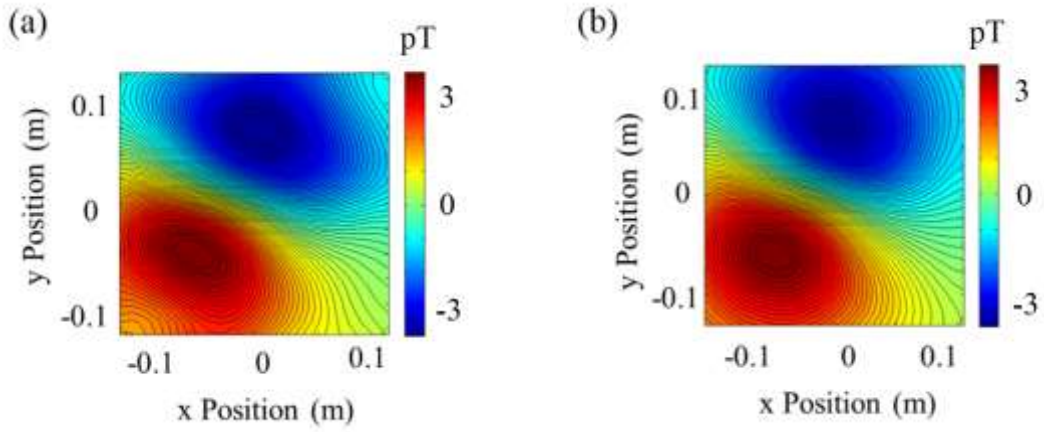

Figure 5.2 (a) Simulated MFM for an equivalent current dipole (ECD) for an SNR of 20 dB (b) MFM reconstructed using the source parameters estimated by Nelder-Mead algorithm. Qualitative and quantitative similarity between the two MFMs indicates the reliability of the NM method in estimating the source parameters.

5.3.1.2 Localization of test coil

The source position parameters obtained by application of NM method to the input data-set corresponding to the measured magnetic field distribution generated by a small multi-turn coil excited by a synthesized cardiac waveform were compared with the values of the actual position of the multi-turn coil known apriori. Figure 5.3 shows the results obtained when the test coil was placed at the center of the grid at a depth of 9 cm from the sensor plane. Figure 5.3 (a) and (b) respectively show the magnetic field distribution at 36 spatial locations at the vertices of a square grid and the corresponding MFM generated at the instant of R peak of the synthetic cardiac

waveform. Figure 5.3 (c) is the PCD map constructed using the corresponding MFM. The green dot depicts the position of the largest current arrow, which is chosen as the initial guess point for solving the inverse problem using the NM method. Figure 5.3 (d) shows the reconstructed MFM

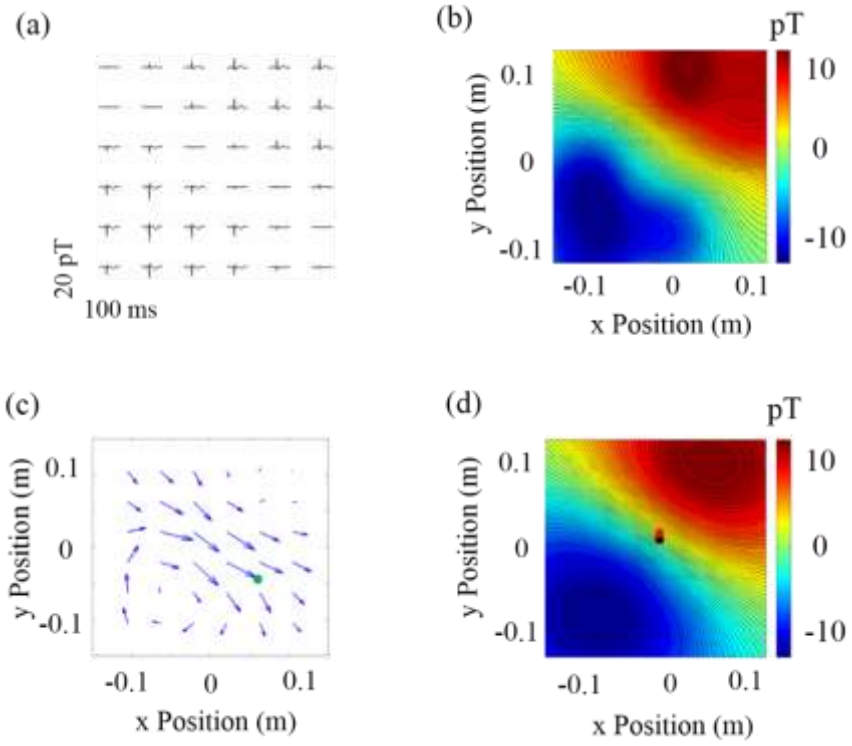

Figure 5.3 (a) Spatial distribution of magnetic field signals generated by feeding a synthetic cardiac waveform to a small test coil and measured over 36 locations by sequential repositioning of the test coil relative to the sensor array (b) MFM generated at the R peak time instant of the synthetic cardiac cycle (c) PCD map for the corresponding MFM showing the initial guess point for NM algorithm corresponding to the point of maximum field gradient marked as a green dot (d) reconstructed MFM showing the source position identified using NM algorithm as a red dot and the actual position of the coil known apriori as a black dot.

with the red dot showing the position of the source obtained using the proposed approach, and is seen to be almost identical to the actual position of the source known apriori (shown as a black dot in the same figure for comparison). The position of the source was found to be (-0.003 m, 0.002 m, 0.092 m) which is in close agreement with the known actual source position of (0 m, 0 m, 0.090m).

The maximum positional error in x' and y' was found to be about ± 6 mm when the coil was kept at the extreme corner of the measurement grid for measurements performed inside the MSR, while it was ± 1 cm for unshielded measurement. Similarly, the maximum localization error associated with the z' component was found to be ± 7 mm when the source was kept at a maximum depth of 15 cm for the measurement performed inside MSR, and about ±1.5cm for the unshielded measurement.

5.3.2 Results on source localization by analyzing actual MCG data

5.3.2.1 Healthy subjects

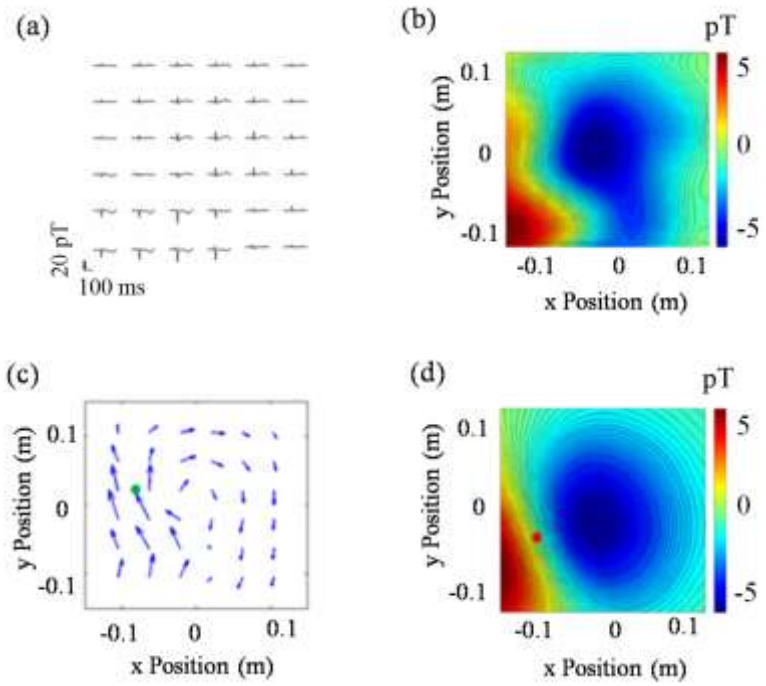

Figure 5.4 (a) Spatial distribution of averaged and denoised cardiac waveforms over 36 locations for a normal subject (b) MFM constructed at the S peak time instant of the cardiac cycle (c) PCD map for the corresponding MFM showing the initial estimate of source position (marked as a green dot) chosen over the maximum field gradient vector (d) MFM reconstructed using the source parameters obtained using the Nelder-Mead algorithm with the red dot showing the position of the identified source.

Figure 5.4 (a) shows the signal averaged MCG waveforms over 36 locations on the anterior thoracic surface of a normal subject. Figure 5.4 (b) shows the MFM constructed at the S peak time instant of the cardiac cycle. The corresponding PCD map is shown in figure 5.4 (c). The initial estimates for *x* and *y* coordinates of the assumed ECD model are chosen to be located over the maximum current arrow (marked as a green dot) of the PCD map and are fed to the Nelder-Mead method along with the initial estimates for other source parameters. The reconstructed MFM plotted using the inverse solution found using the Nelder-Mead algorithm is shown in figure 5.4 (d) together with the inferred source position marked as a red dot.

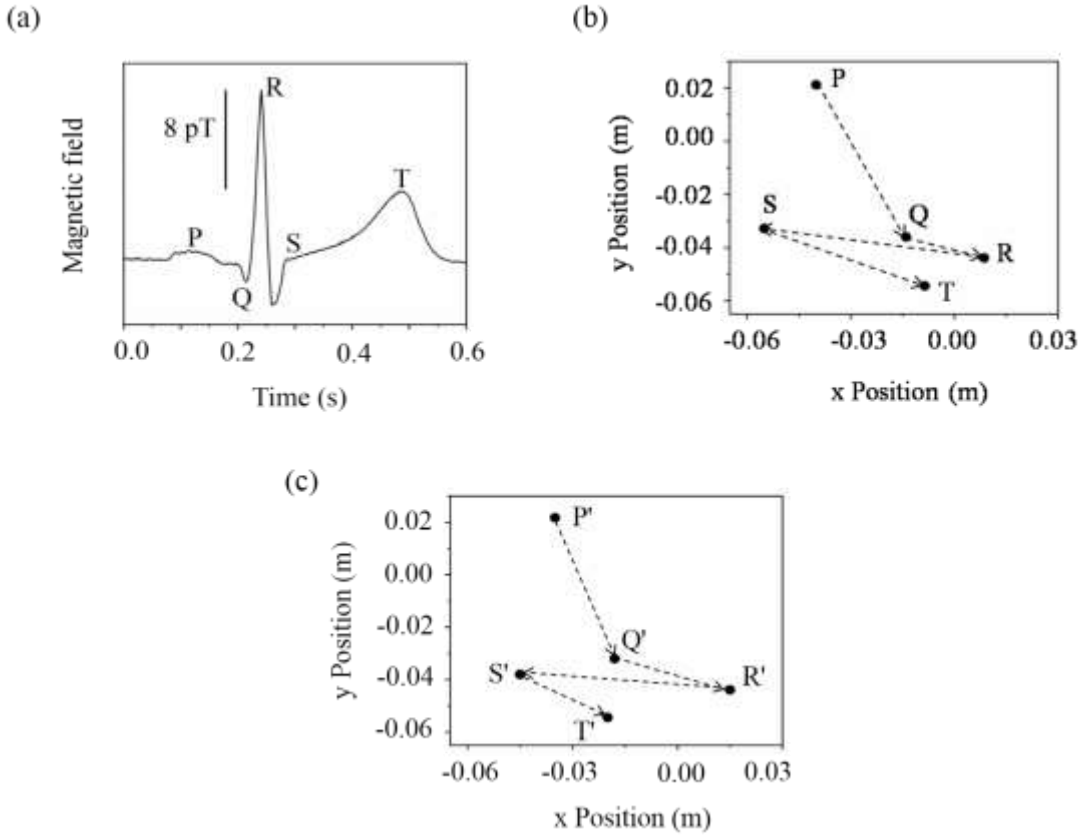

Figure 5.5 (a) A representative cardiac waveform of a normal subject depicting the various reference points (P, Q, R, S, T) on the cardiac cycle; the position of the cardiac source at each of these points has been estimated by solving the inverse problem using Nelder-Mead algorithm. (b) and (c) show the positions of the cardiac sources at P, Q, R, S and T time instants of the cardiac cycle identified for the normal subject using the Nelder-Mead method for MCG measured in shielded and unshielded environment respectively. The black dotted arrows indicate the sequence of activation of the cardiac source.

Similarly, the positions of the cardiac source at various other time instants (P, Q, R and T) of the cardiac cycle marked in figure 5.5 (a) were identified for a normal subject, and are shown in figure 5.5 (b). The sequence of activation of the cardiac source is indicated by the dotted black arrows.

Assuming the position of the heart to be at the center of the measurement grid, it is possible to appreciate the identified localized dipolar sources to be associated with their corresponding anatomical sites of activation. The *x* and *y* position coordinates of the localized dipolar source corresponding to the P peak falls over the left anterior portion of the measurement grid. This position may be visualized as the right atrium of the subject's heart. Similarly, the position of the localized dipolar source position corresponding to the Q peak is known to be associated with the activation of the inter-ventricular septum. At the R peak time instant, the position of the dipolar source appears to be over the left ventricle which moves to the right ventricle during the S peak time instant. At the T peak time instant, the source appears to be positioned at the left and inferior portion of the heart. These positions of the identified dipolar source appear to be in accord with the known anatomical and physiological features of a healthy heart and the known course of cardiac electrical activation for a healthy subject.

Figure 5.5 (c) shows the position of the source localized at P, Q, R, S and T peak time instants for MCG measurements performed for the normal subject at the unshielded site. The arrows in the line joining the sources (P′-T′) as marked in the figure indicate the sequence of activation of the cardiac source as one moves from P peak to T peak instants of time. It may be noted that as the activation front propagates during the cardiac cycle, positions of the dipolar source identified using both the shielded and unshielded MCG data-sets are reasonably close to each other.

5.3.2.2 Subject with RBBB

In figure 5.6 (a), the averaged and denoised cardiac waveforms representative of each of the thirty-six locations over the thorax of a subject with RBBB are superposed and plotted together as a butterfly plot. We analyzed the cardiac source around the S peak time instant to highlight the characteristic anomaly associated with the right bundle branch block. By dividing the R-S interval (from the end of the R peak to the end of S peak) into 8 equal intervals of 12 ms duration, the cardiac sources were estimated and analyzed as shown in figure 5.6 (b).

Figure 5.7 (a) shows the spatial distribution of denoised MCG waveforms representative of

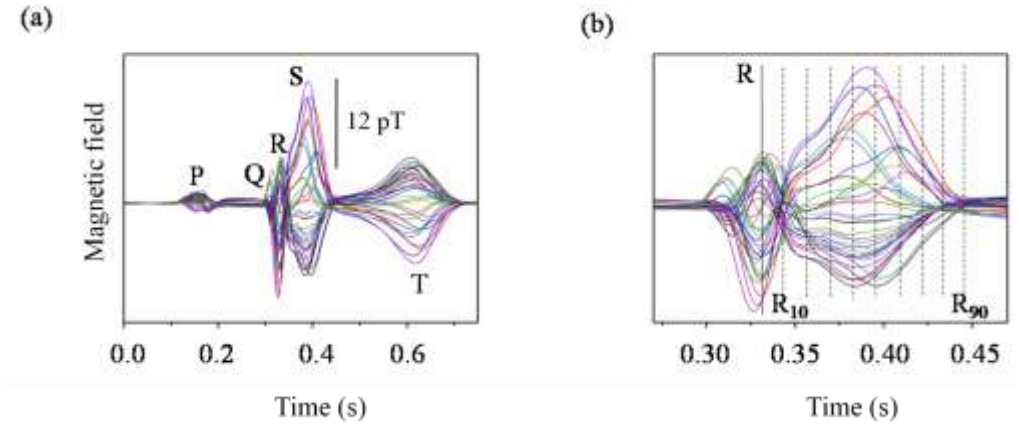

Figure 5.6 (a) Butterfly plot for a subject with RBBB (b) The time interval between R_{10} to R_{90} has been divided equally into 8 segments (each of around 12 ms duration) and the Nelder-Mead method has been used to localize the source at the end of each segment.

each of the 36 locations for the subject with RBBB. The MFM and PCD maps corresponding to S peak time instant are shown in figure 5.7 (b) and (c) respectively. By choosing the initial guess point over the maximum current arrow (shown as green dot in figure 5.7 (c)), NM method was used to solve the inverse problem and estimate the source parameters at the S peak time instant. Figure 5.7 (d) shows the reconstructed MFM for the S peak time instant along with the position parameters of the source obtained by the proposed method as a red dot.

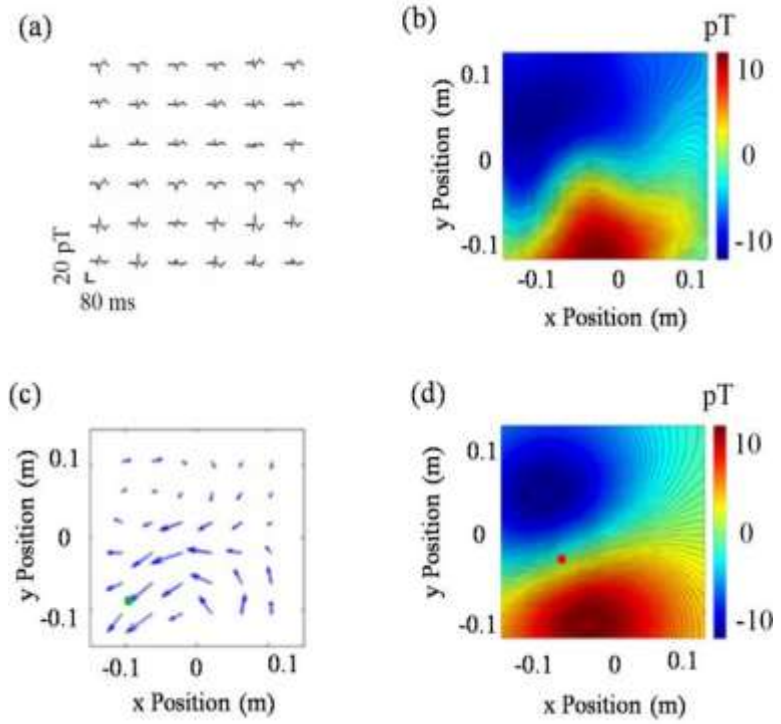

Figure 5.7 (a) Spatial distribution of averaged and denoised MCG waveforms representative of each of the thirty-six locations for a subject with RBBB (b) measured MFM at the S peak time instant of the cardiac cycle (c) PCD map for the corresponding MFM showing the initial guess point (green dot) taken as input to the Nelder-Mead method (d) reconstructed MFM showing the position of the source (red dot) inferred using the proposed method.

In order to highlight the degree of conduction anomaly in the subject with RBBB, the source was estimated from the end of R peak to the end of S peak of a normal subject by dividing this R-S interval into eight equal time segments in a manner similar to the RBBB case. Here the time duration of each segment was, however, only around 4 ms as the QRS for the normal subject spans a comparatively shorter duration. At each instant of time from R_{10} to R_{90}, cardiac dipolar sources were identified using the NM method to solve the inverse problem and estimate the source parameters. These positions of the inferred sources are shown in figure 5.8 for both normal subject and for the subject with RBBB. A stark contrast could be observed in the sequence of ventricular activation between the normal subject and the subject with RBBB. The cardiac activation seems to take a considerably longer time to reach the right ventricle from the left one consistent with underlying pathophysiology associated with RBBB [14]. The delay in

conduction of the activation front for the RBBB case compared to that for a normal heart was quantified by finding the corresponding average conduction velocities during the time interval between the time instants R_{10} to R_{90}. The average conduction velocity was found to be 1.2 m/s for the RBBB subject which was about 3 times lower than that found for a normal subject. For reference, the positions of the source at R peak time instant have also been marked in the figure for both the cases.

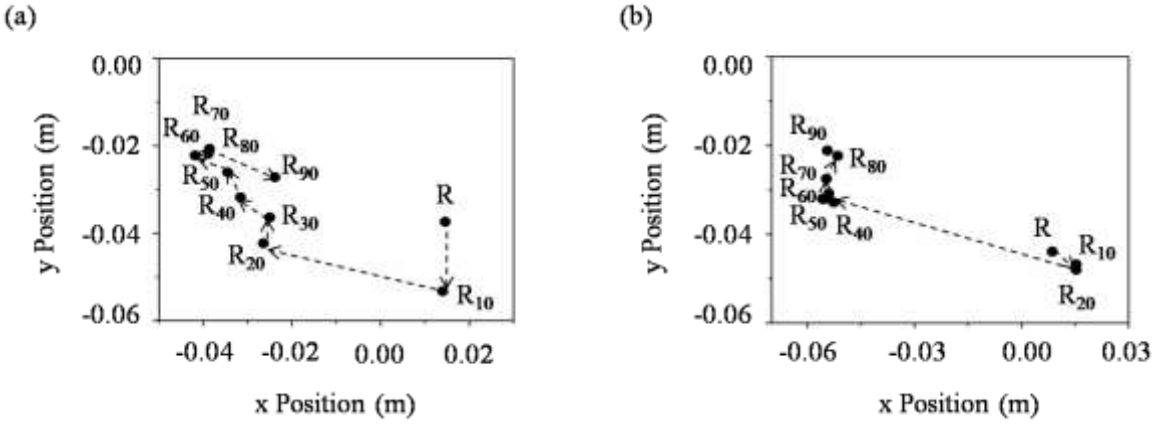

Figure 5.8 Position of the source localized for each of the 8 equal time segments forming the interval R_{10} to R_{90} starting from the end of R peak to the end of S peak for (a) subject with RBBB (b) normal subject. The total time span for (R_{10}-R_{90}) in the case of normal subject is around 31ms, while it is 100 ms for the subject with RBBB.

5.3.2.3 Subject with CAD

Figure 5.9 shows the averaged and denoised cardiac waveforms representative of each of the 36 locations on the anterior thoracic surface plotted together as a butterfly plot for a subject with coronary artery disease (CAD). Here, the cardiac source responsible for the measured activity has been analyzed by dividing the time duration from the S peak to the T peak into four equal segments and localizing the source at the end of each segment. Figure 5.10 (a) shows the signal averaged MCG traces at 36 different locations over the anterior thoracic surface. The MFM plotted at the T peak time instant of the cardiac cycle is shown in figure 5.10 (b),

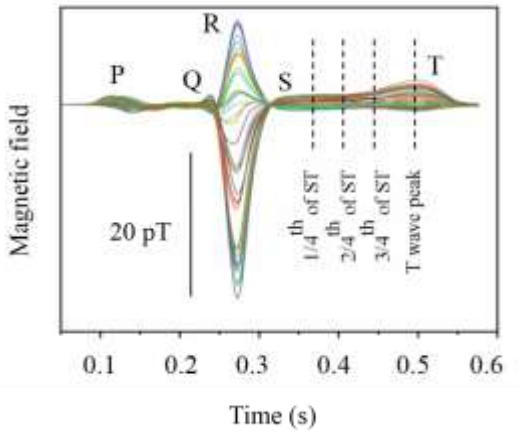

Figure 5.9 Butterfly plot for a subject with coronary artery disease (CAD). The position of the current source has been localized for four equal time segments starting from the S peak up to the T peak.

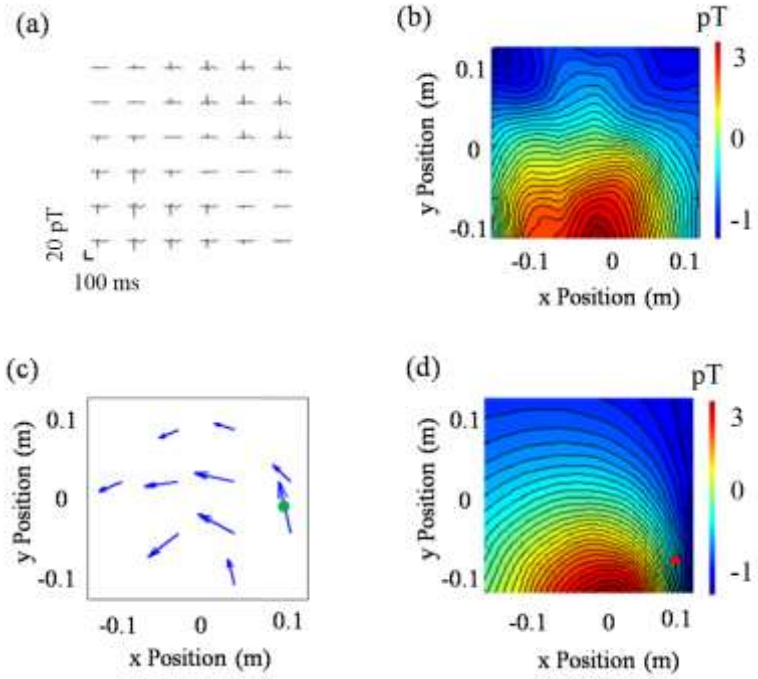

Figure 5.10 (a) Spatial distribution of denoised cardiac waveforms over 36 locations for a subject with CAD (b) measured MFM at the T peak time instant of the cardiac cycle (c) PCD map for the corresponding MFM showing the initial guess point (green dot) (d) reconstructed MFM showing the position of the dipolar source identified by the proposed method (red dot).

while the corresponding PCD map is plotted in figure 5.10 (c). The position coordinates corresponding to the maximum gradient vector of the PCD map, indicated as a green dot in

figure 5.10 (c), served as the initial estimates of the position parameters of the source while solving the inverse problem using the NM method. Figure 5.10 (d) shows the reconstructed MFM using the source parameters identified by the NM method for comparison. Similar analysis has also been performed for normal subjects to understand the nature of abnormal deviations, if any, for the subject with CAD.

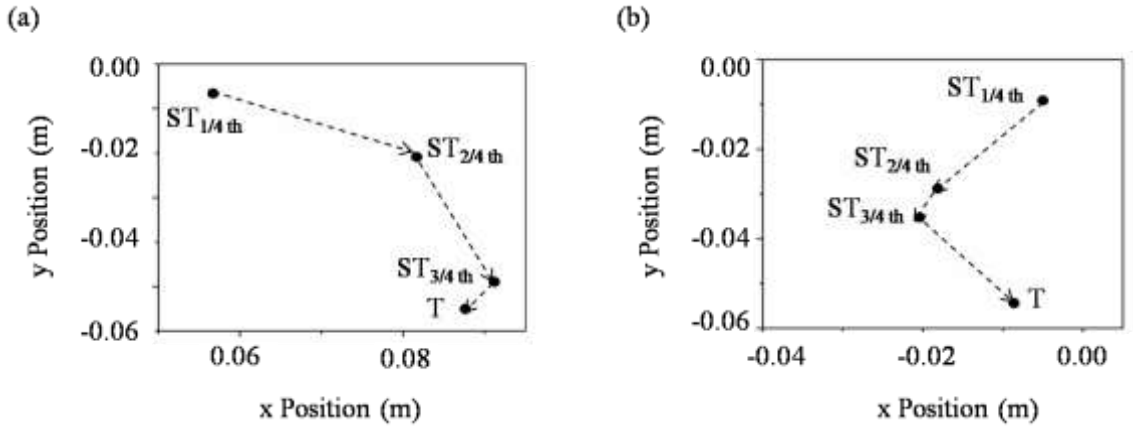

Figure 5.11 Position of the current source localized at $ST_{1/4th}$, $ST_{2/4th}$, $ST_{3/4th}$ and T peak for (a) subject with CAD (b) normal subject. 'ST' refers to the time segment between the S peak to the T peak.

The positions of the dipolar source identified at specified time instants in the S-T interval for the subject with CAD and for the normal subjects have been shown in figure 5.11 (a) and (b) respectively. It is evident from figure 5.11 that the cardiac source, identified using the ECD model, appears to show an anomalous behaviour for the subject with CAD when compared with the normal subject.

The computation time taken by any algorithm to converge to a solution is crucial for a comparative assessment of different algorithms used for estimating the cardiac sources. Table 5.2 lists the computation time required to reach convergence for the simulated data-sets (magnetic fields calculated using computer simulation of ECD and magnetic fields measured for a current carrying test coil as well as for the real MCG data, when the corresponding inverse

problems were solved using NM method with one set of initial parameter estimates based on the position parameters inferred from the PCD map and another set of initial parameters based on generation of pseudorandom numbers. In order to assess the suitability of the NM method for optimization of the source parameters in case of data-sets measured using both shielded and unshielded MCG set ups, these simulated and actually measured MCG data was recorded under two different SNR conditions (higher SNR of 55 dB, and a lower SNR of 20 dB) by admixing controlled amount of noise for the simulated data and by making MCG measurements inside or outside the shielded room for the measured data. The computation time required to reach convergence in all these cases are included in table 5.2. All the optimization programs using the NM method were executed in a PC with configuration: Intel (R) Core (TM) 2 Duo CPU @ 3.00 GHz and 2 GB RAM.

Table 5.2: Comparison of computation time for the Nelder-Mead technique applied using different methods for the estimation of initial values of parameters

	Computer simulation data-set (s)		**Test coil simulation data-set (s)**		**Real MCG data-set (s)**	
	Higher SNR	*Lower SNR*	*Higher SNR*	*Lower SNR*	*Higher SNR*	*Lower SNR*
NM_PCD (proposed method)	0.042±0.028	0.042±0.028	0.043±0.03	0.043±0.03	0.043±0.03	0.043±0.03
NM_ pseudorandom numbers	28.5±3.5	90.5±10.8	30.8±3.9	112.5±14.6	34.6±3.8	118.5±18.8

5.4 Discussion

The variation of SNR from 55 dB to 10 dB in the computer simulation data is intended to mimic the typical values of SNR obtained in a MCG measurement carried out inside a well shielded

MSR, partially shielded MSR and a practical unshielded hospital setup. It may be inferred from these simulations that, as the noise level increases (accompanied by a fall in SNR), the ability of the NM method in accurate localization of the source parameters suffers. However, our evaluation of the source parameters as shown in table 5.1 and figure 5.1 for the computer simulated data-sets indicates that the solutions obtained by the proposed method do not deviate significantly from the actual values of source parameters at least up to a SNR of 20 dB which is fairly realistic for MCG measurements performed in moderately shielded environments. Figure 5.2 illustrates this fact by highlighting the similarity between the MFM used as input to the NM algorithm, and the MFM constructed from the source parameters estimated by using the NM algorithm.

Unlike any simulation study, where it is perhaps easy to guess an initial estimate of the source parameters to seek a solution using the NM algorithm, it is practically quite difficult to provide approximate initial estimates of source parameters that can result in reasonably quick convergence to a globally optimized solution in case of typical MCG measurements. Further, implementation of the algorithm with different sets of pseudo-random numbers as initial estimates of source parameters becomes computationally intensive if the cost function has a large number of local minima; the situation gets worse if the input data has a low SNR (as seen from table 5.2). In this context, the use of a PCD map helps in providing a reasonable initial estimate of the source parameters, which ultimately facilitates a faster convergence to the final solution (within less than 50 milliseconds) and thus, a much quicker source localization.

As shown in figure 5.5, positions of the cardiac ECD source at various time instants of the cardiac cycle obtained by solving the inverse problem are seen to be in general accord with the known physiology of a normal electrical conduction of heart [15]. Hence the solutions of the MCG inverse problem, even within the limits of validity of the ECD model, can be used to directly

interpret cardiac electrophysiology. Any significant deviations in the source positions from the standard ones for the healthy heart could reveal some important diagnostic information. These diagnostic aspects have been illustrated in two specific cases of cardiac disorders, viz., right bundle branch block (RBBB) and ischemic heart disease. As shown in figure 5.4 (b) and 5.7 (b), an abnormal orientation of the current dipole at the S peak time instant of the cardiac cycle is clearly seen for the subject with RBBB. The direction of the current vector at this time instant clearly indicates an electrical activation propagating from left to right in the ventricles. Further information about the abnormal equivalent current dipole vector was obtained from the successive source positions identified during the time interval between the ends of R peak and S peak as shown in figure 5.8. Here, for the subject with RBBB, the cardiac source seems to move more slowly towards the right compared to the normal subject which may be possibly attributed to a decrease in the conduction velocity as expected in a subject with bundle branch blocks [14]. In case of the subject with CAD, repolarization abnormalities which are evident from the rotations of the current angles during the ST segment have been understood using the source positions localized using the NM method. The deviations in the positions of the localized sources compared to a normal subject could possibly be related to the flow of injury currents in such ischemic regions [16]. It may be noted that, depending upon the location of ischemic region in the heart as well as the percentage of myocardial tissue which is affected, the overall appearance of the observed MFM pattern and, consequently, the position of the cardiac source during the ventricular repolarization phase may be expected to change considerably compared to the normal subject [16].

The dipolar source parameters obtained by solving the inverse problem for the unshielded MCG data sets compared well with those derived from data-sets corresponding to MCG measurements carried out inside a magnetically shielded room (as seen in figure 5.5 (b) and (c)). The small change in the source parameters obtained in these two cases may be attributed to slight

differences in positioning of the subject relative to the sensor array while carrying out MCG measurements successively in shielded and unshielded environment.

There are possibilities to superpose the sources identified using the proposed method over the structural images of the human heart to provide a visual representation of this information to a practicing cardiologist, thereby further enhancing the diagnostic potential of the MCG technique. By facilitating such a visualization of cardiac sources, the present work could be extended to investigate other pathologies such as retrograde conduction, accessory pathways, arrhythmogenic foci etc., where such source localization would be quite promising.

It may be noted that, in the proposed method for identification of source parameters by using an ECD model to solve the inverse problem for measured MCG data-sets, the initial estimates of the position coordinates are guessed from the PCD maps and the magnetic moments are assumed to be of the order of nA-m based on earlier published reports and from the simulation studies; these choices are known to be reasonable for adult human hearts [12, 17]. However, for fixing the initial estimates of source parameters for other animal species, additional information may be required taking into consideration specific anatomical and electrophysiological features. While performing the sequential scanning of thirty-six positions using a four-channel cryostat by changing the position of the subject relative to the cryostat, small positional errors are possible, which can potentially lead to some errors in the source localization results. This could be minimized, in principle, by using a cryostat with larger number of channels, which enables MCG measurements to be carried out at all the thirty-six positions simultaneously. In the present study, the source localization was limited to the identification of sources producing a predominantly dipolar Magnetic field map; however, it is possible to extend the approach to investigate the sources responsible for non-dipolar MFMs by considering either multi-dipole models or even

more complicated models involving distribution of source currents over a large volume inside a realistically shaped volume conductor [18].

5.5 Conclusion

This study was aimed at developing a suitable framework to solve the magnetocardiographic inverse problem by assuming the validity of the equivalent current dipole model. The initial estimates of the source parameters were derived from the pseudo-current density maps, and were iteratively refined using the Nelder-Mead optimization method. The method has been thoroughly validated over simulated cardiac sources by considering noise-admixed data-sets with different values of SNR. The accuracy of the source localization was observed to be excellent in the absence of noise, but decreased progressively with increase in the level of admixed noise. However, even with low values of SNR (~20 dB), the relative degradation in the accuracy of inferred source parameters was found to be rather small, making the proposed method suitable for handling unshielded MCG data or for localizing deeper cardiac sources. The efficacy of the algorithm has been demonstrated by localizing the source positions at a number of points on the cardiac waveform for both normal subjects and subjects with cardiac abnormalities. The results of the source localization algorithm applied to measured MCG data were found to be in accord with our general expectations on the basis of cardiac electrophysiology. It is clear that the choice of initial estimates of source parameters based on pseudo-current density maps enabled localization of the cardiac source with superior accuracy and higher computational efficiency. There are possibilities to develop this method further as a promising tool for diagnosing various cardiac disorders in practical clinical setups.

References

1. J Clarke and A Braginski, The SQUID handbook, vol I, WILEY-VCH, ISBN 9783527603640, 2004.

2. J Malmivou and R Plonsey. Bioelectromagnetism. Oxford University press, New York, ISBN: 9780195058239, 1995.

3. N Mariyappa, C Parasakthi, S Sengottuvel, K Gireesan, R Patel, M Janawadkar, C Sundar and T Radhakrishnan. Dipole location using SQUID based measurements: Application to magnetocardiography. *Physica C*. **477** (2012) 15-19.

4. R Avci, J Wilson, D Escalona-Vargas and H Eswaran. Tracking fetal movement through source localization from multisensory magnetocardiographic recording. *IEEE J Biomed Health Inform.* **22** (2018) 758–765.

5. D Escalona-Vargas, P Murphy, L Lowry and H Eswaran. Genetic algorithms for dipole location in fetal magnetocardiography. *IEEE EMBS*. 2016. doi: 10.1109/EMBC.2016.7590847.

6. D Potyagaylo, E Cortes, W Schulze and O Dossel. Binary optimization for source localization in the inverse problem of ECG. *MBEC*. **52** (2014) 717-728.

7. T El-Mihoub, A Hopgood, L Nolle and B Alan. Hybrid Genetic Algorithms: A review. *Engg Letts*. **13** (2006).

8. H Wright. Nelder-Mead and other simplex method. *Documenta Math*. (2012) 271–276.

9. J Sarvas. Basic mathematical and electromagnetic concepts of the biomagnetic inverse problem. *Phys Med Biol*. **32** (1987) 11-22.

10. R Jurkko, V Mantynen, M Tapanainen, J Montonen, H Vaananen, H Parikka and L Toivonen. Non-invasive detection of conduction pathways to left atrium using magnetocardiography: validation by intra-cardiac electroanatomic mapping. *Europace*. **11 (**2008) 169-177.

11. P Swain, S Sengottuvel, R Patel, A Mani and K Gireesan. A feasibility study to measure magnetocardiography (MCG) in unshielded environment using First Order Gradiometer. *Biomed Signal Proces*. **55** (2020) 1-9.

12. N Mariyappa. Development of SQUID based Magnetocardiography system and cardiac signal-source analysis using Ensemble Empirical Mode Decomposition [dissertation], India: Homi Bhaba National Institute; 2013.

13. S Jiang, M Chi, L Zhang, M Luo and L Wang. Dipole source localization in magnetocardiography. Proceedings of NFSI &ICFBI; 2007 Oct 12-14; Hangzhou, China.

14. B Leithauser, J Park, P Mill, Y Lam and F Jung. Magnetocardiography in patients with acute chest pain and bundle branch block, *Int J Cardiol.* **168** DOI: 10.1016/j.ijcard.2013.01.254.

15. D Park and G Fishman. The cardiac conduction system. *Circulation*. **123** (2011) 904-915.

16. S Watanable and S Yamada. Magnetocardiography in early detection of electromagnetic abnormality in ischemic heart disease. *J Arrhythmia*. **24** (2008) 4-17.

17. R Fenici, D Brisinda and A Meloni. Clinical application of magnetocardiography. *Expert Rev Mol Diagn*. **5** (2005) 291-313.

18. S Kawakami, H Takaki, S Hashimoto, Y Kimura, T Nakashima, T Aiba, K Kusano, S Kamakura, and M Sugimachi. Utility of high resolution magnetocardiography to predict later cardiac events in nonischemic cardiomyopathy patients with normal QRS duration. *Circ J*. **81** (2017) 44-51.

LIST OF SYMBOLS

cm	centimetre
mm	millimetre
mV	millivolt
Hz	Hertz
kHz	kilo Hertz
MHz	mega Hertz
dB	decibel
s	second
pT	pico Tesla
fT	femtoTesla
µT	micro Tesla
nT	nano Tesla
He	Helium
N_2	Nitrogen
Nb	Niobium
B	magnetic field
ϕ	magnetic flux
ϕ_0	Flux quantum
K	Kelvin
T_c	Transition temperature

I	current
I_b	Bias current
I_s	Screening current
Wb	Weber
L	Inductance
V	Voltage
R	Resistance
R_f	Feedback resistance
Ω	ohm
θ_c	maximum current angle
θ_m	field map angle
r	Pearson correlation coefficient

LIST OF ABBREVIATIONS

ADC	Analog-to-Digital Converter
AMR	Anisotropic Magnetoresistance
AV node	Atrio-Ventricular node
BSPM	Body Surface Potential Mapping
CAD	Coronary artery disease
DAQ	Data Acquisition
DC	Direct Current
ECD	Equivalent Current Dipole
ECG	Electrocardiography
EEMD	Ensemble Empirical Mode Decomposition
EMD	Empirical Mode Decomposition
FLL	Flux Locked Loop
FOG	First Order Gradiometer
FRP	Fiber Reinforced Plastic
GA	Genetic Algorithm
GMR	Giant Magnetoresistance
GOF	Goodness of Fit

HHT	Hilbert-Huang Transform
HTSC	High temperature superconductor
ICA	Independent Component Analysis
IGCAR	Indira Gandhi Centre for Atomic Research
IMF	Intrinsic Mode Functions
LM	Levenberg-Marquardt
LTSC	Low temperature superconductor
MCG	Magnetocardiography
MFM	Magnetic field map
MI	Myocardial infarction
MR	Magnetoresistance
MSR	Magnetically Shielded Room
NM	Nelder- Mead
OPM	Optically Pumped Magnetometer
PC	Personal Computer
PCA	Principal Component Analysis
PCD	Pseudo-Current Density
PSD	Power Spectral Density
RBBB	Right bundle branch block
RF	Radio Frequency

RFSR	Radio Frequency Shielded Room
RMSE	Root Mean Square Error
RSQ	R-Square
SA node	Sinoatrial node
SD	standard deviation
SNR	Signal-to-Noise Ratio
SOG	Second Order Gradiometer
SPECT	Single Photon Emission Computed Tomography
SQUID	Superconducting Quantum Interference Device
TMR	Tunnel Magnetoresistance
WPW syndrome	Wolf-Parkinson-White syndrome
YBCO	Yttrium Barium Copper Oxide

Thesis Highlight

Name of the Student: Pragyna Parimita Swain
Name of CI: Indira Gandhi Centre for Atomic Research **Enrolment No.:** PHYS 02 2015 04 021
Thesis Title: Measurement and analysis of magnetocardiograms for shielded and unshielded setups
Discipline: Physical Sciences **Sub-Area of Discipline:** Condensed matter physics
Date of viva voce: 23/06/2021

Magnetocardiography (MCG) is a non-invasive and non-contact technique to measure the magnetic fields associated with the electrical activity of heart and is expected to effectively complement the routinely used electrocardiography (ECG) by providing additional independent information for the assessment of cardiac health and possible disorders. In spite of the distinctive information provided by MCG, application of MCG as a routine technique for the assessment of cardiac health is presently not very popular in clinical environments owing to the lack of standardized measurement protocols, relatively high capital cost, usage of cryogenic sensor technology and inherent non-portability of the MCG system. The present thesis takes into account of these limitations of the MCG technique and strives to address some of them.

The thesis proposes the use of conventional technique based magnetic field map (MFM) and presents its use as a standard tool for the visualization of the measured MCG data at any given instant of time on the cardiac cycle. The importance of parameters derived from the MFM to reliably classify the cardiac anomalies over patients with coronary artery disease (CAD) and right bundle branch block (RBBB) are highlighted.

The present thesis describes a feasibility study to measure MCG at an unshielded site with acceptable signal-to-noise ratio. The work addressed various issues such as site-survey of magnetic noise to select a relatively magnetically quiet site, development of software based procedures for effective noise cancellation and finally the successful demonstration of extraction of MCG signal from the data recorded at the unshielded site. Figure 1 shows the comparison of the denoised MCG traces in unshielded environment against those measured inside MSR for a subject at a representative location on the chest.

Another major contribution relates to the localization of cardiac sources responsible for the measured magnetic field distribution using a simple source model. Taking the initial values of source parameters derived from the MFM and pseudo-current density maps to start the iterative optimization of source parameters, it has been shown that the optimization algorithm designed to minimize a suitably chosen cost function converges quickly to the final solution. The proposed algorithm has been used to evaluate the source parameters at various instants of time along the cardiac cycle for healthy subjects as well as subjects with different cardiac disorders and the source parameters have been found to be in general agreement with the underlying electrophysiology in each case. Figure 2 illustrates the localization of cardiac source at the 'S' peak time instant of the cardiac cycle for a healthy subject.

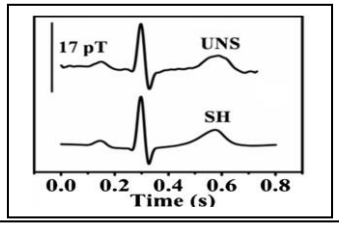

Fig. 1. Comparison of the unshielded (UNS) MCG trace denoised with Ensemble Empirical Mode Decomposition (EEMD) method with those measured inside a magnetically shielded room (SH) for a representative measurement location on the thorax.

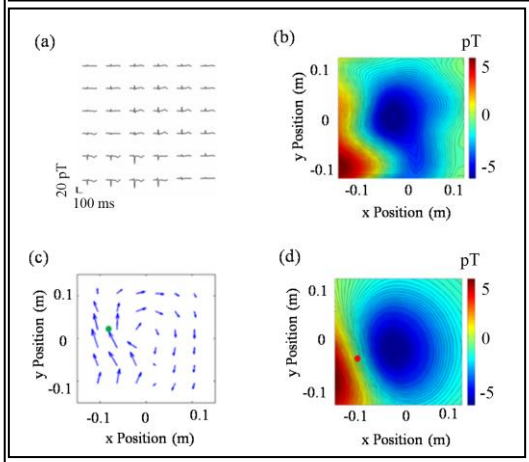

Fig. 2. (a) Spatial distribution of averaged cardiac traces over 36 locations of a normal subject (b) measured MFM at the S peak time instant of the cardiac cycle (c) PCD map for the corresponding MFM showing the initial estimate (marked as a green dot) chosen over the maximum field gradient vector (d) MFM reconstructed using the solution of pattern search algorithm with the red dot showing the position of the identified source.